

Photoacoustic Tomography: From Bench to Bedside

Thesis by

Li Lin

In Partial Fulfillment of the Requirements for

The Degree of

Doctor of Philosophy

The logo for Caltech, featuring the word "Caltech" in a bold, orange, sans-serif font.

CALIFORNIA INSTITUTE OF TECHNOLOGY

Pasadena, California

2020

(Defended December 4, 2019)

© 2019

Li Lin

ORCID: 0000-0002-0517-8436

All rights reserved

ACKNOWLEDGMENTS

I would like to express my sincere thanks to my advisor, Prof. Lihong V. Wang, for his support, guidance, and inspirations throughout my Ph.D. journey. I treasure the chance to perform first-rate research and solving cutting-edge scientific problems in his lab. I always encourage myself by Prof. Wang's words, attitudes, and the experiences. I believe the lessons I learned from him will benefit my future career and even my next generations.

Many lab members also offered me generous help. I appreciate Junjie Yao, Peng Hu, Junhui Shi, Jun Xia, Pengfei Zhang, Shuai Na, Rui Cao, David Garrett, Wenyu Bai, Tsz Wai Wong, Lidai Wang, Xiaohua Feng, Garcia-Urbe Alejandro, and Konstantin Maslov. Without their inspirations and supports, my work cannot be accomplished smoothly. I am thankful to the mechanical support from James Linders and the clinical support from Drs. Lily Lai and Catherine Appleton. I want to say thank you to my committee members, Drs. Mikhail Shapiro, Yu-Chong Tai, and Changhuei Yang, for their invaluable advice and help on my research.

Last but certainly not least, I owe my special thanks to my family for their boundless loves and unconditioned supports.

This work was sponsored by National Institutes of Health (NIH) grants DP1 EB016986, R01 CA186567, R01-CA159959, and EB016963.

DEDICATION

To my wife Xi Li, my daughter Shilan Lin, my parents, and my parents in law,
for their true love and support.

ABSTRACT

Photoacoustic imaging (PAI) is an emerging imaging modality that shows great potential for preclinical research and clinical practice. As a hybrid technique, PAI uniquely combines the advantages of optical excitation and of acoustic detection. Optical absorption provides a rich contrast mechanism from either endogenous chromophores or exogenous contrast agents. Because ultrasound scatters much less than light in tissue, PAI generates high-resolution images in both the optical ballistic and diffusive regimes, overcoming the limitations imposed by light scattering in deep biological tissues. PAI has led to a variety of exciting discoveries and applications from laboratory research to clinical patient care.

To translate photoacoustic technology from the bench to the bedside, this thesis focuses on efforts to increase the imaging depth, provide clinically useful information (i.e., relevant imaging contrast), reduce system size, and improve system reliability. Assisted by powerful pulsed lasers and advanced data acquisition circuits, modern PAI has achieved applications such as functional imaging of the whole rat brain, revealing detailed angiography and functional connectivity at high spatiotemporal resolution. The advancement of deep imaging in small animal PAI has been transferred to human breast and brain imaging, showing early promise for clinical practice. To further extend the imaging depth and provide dielectric imaging contrast, microwave-based thermoacoustic tomography has been demonstrated *in vivo*. To map further physiological contrasts, spectroscopic PAI has been performed to image the oxygenation states of hemoglobin and myoglobin. In addition to the effort towards deep penetration and multiple contrasts, benchtop photoacoustic microscopy has been minimized to a handheld probe for human

skin imaging. As a rapidly evolving imaging technology, PAI is being translated from the bench to the bedside and promises exciting and useful clinical applications.

PUBLISHED CONTENT AND CONTRIBUTIONS

1. **Li Lin**[†], Peng Hu[†], Junhui Shi[†], Catherine M. Appleton, Konstantin Maslov, Lei Li, Liren Zhu, Ruiying Zhang, and Lihong V. Wang. Single-breath-hold photoacoustic computed tomography of the breast. *Nature Communications* **9**(1), 2018. DOI:10.1038/s41467-018-04576-z.

Li Lin participated in the conception of the study, designed and constructed the hardware system, performed the experiments, analyzed the data, and wrote the manuscript.

2. **Li Lin**[†], Pengfei Zhang[†], Song Xu, Junhui Shi, Lei Li, Junjie Yao, Lidai Wang, Jun Zou, and Lihong V. Wang. Handheld optical-resolution photoacoustic microscopy. *Journal of Biomedical Optics* **22**(4), 2017. DOI: 10.1117/1.JBO.22.4.041002.

Li Lin participated in the conception of the study, designed and constructed the hardware system, performed the experiments, and wrote the manuscript.

3. **Li Lin**[†], Junjie Yao[†], Ruiying Zhang, Chun-Cheng Chen, Chih-Hsien Huang, Yang Li, Lidai Wang, William Chapman, Jun Zou, and Lihong V. Wang. High-speed photoacoustic microscopy of mouse cortical microhemodynamics. *Journal of Biophotonics* **10**(6-7), 2017. DOI: 10.1002/jbio.201600236.

Li Lin participated in performing the experiments, analyzed the data, and wrote the manuscript.

4. **Li Lin**, Junjie Yao, Lei Li, and Lihong V. Wang. In vivo photoacoustic tomography of myoglobin oxygen saturation. *Journal of Biomedical Optics* **21**(6), 2016. DOI: 10.1117/1.JBO.21.6.061002.

Li Lin participated in the conception of the study, performed the experiments, analyzed the data, and wrote the manuscript.

5. **Li Lin**, Jun Xia, Terence T.W. Wong, and Lihong V. Wang. In vivo deep brain imaging of rats using oral-cavity illuminated photoacoustic computed tomography. *Journal of Biomedical Optics* **20**(1), 2015. DOI: 10.1117/1.JBO.20.1.016019.

Li Lin participated in the conception of the study, performed the experiments, analyzed the data, and wrote the manuscript.

6. Lei Li[†], Liren Zhu[†], Cheng Ma[†], **Li Lin**[†], Junjie Yao, Lidai Wang, Konstantin Maslov, Ruiying Zhang, Wanyi Chen, Junhui Shi, and Lihong V. Wang. Single-impulse panoramic photoacoustic computed tomography of small-animal whole-body

dynamics at high spatiotemporal resolution. *Nature Biomedical Engineering* **1**(5), 2017. DOI: 10.1038/s41551-017-0071.

Li Lin participated in performing the experiments and analyzed the data.

7. Parker Wray[†], **Li Lin**[†], Peng Hu, and Lihong V. Wang. Photoacoustic computed tomography of human extremities. *Journal of Biomedical Optics*, **24**(2), 2019. DOI: 10.1117/1.JBO.24.2.026003.

Li Lin conceived and designed the study, constructed the hardware system, participated in performing the experiments, and analyzed the data.

8. Kristine Ravina, **Li Lin**, Charles Y. Liu, Lihong V. Wang, and Jonathan J. Russin. Prospects of photo- and thermoacoustic imaging in neurosurgery. *Neurosurgery*, nyz420, 2019. DOI: 10.1093/neuros/nyz420.

Li Lin provided the data and participated in the writing of the manuscript.

9. An Yan, **Li Lin**, Changjun Liu, Junhui Shi, Shuai Na, and Lihong V. Wang. Microwave-induced thermoacoustic tomography through an adult human skull. *Medical Physics*, **46**(4), 2019. DOI: 10.1002/mp.13439.

Li Lin conceived and designed the study, constructed the hardware system, participated in performing the experiments, and analyzed the data.

10. An Yan, **Li Lin**, Shuai Na, Changjun Liu, and Lihong V. Wang. Large field homogeneous illumination in microwave-induced thermoacoustic tomography based on a quasi-conical spiral antenna. *Applied Physics Letters*, **113**(2), 2018. DOI: 10.1063/1.5043541.

Li Lin designed the study and constructed the hardware system.

11. Pengfei Zhang, Lei Li, **Li Lin**, Junhui Shi, and Lihong Wang. In vivo super-resolution photoacoustic computed tomography by localization of single dyed droplets. *Light: Science & Applications*, **8**(36), 2019. DOI: 10.1038/s41377-019-0147-9.

Li Lin participated in performing the experiments.

12. Jeffrey Cochran, David Busch, **Li Lin**, David Minkoff, Martin Schweiger, Simon Arridge, and Arjun Yodh. Hybrid time-domain and continuous-wave diffuse optical tomography instrument with concurrent, clinical MRI for breast cancer imaging. *Journal of Biomedical Optics*, **24**(5), 2019. DOI: 10.1117/1.JBO.24.5.051409.

Li Lin participated in performing the experiments.

13. Pengfei Zhang, Lei Li, **Li Lin**, Peng Hu, Junhui Shi, Yu He, Liren Zhu, Yong Zhou, and Lihong V. Wang. High-resolution deep functional imaging of the whole mouse

brain by photoacoustic computed tomography in vivo. *Journal of Biophotonics* **11**(1), 2017. DOI: 10.1002/jbio.201700024.

Li Lin participated in performing the experiments.

14. Yu He, Changjun Liu, **Li Lin**, and Lihong V. Wang. Comparative effects of linearly and circularly polarized illumination on microwave-induced thermoacoustic tomography. *IEEE Antennas and Wireless Propagation Letters* **16**, 2017. DOI: 10.1109/LAWP.2017.2652853.

Li Lin participated in the conception of the study and performed the experiments.

15. Terence T.W. Wong, Yong Zhou, Alejandro Garcia-Uribe, Lei Li, Konstantin Maslov, **Li Lin**, and Lihong V. Wang. Use of a single xenon flash lamp for photoacoustic computed tomography of multiple-centimeter-thick biological tissue ex vivo and a whole mouse body in vivo. *Journal of Biomedical Optics* **22**(4), 2017. DOI: 10.1117/1.JBO.22.4.041003.

Li Lin constructed the hardware system.

† Equal contribution.

TABLE OF CONTENTS

ACKNOWLEDGMENTS.....	iii
DEDICATION.....	iv
ABSTRACT	v
PUBLISHED CONTENT AND CONTRIBUTIONS.....	vii
TABLE OF CONTENTS	x
LIST OF ILLUSTRATIONS AND/OR TABLES	xii
LIST OF FREQUENTLY USED ABBREVIATIONS.....	xvii
Chapter I INTRODUCTION.....	1
Motivation.....	1
Fundamentals of PAI	2
Major Implementations of Multiscale PAI	5
Dissertation outline	9
Chapter II PACT OF RAT BRAIN	12
Introduction and Motivation	12
Oral-cavity illuminated PACT of Rat Brain	13
Rat Whole Brain Functional Imaging by Single-Impulse Panoramic PACT	17
Summary and Outlook	19
Chapter III PACT OF HUMAN BREAST CANCER.....	20
Introduction and Motivation	20
System Construction and Characteristics.....	23
SBH-PACT of Healthy Breast Anatomy and Dynamics	27
SBH-PACT of Breast Cancer Anatomy, Segmentation, and Elastography.....	29
Assessing Breast Cancer Response to Neoadjuvant Chemotherapy.....	36
Data Process and Analysis Methods	38
Chapter IV 3D PACT OF HUMAN BRAIN	45
Introduction and Motivation	45
System Construction and Characteristics.....	46
Geometric Correction in 3D-PACT	48
In Vivo 3D PACT	51
Chapter V MICROWAVE-BASED THERMOACOUSTIC TOMOGRAPHY	54

Introduction and Motivation	54
Experimental Setup	55
Results	57
Summary and Outlook	60
Chapter VI MULTI-CONTRAST PACT—MYOGLOBIN	61
Introduction and Motivation	61
Results	63
Discussion	69
Chapter VII HIGH-SPEED OR-PAM OF CORTICAL HEMODYNAMICS	70
Introduction and Motivation	70
High-speed OR-PAM of blood flow redistribution in mini-stroke models	74
High-speed OR-PAM of cerebral autoregulation	77
Discussion	80
Chapter VIII HANDHELD OR-PAM	81
Motivation	81
System Construction and Characteristics	82
Results	85
Summary	87
Chapter IX CONCLUSIONS AND OUTLOOK	88
BIBLIOGRAPHY	90

LIST OF ILLUSTRATIONS AND/OR TABLES

List of Figures

<i>Number</i>	<i>Page</i>
Figure 1. Dissertation outline.....	10
Figure 2. Experimental setup of the oral-cavity illuminated PA computed tomography (OI-PACT) system: (a) Schematic of the OI-PACT system. (b) Detailed view of the optical fiber tip in the rat’s mouth. The origin of the z-axis was aligned with the plane 3 mm above the fiber tip.....	14
Figure 3. A series of images acquired at $z = -1$ mm (a), $z = 1$ mm (b), and $z = 4$ mm (c), with control images at the same layers (d)–(f) acquired by external illumination through the top skull. (g) In vivo PA image of the rat brain base ($z = 0$ mm) acquired by OI-PACT. (h) Corresponding photograph of the anatomy of the same rat brain. ACA, anterior cerebral artery; BS, brain stem; BMI, bone-muscle interface; CE, cerebellum; CM, cerebral medulla; CO, colliculus; HY, hypothalamus; LCH, left cerebral hemisphere; OL, olfactory lobes; RCH, right cerebral hemisphere; and TH, thalamus.	17
Figure 4. (a) Setup of the rat brain imaging. The rat head was mounted vertically during imaging and 1064-nm light was obliquely delivered to the rat cortex. (b) Rat whole-brain vasculature in different coronal planes (From ~bregma -1 mm to -4 mm). (c) Seed-based functional connectivity analyses of different functional regions on both sides of the brain before the stroke surgery. (d) Seed-based functional connectivity analyses the brain after the stroke surgery.	18
Figure 5. Representations of the SBH-PACT system. (a) Perspective cut-away view of the system with data acquisition components removed. (b) Perspective view of the system with patient bed and optical components removed. (c) Signal flow diagram for the system. (d) Photograph of the system. DAQ, data acquisition system; Pre-amp, pre-amplifier circuits.....	23
Figure 6. Simulation of the optical fluence in breast tissue at 2 cm depth, produced by different illumination schemes. (a) Distribution of the optical fluence in breast tissue when the illumination beam is donut-shaped. After removing the engineered diffuser, the ring diameter is approximately 6 cm. (b) Distribution of the optical fluence in breast tissue at the same depth when the illumination beam is Gaussian-shaped. The FWHM of the beam is approximately 6 cm. To mimic a breast compressed against the chest wall, we built a cylindrical breast model with a height of 4 cm and a diameter of 15 cm. In this numerical model, the absorption coefficient (0.05 cm^{-1}) and the reduced scattering coefficient (7 cm^{-1}) inside the breast were selected for a 1064 nm wavelength [58].	24
Figure 7. (a) The raw radio frequency signal from each ultrasonic transducer element corresponding to a point PA source at the center of the full-ring array. The black solid line represents the mean value of all transducer elements’ responses, and the gray region represents the standard deviation (STD) across the elements. (b) Fourier transform amplitude of each RF signal in (a), showing that the bandwidth of the transducer array is about 2.16 MHz. The point source was created by fixing a carbon particle (20–50 μm) in an agar phantom. The particle was small enough to be regarded as a spatial point source for the SBH-PACT system. (c) A maximum amplitude projection (MAP) image of two crossed tungsten wires, each with a nominal diameter	

of 13 μm . (d) The PA amplitude distribution along the red dashed line in (c). The in-plane resolution, defined as the FWHM of the amplitude distribution, is 255 μm26

Figure 8. Quantification of elevational resolution. (a) Simulated acoustic diffraction field in the elevational direction. (b) Line profile in the elevational direction of a carbon particle (20–50 μm , placed at the ring center) reconstructed by 2D back-projection. (c) Line profile in the elevational direction of the same carbon particle reconstructed by 3D back-projection.27

Figure 9. SBH-PACT of healthy breasts. (a) Vasculature in the right breast of a 27-year-old healthy female volunteer. Images at four depths are shown in increasing depth order from the nipple to the chest wall. (b) The same breast image with color-encoded depths. (c) A close-up view of the region outlined by the magenta dashed box in (b), with selected thin vessels and their line spread plots. (d) A selected vessel tree with five vessel bifurcations, labeled from B1 to B5. At each bifurcation, the diameter relationships between the parent vessel (D_{parent}) and daughter vessels ($D_{daughter}$) are presented on the right. X_B is the junction exponent, and R_B is defined as $R_B = D_{parent}^3 / (D_{daughter_a}^3 + D_{daughter_b}^3)$. (e) Heartbeat-encoded arterial network mapping of a breast cross-sectional image (red = artery, blue = vein). (f) Amplitude fluctuation in the time domain of the two pixels highlighted by yellow and green dots in e. The pixel value in the artery shows changes associated with arterial pulse propagation. (g) Fourier domain of the pixel value fluctuations in f. The oscillation of the arterial pixel value shows the heartbeat frequency at ~ 1.2 Hz.28

Figure 10. SBH-PACT of cancerous breasts. (a) X-ray mammograms of the affected breasts of seven breast cancer patients. LCC left cranial-caudal, LLM left lateral-medio, LML left mediolateral, LMLO left mediolateral-oblique, RCC right cranial-caudal, RML right medio-lateral. (b) Depth-encoded angiograms of the eight affected breasts acquired by SBH-PACT. Breast tumors are identified by white circles. For illustration, we marked the nipple of the first patient (P1) with a magenta circle. P1—48-year-old female patient with an invasive lobular carcinoma (grade 1/3); P2—70-year-old female patient with a ductal carcinoma in situ (microinvasion grade 3/3); P3—35-year-old female patient with two invasive ductal carcinomas (grade 3/3); P4—71-year-old female patient with an invasive ductal carcinoma (grade 3/3); P5—49-year-old woman with a stromal fibrosis or fibroadenoma; P6—69-year-old female patient with an invasive ductal carcinoma (grade 2/3); P7—44-year-old female patient with a fibroadenoma in the right breast and an invasive ductal carcinoma (grade 2/3) in the left breast. (c) MAP images of thick slices in sagittal planes marked by white dashed lines in (b). (d) Automatic tumor detection on vessel density maps. Tumors are identified by green circles. Background images in gray scale are the MAP of vessels deeper than the nipple. (e) Maps of the relative area change during breathing in the regions outlined by blue dashed boxes in the angiographic images in d. The same tumors are identified by red circles. The elastographic study began with Patient 4, and it revealed all imaged tumors, including the undetected one in (d) (P7(L)).32

Figure 11. SBH-PACT elastography of a breast mimicking phantom. (a) Cross-sectional image of the phantom acquired by SBH-PACT. Hundreds of chopped human hairs were uniformly distributed in the phantom to mimic small blood vessels. To mark the location for comparison, two crossed tungsten wires (indicated by yellow arrows) were placed inside the ball (enclosed by the red dashed circle), which had a higher agar concentration to mimic a breast tumor. (b) SBH-PACT elastographic image of the same

	cross section. Identified by the red dashed circle, the location of the agar ball is revealed correctly.	33
Figure 12.	Statistics. (a) The ROC curves of breast tumor detection based on blood vessel density. σ , STD. (b) The average vessel density in each tumor and surrounding normal breast tissue. (c) The relative area change in each tumor and surrounding normal breast tissue caused by breathing. The elastographic study was started with Patient 4. (d) The longest dimension and center depth of each tumor.	35
Figure 13.	SBH-PACT of a patient before and after the 2-cycle NAC treatments.	37
Figure 14.	Vascular diameter quantification. (a) (left) Numerically simulated image of a cylinder with a diameter of 3 mm. (right) Experimental image of a rubber cylinder with a pre-known diameter of 3 mm. (b) Photoacoustic amplitude distributions along the normal directions (yellow dashed lines) of the numerical cylinder and the rubber cylinder. (c) Correlation coefficients between numerical cylinders with different diameters and the rubber cylinder. (d) (left) Numerically simulated image of a cylinder with a diameter of 1.04 mm. (right) <i>In vivo</i> image of a section of a human blood vessel. (e) Photoacoustic amplitude distributions along the normal directions (yellow dashed lines) of the numerical cylinder and the blood vessel. (f), Correlation coefficients between numerical cylinders with different diameters and the blood vessel.	40
Figure 15.	3D-PACT system. (a) Photograph of the 3D-PACT system. The whole system is mounted on wheels. (b) Photograph of the system with the bed top and side panels removed. (c) Closeup view of the ultrasonic transducer arrays. (d) Cut-away view of the system schematic.	47
Figure 16.	Radial calibration factor α_n of each ultrasonic transducer element.	50
Figure 17.	MAP images of a leaf skeleton reconstructed before and after geometric correction.	51
Figure 18.	MAP images of a healthy human breast acquired by 3D-PACT within a single breath hold of 10 seconds.	52
Figure 19.	3D-PACT of a healthy human head. (a) Photograph of a healthy subject being imaged. (b) MAP images of a healthy human head acquired by 3D-PACT within 10 seconds.	52
Figure 20.	Penetration depths of various biological tissues versus the microwave frequency.	55
Figure 21.	(a) Schematic of the experimental TAT system. (b) Simulated electric field distribution in a plane 4.5 cm above the antenna. (c) Photograph of the ultrasonic transducer shielded with metal mesh.	56
Figure 22.	Diagrams of TAT signals acquired before and after shielding.	58
Figure 23.	Two phantom photographs and their cross-sectional images acquired by TAT. ...	58
Figure 24.	Cross-sectional images of the rat's trunk. (a) TAT image and the corresponding photograph. (b) TAT images of the rat's trunk at different cross sections.	59
Figure 25.	Transcranial TAT. (a) Normalized spectrum of the transcranial thermoacoustic signal. (b) Transcranial TAT image of the agar.	60
Figure 26.	Optical absorption properties of myoglobin. (a) Absorption spectra of major chromophores found in muscle, measured at wavelengths from 600 nm to 820 nm. (b) Absorption spectra of a mixture of MbO ₂ (60.7%), Mb (24.8%), HbO ₂ (6.9%), and Hb	

	(7.6%), measured using a spectrophotometer before and after the photoacoustic experiment.	63
Figure 27.	Experimental setup and a representative PA image of the phantom. (a) Schematic of the phantom setup. (b) Photoacoustic image of the phantom acquired at 600 nm.	64
Figure 28.	Schematic of the experimental setup for <i>in vivo</i> sO ₂ measurement in backbone muscle.	67
Figure 29.	<i>In vivo</i> experimental results. (a-b) Concentration fraction of myoglobin (a) and hemoglobin (b) in hyperoxia (state <i>a</i>) (shown in color) overlaid on the structural image (shown in gray). (c-d) The relative change in myoglobin sO ₂ (c) and hemoglobin sO ₂ (d) from hyperoxia (state <i>a</i>) to hypoxia (state <i>b</i>) (shown in color) overlaid on the structural image (shown in gray). BM, backbone muscle; KN, kidney; SC, spinal cord.	68
Figure 30.	Schematic of the high-speed OR-PAM.	72
Figure 31.	High-speed OR-PAM of ischemic mini-stroke dynamics in a mouse brain. (a) OR-PAM image of a 1 mm by 1 mm cortical area, where spontaneous bleeding was observed in the boxed region. (b) Zoomed-in images of the bleeding region, showing a capillary bifurcation composed of a parent vessel (P) and two daughter vessels (D1 and D2). Spontaneous bleeding was observed at daughter vessel D1. (c) The time course of the bleeding dynamics, which shows that the bleeding halftime was 4.0 seconds and the extravascular blood was cleared with a halftime of 38.2 seconds. On the fitted curve, the halftime is the time duration from the baseline to half of the peak or from the peak to half of the peak. (d) The PA signals from the parent vessels and daughter vessels show the blood volume redistribution after the bleeding, with the loss of the blood volume in the bleeding daughter vessel D1 compensated by the blood volume increase in the intact daughter vessel D2.	74
Figure 32.	Blood flow dynamics in response to vessel occlusion. A CW laser at 650 nm was focused at the lumen of a vessel to induce photothrombosis. (a) The occlusion region is marked by the dashed circle. Snapshots are shown before, during, and after the occlusion. (b) Line scanning at the bifurcation, consisting of a parent vessel (P) and two daughter vessels (D1 and D2), shows a reduced flow speed in the parent vessel and the reverse flow in the daughter vessel (D1). (c-d) Line scanning images of the parent vessel (c) and one daughter vessel (d) before and after the occlusion, which show the blood flow slowing down in the parent vessel and reversing in the daughter vessel.	76
Figure 33.	Amoeboid structures (indicated by arrows) were observed in the damaged regions after hemorrhage and vessel occlusion.	77
Figure 34.	High-speed OR-PAM of mouse brain autoregulation in response to phenylephrine. (a-b) PA images of a 2 mm by 3 mm cortical area before (a) and after (b) the intravenous tail vein injection of phenylephrine, a vasoconstriction agent. While the brain autoregulation maintained the diameters of the majority of vessels, blood perfusion to a sub-population of vessels was completely stopped. (c) The relative PA signal change between the close-ups in (a) and (b), showing the vessels with stopped blood perfusion. (d) Automatic vessel segmentation was used to quantify the vessel diameters. (e) The statistical results show no significant difference in the vessel diameters in the mouse brain before and after the injection of phenylephrine. (f) A comparative study performed in the mouse ear shows clear vasoconstriction (marked by arrows) after the injection. (g) The statistical results also confirmed the decrease in vessel diameters in the mouse ear after the injection. Statistics: paired Student's t-test.	

*** $p < 0.001$, $n = 3$. (h) Averaged diameter changes of representative vessel segments in the mouse brain and ear in response to phenylephrine. B1 and B2 are brain vessel segments marked in the close-up in (a), and E1 is an ear vessel segment marked in (f). While the diameter of E1 steadily decreased after the injection, the diameter of B1 remained constant and the blood perfusion in B2 stopped.....78

Figure 35. Schematic of the OR-PAM handheld probe. (a) 2-D sketch of the optical and acoustic beams in the probe. UT, ultrasound transducer; AC, aluminum coating; AL, acoustic lens. (b) 3-D rendering of the OR-PAM handheld probe. The front and the left side panels are removed for better visualization.83

Figure 36. Characteristics of the handheld OR-PAM probe. (a) Lateral resolution measurement by imaging a sharp edge. Solid squares: the PA amplitude when the laser beam was scanned across the edge. Solid curve: the fit of the measured data to an error function. Dashed line: the extracted Gaussian-shaped line spread function. (b) Penetration depth measured by a hair embedded in an optical scattering medium mimicking skin tissue. The acoustic attenuation has been compensated for by multiplying the PA signal by a depth-dependent exponential correction factor. The gray bar shows the normalized PA signal amplitude.....84

Figure 37. Hemoglobin concentration monitoring in the vessels in a mouse ear after tail vein injection of 0.9% saline. (a) Representative images recorded at different time points after the injection of 0.6 mL saline. The stamps on the images indicate the time (min:s) after the injection. (b) The signal from the blood vessels within the dashed box in (a) as a function of time. The injection procedure lasted 75 s.85

Figure 38. OR-PAM of the human skin by the handheld probe. (a) OR-PAM image of capillaries in a cuticle. (b) Photograph of the OR-PAM handheld probe imaging a red mole on a volunteer’s leg. (c) Photograph of the mole. (d) OR-PAM image of the mole. The color bar shows the normalized PA signal amplitude.....87

List of Tables

<i>Number</i>	<i>Page</i>
Table 1. Summary of the phantom experiment results.	66

LIST OF FREQUENTLY USED ABBREVIATIONS

ANSI: American National Standards Institute
AR-PAM: Acoustic-resolution photoacoustic microscopy
BBB: Blood brain barrier
BOLD: Blood oxygenation level dependent
CA: Cerebral autoregulation
CW: Continuous wave
DAQ: Data acquisition
DOT: Diffuse optical tomography
fMRI: Functional magnetic resonance imaging
FOV: Field of view
FWHM: Full width at half maximum
HbO₂: Oxy-hemoglobin
Hb: Deoxy-hemoglobin
MAP: Maximum amplitude projection
MEMS: Microelectromechanical system
MbO₂: Oxy-myoglobin
Mb: Deoxy-myoglobin
MRI: Magnetic resonance imaging
NA: Numerical aperture
NIR: Near infrared
OPO: Optical parametric oscillator
OR-PAM: Optical-resolution photoacoustic microscopy
PA: Photoacoustic
PACT: Photoacoustic computed tomography
PAI: Photoacoustic imaging
PAM: Photoacoustic microscopy
RBC: Red blood cell
ROC: Receiver operating characteristic
SAR: Specific absorption rate
SBH-PACT: Single-breath-hold photoacoustic computed tomography

SIP-PACT: Single-impulse panoramic photoacoustic computed tomography

SNR: Signal-to-noise ratio

sO₂: Hemoglobin oxygen saturation

sO₂-Mb: Oxygen saturation of myoglobin

STD: standard deviation

TAT: Thermoacoustic tomography

UBP: Universal back-projection

1D: One-dimensional

2D: Two-dimensional

3D: Three-dimensional

Chapter I

INTRODUCTION

Motivation

With recent advances in photonics and optical molecular probes, optical imaging plays an increasingly important role in preclinical and clinical imaging. The manner in which light is scattered and absorbed in tissues can provide both structural and functional information in biomedical contexts. A fundamental constraint in pure optical imaging is light diffusion, which limits the spatial resolution in deep-tissue imaging. Consequently, pure optical imaging methods fall into two categories: ballistic (minimally scattered) optical microscopy and diffuse (multi-scattered) optical tomography. The former provides fine resolution but with a low imaging depth in tissue—up to ~ 1 mm, as defined by the optical diffusion limit [1]. In contrast, diffuse optical tomography (DOT) can probe centimeters into tissue, but the scrambled paths of the diffuse photons render the image reconstruction mathematically ill-posed with poor spatial resolution [2]. It remains a challenge for pure optical imaging to attain fine spatial resolution at depths beyond the optical diffusion limit.

Fortunately, photons in tissue can be converted into ultrasonic waves, which are scattered approximately 1,000 times less than optical scattering. Based on the photoacoustic (PA) effect, absorption of photons by biomolecules thermoelastically induces a pressure rise which propagates as ultrasonic waves. The amplitude of the ultrasonic wave is proportional to the optical absorption. Photoacoustic imaging (PAI) forms high-resolution images by detecting the low-scattered ultrasonic waves and consequently revealing the optical absorption as the imaging contrast. Accordingly, PAI combines the advantages of both

optical excitation and acoustic detection. The conversion from optical to ultrasonic energy brings multiple inherent advantages: (1) the low acoustic scattering enables PAI to break through the optical diffusion limit and achieves multiscale high-resolution imaging of biological structures ranging in size from organelles to organs; (2) rich optical contrast based on chemical compositions, which express wavelength-dependent light absorption; (3) PAI provides background-free detection because non-absorbing tissue components present no background [3]; (4) PAI is speckle free [4].

PAI also has unique advantages when compared with other mainstream biomedical imaging modalities, making a broad impact both in preclinical studies and clinical practice: (1) compared with ultrasonic imaging, PAI has rich intrinsic and extrinsic optical contrasts and is free of speckle artifacts; (2) compared with X-ray computed tomography and positron emission tomography, PAI uses nonionizing laser illumination; (3) compared with magnetic resonance imaging (MRI), PAI is faster and less expensive.

Fundamentals of PAI

In PAI, a short-pulsed (usually in nanoseconds) light source is typically used to irradiate the tissue. Following the temporally confined optical absorption, an initial temperature rise induces a pressure rise. The pressure rise is proportional to the temperature rise and propagates as an ultrasonic wave (i.e., PA wave). Approximately, a 1-mK temperature rise results in an 800-Pa pressure rise, which is on the order of the noise level of a typical ultrasonic transducer. If the pulse duration is shorter than the thermal relaxation time and the stress relaxation time, the excitation satisfies both thermal and stress confinements and the initial pressure rise p_0 can be expressed as:

$$p_0 = \Gamma \eta_{th} \mu_a F, \quad (1)$$

where Γ is the Gruneisen parameter (dimensionless) and η_{th} denotes the percentage of absorbed light converted into heat. They are usually approximated as constants, although Γ has been found to increase with equilibrium temperature, enabling PAI to image temperature with a sensitivity of 0.16 °C — useful for monitoring thermal therapy [5]. μ_a is the optical absorption coefficient (cm^{-1}) and F represents the local optical fluence (J/cm^2), also called radiant exposure. Therefore, if p_0 can be measured and F is known, μ_a can be recovered. Since p_0 is linearly proportional to the local optical fluence F , increasing the optical fluence within the safety limit is always preferable for obtaining higher signal-to-noise ratio (SNR) in PA images. Averaging PA signals will also improve the SNR, which, however, is proportional to the square root of the signal averaging times.

After the generation of the initial pressure p_0 , an acoustic wave starts to propagate at the speed of sound (v_s) in the material. The propagation in an inviscid medium can be described by a general PA equation in the time-domain [6]:

$$\left(\nabla^2 - \frac{1}{v_s^2} \frac{\partial^2}{\partial t^2} \right) p(\vec{r}, t) = - \frac{\beta}{C_p} \frac{\partial H(\vec{r}, t)}{\partial t}, \quad (2)$$

where $p(\vec{r}, t)$ is the acoustic pressure at position \vec{r} and time t . β and C_p denote the isothermal compressibility and specific heat capacity at constant pressure, respectively. $H(\vec{r}, t)$ is the heating function defined as the thermal energy converted per unit volume and per unit time; it is related to the optical fluence rate Φ by $H = \eta_{th} \mu_a \Phi$. Solving Eq. (2) with the Green's function approach, the delta heating response of an arbitrary absorbing object is:

$$p(\vec{r}, t) = \frac{1}{4\pi v_s^2} \frac{\partial}{\partial t} \left\{ \frac{1}{v_s t} \int d\vec{r}' p_0(\vec{r}') \delta\left(t - \frac{|\vec{r} - \vec{r}'|}{v_s}\right) \right\}. \quad (3)$$

For an ideal point transducer placed at \vec{r}_d , the detected PA signal can be written by reforming Eq. (3) as:

$$p_d(\vec{r}_d, t) = \frac{\partial}{\partial t} \left\{ \frac{t}{4\pi} \iint_{|\vec{r}_d - \vec{r}| = v_s t} p_0(\vec{r}) d\Omega \right\}, \quad (4)$$

where $d\Omega$ is the solid-angle element of \vec{r} with respect to the point at \vec{r}_d . Eq. (4) indicates that the detected pressure at time t comes from sources over a spherical shell centered at the detector position \vec{r}_d with a radius $v_s t$. The initial pressure distribution $p_0(\vec{r})$ can be obtained by inverting Eq. (4). The so-called universal back-projection (UBP) algorithm for image reconstruction can be expressed in the temporal domain as:

$$p_0(\vec{r}) = \frac{1}{\Omega_0} \int_S d\Omega_0 \left\{ 2p_d(\vec{r}_d, t) - 2t \frac{\partial p_d(\vec{r}_d, t)}{\partial t} \right\} \Bigg|_{t = |\vec{r}_d - \vec{r}|/v_s}. \quad (5)$$

Here, Ω_0 is the solid angle of the whole detection surface S with respect to a given source point at \vec{r} . Eq. (5) indicates that the initial pressure $p_0(\vec{r})$ can be obtained by back-projecting the filtered data, $\left\{ 2p_d(\vec{r}_d, t) - 2t \frac{\partial p_d(\vec{r}_d, t)}{\partial t} \right\}$, onto a collection of concentric spherical surfaces that are centered at each transducer location \vec{r}_d , with $d\Omega_0/\Omega_0$ as the weighting factor applied to each backprojection. The first derivative with respect to time represents a ramp filter, which suppresses low frequency signals. The UBP reconstruction algorithm is essentially a method for sophisticated triangulation of PA sources from the time-resolved acoustic signals [7]. We note that UBP assumes the medium is acoustically lossless and homogeneous. Significant acoustic inhomogeneity of the sample may introduce reconstruction distortions, which, however, may be corrected or minimized using modified algorithms that take into account the acoustic inhomogeneity [8].

Major Implementations of Multiscale PAI

The elegant marriage between light and sound endows PAI with the unique capability of scaling its spatial resolution and imaging depth across both optical and ultrasonic dimensions. Currently, PAI has two major implementations: focused-scanning photoacoustic microscopy (PAM) and photoacoustic computed tomography (PACT). While PAM usually aim to image millimeters deep at micrometer-scale resolution, PACT can be implemented for both mesoscopic and macroscopic resolution with centimeter imaging depth. Microwave-induced thermoacoustic tomography (TAT) is a macroscopic imaging modality that bears resemblance to PACT. Instead of using light, TAT utilizes microwaves for excitation, providing deeper penetration with dielectric contrast.

Photoacoustic Microscopy

In PAM, both the optical excitation and ultrasonic detection are focused, and the dual foci are usually configured confocally to maximize sensitivity. Volumetric imaging is realized by two-dimensional (2D) raster scanning of the dual foci of optical excitation and ultrasonic detection. At each scanning position, a laser pulse excites tissue predominantly along a line in the elevational direction and the ultrasonic transducer receives PA signals along the line and records the time-of-arrival, producing a one-dimensional (1D) depth-resolved image (A-line). Accordingly, a 2D transverse scanning generates a three-dimensional (3D) image. While the depth information is resolved by the acoustic time of flight, the lateral resolution is determined by the product of the point spread functions of the light illumination and acoustic detection. Depending on whether the optical or ultrasonic focus is finer, PAM is further classified into optical-resolution (OR) and acoustic-resolution (AR) PAM.

In OR-PAM, the laser beam is focused by a microscope objective to a diffraction-limited spot, whose diameter can range from several hundred nanometers to several micrometers, depending on the numerical aperture (NA_{opt}) of the optical focusing lens, the wavelength (λ_{opt}) of the excitation beam, and the desired imaging depth. In typical OR-PAM, the objective forms an Airy diffraction pattern whose full width at half maximum (FWHM) size determines the lateral resolution (R_{OR-PAM}):

$$R_{OR-PAM} = 0.51 \frac{\lambda_{opt}}{NA_{opt}}. \quad (6)$$

Relying on the tight optical focus, the penetration of an OR-PAM system is limited to about one transport mean free path in tissue [9]. By using longer optical wavelengths, which have longer transport mean free paths, the penetration limit can be increased.

At depths beyond the optical diffusion limit and up to a few millimeters, AR-PAM achieves high resolution by taking advantage of the much lower acoustic scattering. Despite the loosely-focused laser beam, lateral resolution (R_{AR-PAM}) of tens of micrometers is achieved by diffraction-limited acoustic detection:

$$R_{AR-PAM} = 0.71 \frac{\lambda_{Act}}{NA_{Act}}, \quad (7)$$

where λ_{Act} and NA_{Act} denote the center wavelength of the acoustic wave and the numerical aperture of the ultrasonic detector, respectively.

In both PAM configurations, the axial resolution is given by the corresponding distance of the FWHM of the temporal signal envelope. Accordingly, if the impulse response of the ultrasonic transducer has a Gaussian envelope, the axial resolution can be estimated as $0.88v_s/B$, where B is the ultrasonic transducer bandwidth which is approximately

proportional to the central frequency. Increasing the bandwidth for better axial resolution will decrease the maximum imaging depth since higher frequency ultrasound has greater attenuation in biological tissues. To convert each PA signal to a depth-resolved image, the Hilbert transformation is normally used to extract the envelope of the short-pulsed PA signal. Because the transducer is focused in PAM and each signal acquired by the transducer directly represents a 1D image after Hilbert transformation, UBP is usually not applied to PAM.

Photoacoustic Computed Tomography

Rather than relying on raster scanning as in PAM, PACT uses an array of ultrasonic transducers to detect PA waves emitted from an object at multiple view angles simultaneously, allowing a much faster cross-sectional or volumetric imaging speed at the expense of system and computational costs. In PACT, the entire region of interest is excited by an expanded laser beam for wide-field illumination.

After the acoustic waves are detected by the transducers, various reconstruction algorithms can be applied for PACT image formation [10]. The UBP based on Eq. (5) is commonly utilized because of its high accuracy and ease of implementation. In the reconstructed images, tissue interfaces are important for identifying organ boundaries. Because each boundary is composed of small flat segments and each segment transmits acoustic waves along the two opposite directions perpendicular to it, a boundary can be well-reconstructed if the local normal directions of the boundary pass through the transducers [11]. Therefore, the detection surface with respect to the imaging object should be 2π radians and 4π steradians to exactly reconstruct an arbitrary boundary in 2D and 3D, respectively. The UBP reconstruction algorithm can be extended straightforwardly to the limited-angle view

case, in which the reconstruction may be incomplete and reconstruction artifacts may occur. The solid-angle weighting factor in the UBP Eq. (5), however, can compensate for the variations in the detection views. Ultrasonic transducer arrays with various populating patterns, such as line, plane, half ring, full ring, and hemisphere, have been employed and demonstrated in both animal and clinical applications.

There are a few important factors a researcher/engineer should consider when building a PACT system: (1) high optical fluence within the safety limit is preferable for high SNR. Since PACT reconstruction assumes light has a uniform or predictable distribution, light illumination needs to be carefully designed. Positioning of the imaging object should also be considered for desirable light illumination; (2) a large view angle of the transducer array or detection aperture is helpful to minimize the loss of information and improve the image quality; (3) since PA signals generated from the deep tissue could suffer both light and acoustic attenuation, analog preamplifiers connected between the array and data acquisition systems (DAQ) can amplify the weak PA signals before cable noise compromises the SNR; (4) in addition to the temporal Nyquist sampling law, one should also consider the spatial Nyquist sampling criterion. Inadequate spatial sampling will result in limited field of view (FOV) and undersampling artifacts; (5) high imaging speed is helpful to reduce the motion-induced artifacts. Although co-registration methods can partially mitigate the motion distortion, the non-rigidity of the biological tissue compromises the effectiveness; (6) proper grounding of the metallic housing of the transducer array, preamplifiers, and DAQs is important to reduce noise. The motors are often well-shielded to eliminate electromagnetic interference.

The high imaging speed and deep penetration is the key advantage of PACT over PAM. Nevertheless, deeper penetration is necessary for many clinical applications, including human brain or trunk imaging. By simply replacing the laser with a pulsed microwave source and applying proper shielding of the transducers and electronics, microwave-induced TAT images can be generated using the same reconstruction algorithm. Different from visible light absorption in which heat is generated by non-radiative relaxation of excited electrons, microwaves generate heat through the electrical conductivity of tissues. Molecular relaxation and ionic conduction dominate this response at microwave frequencies, which generally relate to water and salt content. Therefore, the difference in dielectric properties of biological tissues can be revealed by TAT.

Dissertation outline

Both PACT and PAM have the potential for clinical applications. Most of the projects in this thesis were accomplished to advance PAI for small animal imaging, and to then transfer the improved technology for human applications. The essential improvements in PACT for bedside imaging are to provide greater depth and multiple contrasts. In PAM, one key objective is to minimize the system for handheld operation. Prior to the work in this thesis, PACT was limited to the imaging depth of a few millimeters *in vivo* and was mainly used to image the mouse brain cortex. First, internal illumination was developed using an optical fiber in the oral cavity to demonstrate PACT of the deep rat brain *in vivo*, and whole rat brain imaging was then implemented using a stronger laser and faster system (Chapter II). The experience gained from small animal brain PACT was further transferred to human breast imaging. In this new system, high-resolution, high-speed, and deep-penetration PACT was first demonstrated for breast cancer patients. This study was further

extended to assess the effectiveness of neoadjuvant chemotherapy in breast cancer patients (ongoing project) (Chapter III). To advance the technology for human brain imaging, another PACT system was developed with improved performance that provided isotropic spatial resolution in 3D space. The system has been validated by imaging healthy human subjects and will be moved to the Children’s Hospital of Los Angeles for neonatal brain imaging (Chapter IV). To provide dielectric imaging contrast and further extend the imaging depth, TAT of a rat *in vivo* and transcranial imaging of a phantom enclosed by a human skull were demonstrated (Chapter V). Based on the dynamics of PA signals at different oxygenation states, oxygenation of hemoglobin and myoglobin were revealed in mice backbone muscles, thus providing multiple optical contrasts (Chapter VI). In addition to PACT, OR-PAM of mouse cortical microhemodynamics was explored (Chapter VII), where the system was minimized from a benchtop system to a handheld probe for human skin imaging (Chapter VIII). The dissertation outline is summarized in Fig. 1.

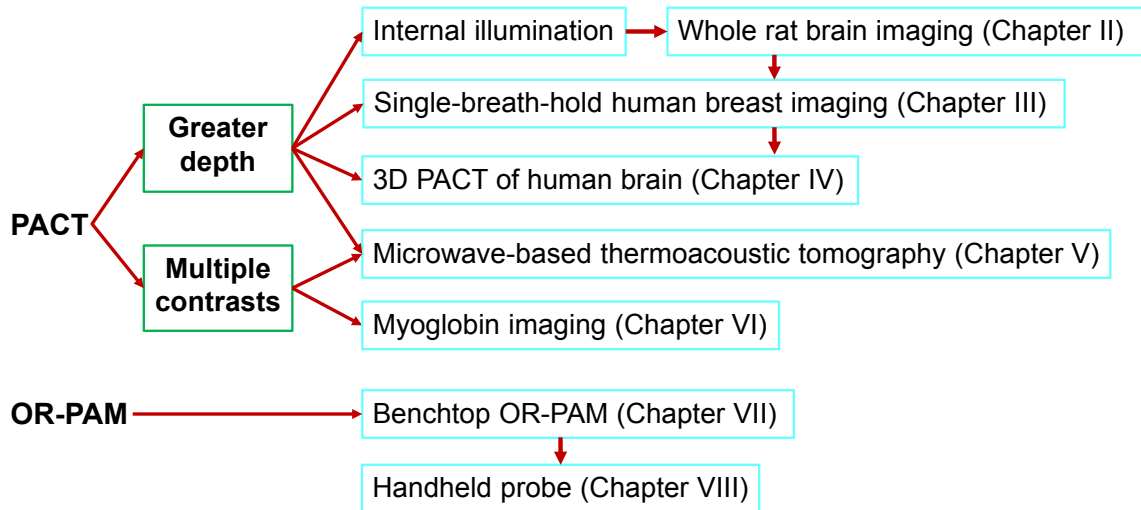


Figure 1. Dissertation outline.

All animal experimental procedures in this dissertation were carried out in conformity with laboratory animal protocols approved by the Animal Studies Committee at Washington University in St. Louis and the Institutional Animal Care and Use Committee at California Institute of Technology. All the human experiments followed protocols approved by the Institutional Review Board (IRB) and Protocol Review and Monitoring Committee (PRMC) of Washington University in St. Louis, as well and the IRB at California Institute of Technology and City of Hope National Medical Center.

Chapter II

PACT OF RAT BRAIN

The evolution of this research began from small animal imaging. Existing PACT systems were used with improved setups to demonstrate deep imaging depth in the rat brain. Knowledge gained from these trials was then transferred to building human-scale breast and brain PACT systems.

Introduction and Motivation

The brain has been likened to a great stretch of unknown territory consisting of a number of unexplored continents. Small animal brain imaging plays an important role in biomedical research. Currently, two major animal brain imaging modalities are multiphoton microscopy and MRI. However, these imaging techniques have their own limitations. Multiphoton microscopy has a depth limit around 1 mm [12]. Functional MRI (fMRI) of small animals requires a costly high magnetic field to achieve sufficient temporal and spatial resolutions [13].

As a nonionizing imaging modality, PACT is gaining increasing interest in neuroimaging. Its hybrid nature allows PACT to image optical absorption with ultrasonically defined spatial resolution beyond the diffraction limit, which limits the penetration capability of ballistic optical imaging such as two-photon microscopy. Prior to this work, multiple PA brain imaging studies have been reported [14-19]. However, due to the limited light penetration depth, most studies focused on cortical imaging [14, 16, 18, 19]. By then, only two studies on deep brain PA imaging have been reported. One used

external illumination through the scalp of a dead mouse [15]. While some deep structures can be identified, the imaging depth was limited to intermediate layers of the brain. The dead brain also limited its usefulness in functional neural studies. The other study used an optical fiber bundle illuminating the circumference of a mouse head to acquire coronal-view images [17]. However, their presented image still shows strong cortex signals and the internal brain structures can barely be identified. The limited-view half-ring detection also prevents accurate reconstruction of the cross-sectional image.

Oral-cavity illuminated PACT of Rat Brain

To deliver light deep into the brain, either strong lasers with low-attenuation wavelengths or internal illumination using lower-power light sources can be used. At the time of this work, strong lasers were not available to us, so we resorted to internal illumination. By inserting a multimode optical fiber with a side-illumination tip into the oral cavity of a rat, we delivered more light to the base of the brain than with conventional external illumination through the scalp. The PA signals were collected by a full-ring-array PACT system [18]. The full-ring ultrasonic transducer array provided faster imaging speed than a single-element ultrasonic transducer scanner [15] and more accurate image reconstruction than a fixed half-ring transducer array [17].

Figure 2a shows a schematic of the oral-cavity illuminated PACT (OI-PACT) system. A tunable Ti-Sapphire laser pumped by a Q-switched Nd:YAG laser emitted pulsed light with a 780-nm wavelength, 12-ns pulse width, and 10-Hz repetition rate. The laser beam was first condensed by two convex lenses. The condensed beam, with a full-width at half-maximum of ~ 2 mm, was then coupled into a multimode optical fiber (2.8-mm core

diameter, SGS-3.0, Fiber Optic Store) with a coupling efficiency of approximately 35%. The other end of the fiber was inserted into the rat's mouth as shown in Fig. 2b. A 45-deg right-angle prism was attached to the fiber tip and fixed in an air chamber enclosed by transparent cladding and translucent adhesive. To quantify the illumination uniformity, we measured the light intensity around the fiber tip using a power meter with a pinhole in front. The light intensities at 45 deg and 90 deg were, respectively, $\sim 56\%$ and $\sim 15\%$ of the intensity at 0 deg (Fig. 2b). The maximum light intensity at the palate surface was approximately 20 mJ/cm^2 , which was below the American National Standards Institute (ANSI) limit (29 mJ/cm^2) at the chosen wavelength [20]. The total energy at the output end of the fiber was $\sim 10 \text{ mJ}$.

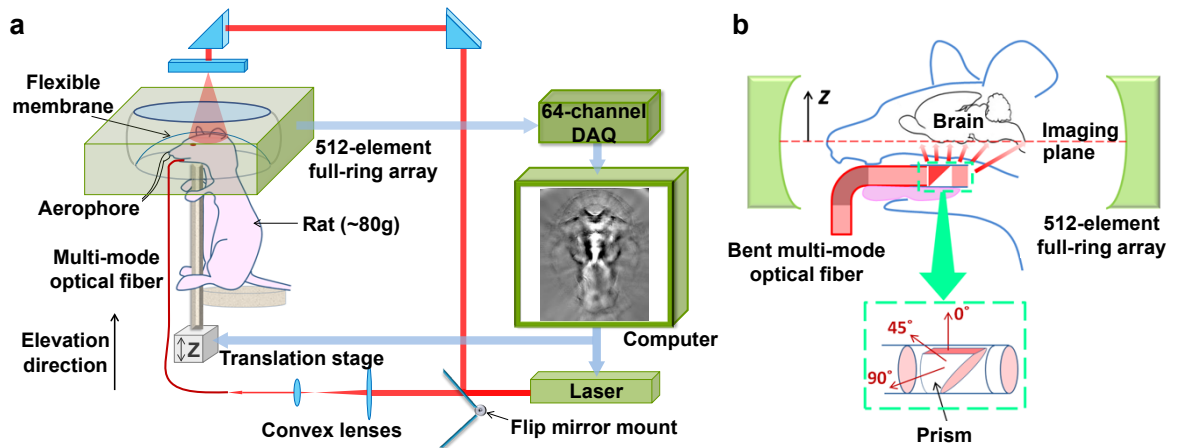


Figure 2. Experimental setup of the oral-cavity illuminated PA computed tomography (OI-PACT) system: (a) Schematic of the OI-PACT system. (b) Detailed view of the optical fiber tip in the rat's mouth. The origin of the z-axis was aligned with the plane 3 mm above the fiber tip.

As shown in Fig. 2a, the rat was mounted in an upright position and was secured to a holder.

We then mounted the holder on a translation stage for elevational scans. The rat was placed

underneath the water tank with its scalp coupled to the flexible membrane through ultrasonic gel to be imaged through the membrane.

The PACT system utilized a 5-MHz (80% bandwidth) transducer array formed into a circular aperture with a 50-mm diameter. Each element was shaped into an arc in elevation to produce an acoustic focal length of 19 mm. The combined foci of all elements generated a central imaging region of 20-mm diameter and 1-mm thickness. Within the central imaging region, the system provided relatively uniform 0.10-mm radial (axial) resolution and <0.25-mm tangential (transverse) resolution [18]. The center cross section of the ultrasonic transducer array determined the imaging plane, which was 3 mm above the fiber tip (Fig. 1b) when we imaged the brain base. The origin of the z-axis was aligned with the plane of the brain base. For the particular rat shown here, the elevational distance from the scalp to the brain base was around 13 mm.

The data acquisition was triggered by the laser's Q-switch signal. After every other laser shot, the 8:1 multiplexer on the receiver boards forwarded the data from the transducer elements to the 64-channel acquisition board. With pure endogenous hemoglobin contrast and 10 times averaging, each PA image was acquired over 16 s. In order to reduce artifacts caused by the acoustic heterogeneities in the rat's head, we used the simplified half-time image reconstruction algorithm [21], which backprojected only the first half of the received data.

To investigate the advantages of internal illumination in deep brain imaging, after each measurement with fiber illumination, we also acquired corresponding control images with external illumination. Figure 3 shows a series of *in vivo* images acquired over an

elevational distance of 5 mm in the brain's bottom region, with images acquired by internal illumination above (Figs. 3a–3c) and corresponding images obtained by external illumination below (Figs. 3d–3f). Clearly, for deep brain imaging, using the same PACT data collection system and image reconstruction algorithm, internal illumination provides much clearer images than external illumination, which barely showed any recognizable structures. Figure 3g shows an *in vivo* PA image of the rat brain base ($z = 0$ mm, ventral aspect). In the image, the left and right cerebral hemispheres, brain stem, hypothalamus, and anterior cerebral artery underneath the optic chiasma are clearly visible. In addition to the brain structures, the interface between the zygoma and the muscle tissue can also be seen. After the imaging experiment, we euthanized the rat in a CO₂ chamber and then dissected its brain to photograph the anatomy in ventral view (Fig. 3h). The PA image and photograph agree with each other despite the fact that the release from skull confinement slightly changed the shape of the cerebral hemispheres.

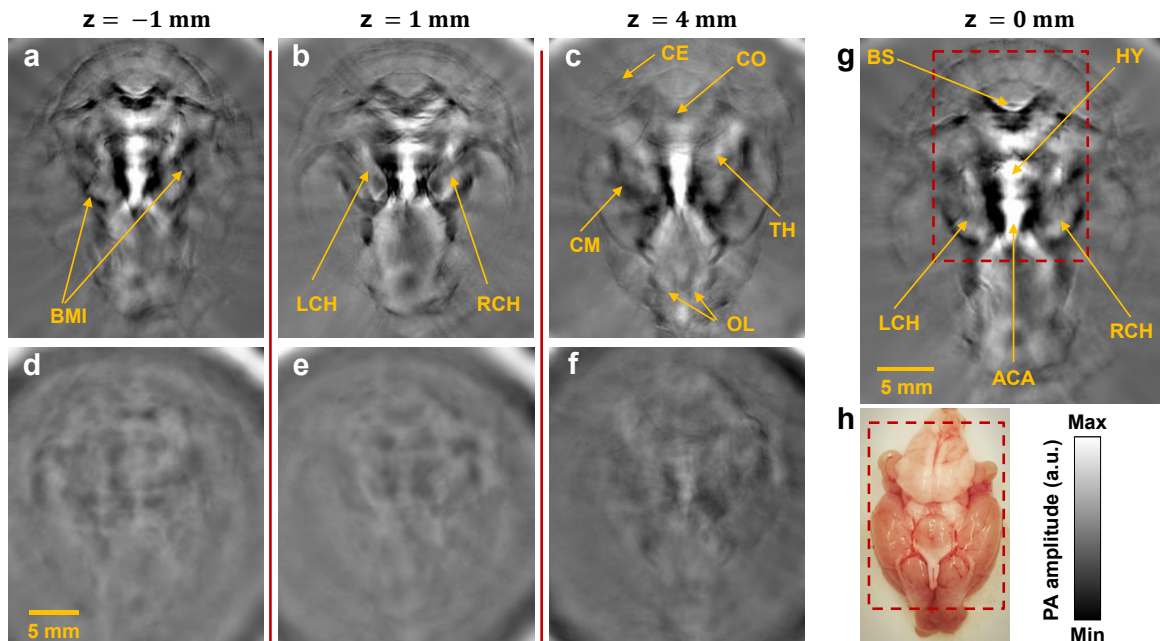


Figure 3. A series of images acquired at $z = -1$ mm (a), $z = 1$ mm (b), and $z = 4$ mm (c), with control images at the same layers (d)–(f) acquired by external illumination through the top skull. (g) *In vivo* PA image of the rat brain base ($z = 0$ mm) acquired by OI-PACT. (h) Corresponding photograph of the anatomy of the same rat brain. ACA, anterior cerebral artery; BS, brain stem; BMI, bone-muscle interface; CE, cerebellum; CM, cerebral medulla; CO, colliculus; HY, hypothalamus; LCH, left cerebral hemisphere; OL, olfactory lobes; RCH, right cerebral hemisphere; and TH, thalamus.

Rat Whole Brain Functional Imaging by Single-Impulse Panoramic PACT

Two years afterwards, we built a single-impulse panoramic PACT (SIP-PACT) system which is coupled with a stronger Nd:YAG laser. The PACT system is equipped with a cylindrically-focused ring array that is similar to the previous version, but with one-to-one mapped preamplification and analogue-to-digital sampling (no multiplexer) so that it can form a 2D image from a single laser shot. Accordingly, SIP-PACT realizes high spatiotemporal resolution (125 μm in-plane resolution, 50 μs per frame data acquisition and 50 Hz frame rate) without noticeable motion artifacts [22].

Equipped with the strong laser at 1064 nm, we imaged the entire rat brain on the coronal plane. As shown in Fig. 4a, the rat head was mounted vertically and the light was delivered obliquely to the rat cortex. A cranial window was opened to maximize the acoustic transmission. Taking advantage of the low scattering of 1064 nm light, the full-view acoustic coverage and high detection sensitivity of SIP-PACT, coronal views of the whole rat brain (11 mm in depth) was produced with detailed vasculature (Fig. 4b).

The brain serves as the center of the nervous system, dynamically coordinating responses through the functional network. We utilized PACT to detect the functional connectivity by globally monitoring the brain hemodynamics with appropriate spatiotemporal resolution

and penetration. We measured and compared the spontaneous hemodynamic responses between contralateral regions of the rat brain. In the seed-based functional connectivity study, we picked a seed in the image and computed the correlation coefficients between all pixels in the region of interest and the seed (Fig. 4c). Excitingly, we identified the left-right correlation between the deep thalamus regions (9.7 mm in depth, Fig. 4c, bottom right), which, to the best of our knowledge, has not been demonstrated at this spatial resolution.

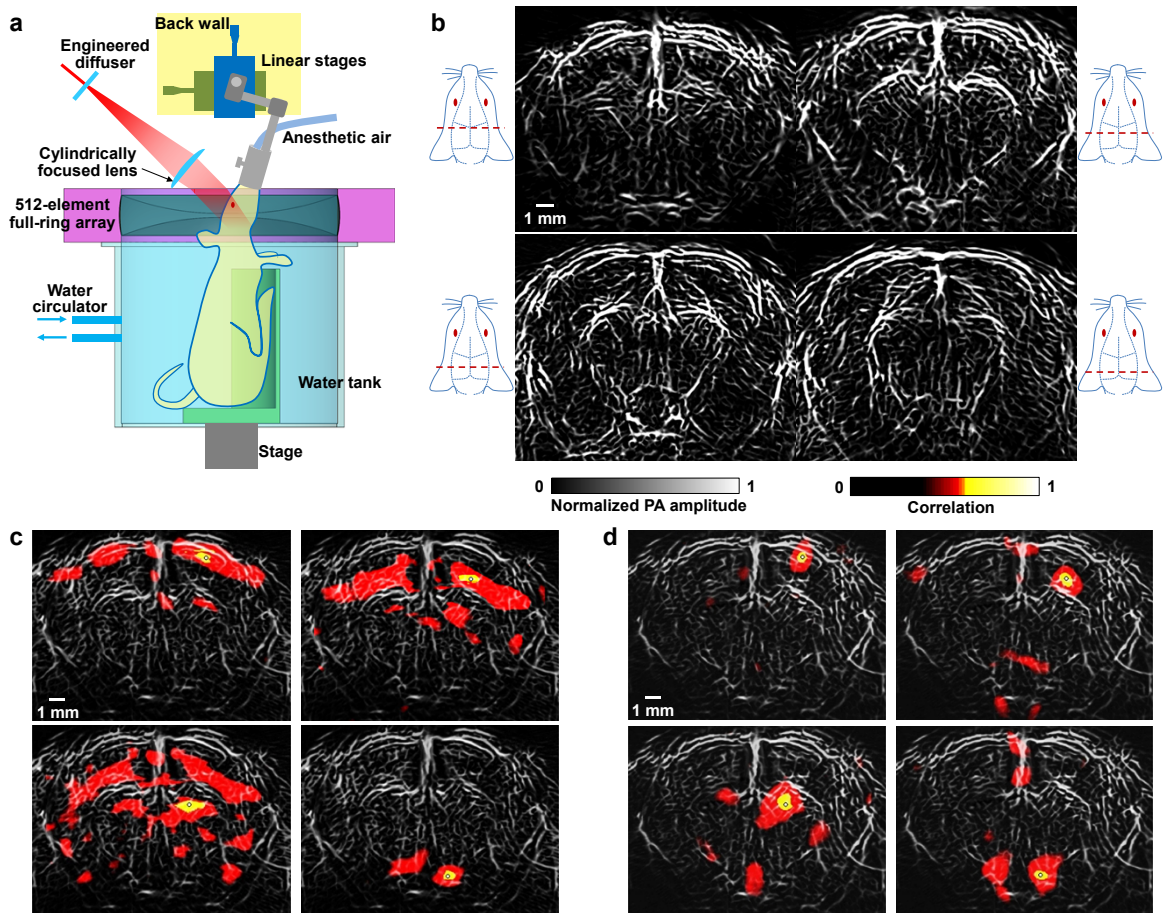


Figure 4. (a) Setup of the rat brain imaging. The rat head was mounted vertically during imaging and 1064-nm light was obliquely delivered to the rat cortex. (b) Rat whole-brain vasculature in different coronal planes (From ~bregma -1 mm to -4 mm). (c) Seed-based functional connectivity analyses of different functional regions on both sides of the brain

before the stroke surgery. (d) Seed-based functional connectivity analyses the brain after the stroke surgery.

We further performed a stroke ligation surgery at a neck artery of the same rat and assessed the functional connectivity between the two hemispheres. Because of the ischemia in the left brain hemisphere, most correlations disappeared (Fig. 4d). Interestingly, the left–right correlation between the deep thalamus regions still existed (Fig. 4d, bottom right). The functional connectivity observation demonstrates the potential of PACT as a high-resolution imaging tool for studying deep brain functions in rats, which was previously difficult to accomplish using optical contrast, and therefore underexplored.

Summary and Outlook

By utilizing a fiber-transmitted internal illumination and full-view-array PACT system, we first demonstrated a method for deep rat brain imaging when laser energy is not adequate for external illumination. With the improvements of high-energy lasers and DAQ systems, we further made fast and deep PACT available for small animal imaging. Using the new PACT system with strong 1064-nm light, the entire rat brain was imaged, realizing whole brain functional imaging by showing the functional connectivity of different functional regions before and after stroke surgery. More efforts are necessary to improve the imaging sensitivity, spatiotemporal resolution, and contrast agents to assess single neuron action potentials in the whole brain.

Chapter III

PACT OF HUMAN BREAST CANCER

The experience gained from small animal brain PACT inspired the design and construction of an advanced PACT system for human breast imaging, which requires deeper penetration and higher reliability. We have developed a single-breath-hold photoacoustic computed tomography (SBH-PACT) system to reveal detailed angiographic structures in human breasts.

Introduction and Motivation

About 1 in 8 (12%) women in the U.S. will develop invasive breast cancer during their lifetime [23]. Multiple large prospective clinical trials have demonstrated the importance of early detection in improving breast cancer survival [24-26]. While mammography is currently the gold standard used for breast cancer screening, it utilizes ionizing radiation and has lower sensitivity in women with dense breasts [27, 28]. Ultrasonography has been used as an adjunct to mammography, but suffers from speckle artifacts and low specificity [29, 30]. MRI poses a large financial burden and requires the use of intravenous contrast agents that can cause allergy [31], kidney damage [32], and permanent deposition in the central nervous system [33]. Diffuse optical tomography has been investigated to provide functional optical contrast. However, the spatial resolution of the current prototypes limits their clinical use [34, 35]. Overall, each modality has notable advantages and limitations. PACT is a promising complementary modality that overcomes many of these limitations.

In the near infrared (NIR) region, the $1/e$ attenuation coefficient ($1.0\text{--}1.3\text{ cm}^{-1}$) [36] for light in an average breast is less than twice that for mammographic X-rays ($0.5\text{--}0.8\text{ cm}^{-1}$) [37]. However, the optical absorption contrast of soft tissue is much higher than X-ray contrast [38]. For breast imaging, PACT can exploit these advantages to the fullest, offering high spatial and temporal resolutions with sufficiently deep nonionizing optical penetration [7, 39]. As the principal optical absorber in the NIR region, hemoglobin provides an endogenous contrast for imaging of blood vessels. A high density of blood vessels should correlate with angiogenesis [40-42], which plays an important role in tumor growth and metastasis [43].

Several breast PACT systems have been developed, employing different light illumination and detection schemes [44-53]. These systems have advanced PACT toward clinical application, but ongoing limitations remain to be addressed. Here, we consider five main factors: (1) sufficient penetration depth to accommodate most breast sizes and skin colors, (2) high spatial resolution to reveal detailed angiographic structures, (3) high temporal resolution to minimize motion artifacts and enable dynamic or functional studies, (4) minimal limited-view artifacts, and (5) sufficient noise-equivalent sensitivity and contrast-to-noise ratio to detect breast masses.

Specifically, the current systems' limitations mainly arise from their long scanning times [44-46] and/or limited-view apertures (i.e., missing data or a $<2\pi$ steradian solid angle) [46-52]. Toi et al. recently reported a photoacoustic imaging system with a hemispherical detector array [44], which was modified from a previous design [45]. Although the design for acoustic detection is slightly different, both used a sparse hemispherical detector array and scanned in a spiral pattern on a plane. The dense sampling, and the nearly isotropic 3D

spatial resolutions produced elegant vascular images, but tumor detection was limited by respiratory motion artifacts resulting from the long scanning time (~4 min). Although co-registration partially mitigated the breathing motion distortion, the non-rigidity of the breast compromised the effectiveness. While larger vessels were coregistered, small tumor vessels, which often occur in small clusters, could be challenging to be imaged with partial data and even more difficult to be coregistered. Other groups have used planar transducer arrays [47-50] and arc-shaped arrays [51] for breast imaging. However, the limited views of these systems decreased their overall performances [54, 55]. Consequently, most blood vessels were not well visualized in their images. The same problem occurred with linear transducer arrays, either fixed in position [52] or scanned [46]. A ring-shaped array of 32 elements was developed at presumably relatively low system cost [53]. However, the low number of elements severely limited the field of view due to the spatial Nyquist sampling criterion, resulting in degradation of image quality [22].

The experience gained from small animal brain PACT has been transferred to a significant advancement in breast PACT technology that overcomes all of the aforementioned limitations. Our breast imaging modality—SBH-PACT—is the first PACT system that meets the aforementioned five conditions: (1, 2) Combining 1064-nm light illumination and a 2.25-MHz unfocused ultrasonic transducer array, SBH-PACT achieved up to 4 cm *in vivo* imaging depth and a 255 μm in-plane resolution (approximately four times finer than that of contrast-enhanced MRI [56]). (3) Equipped with one-to-one mapped signal amplification and DAQ circuits, SBH-PACT can obtain an entire 2D cross-sectional breast image with a single laser pulse, or obtain a volumetric 3D image of the entire breast by fast elevational scanning within a single breath-hold (~15 s). The 10 Hz 2D frame rate,

currently limited by the laser repetition rate, enables SBH-PACT to observe biological dynamics in a cross-section associated with respiration and heartbeats without motion artifacts. (4) A full-ring 512-element ultrasonic transducer array enables SBH-PACT for full-view fidelity in 2D imaging planes and delivers high image quality. (5) Capitalizing on the optimized illumination method and signal amplification, SBH-PACT achieves sufficient noise-equivalent sensitivity to clearly reveal detailed angiographic structures both inside and outside breast tumors without the use of exogenous contrast agent.

System Construction and Characteristics

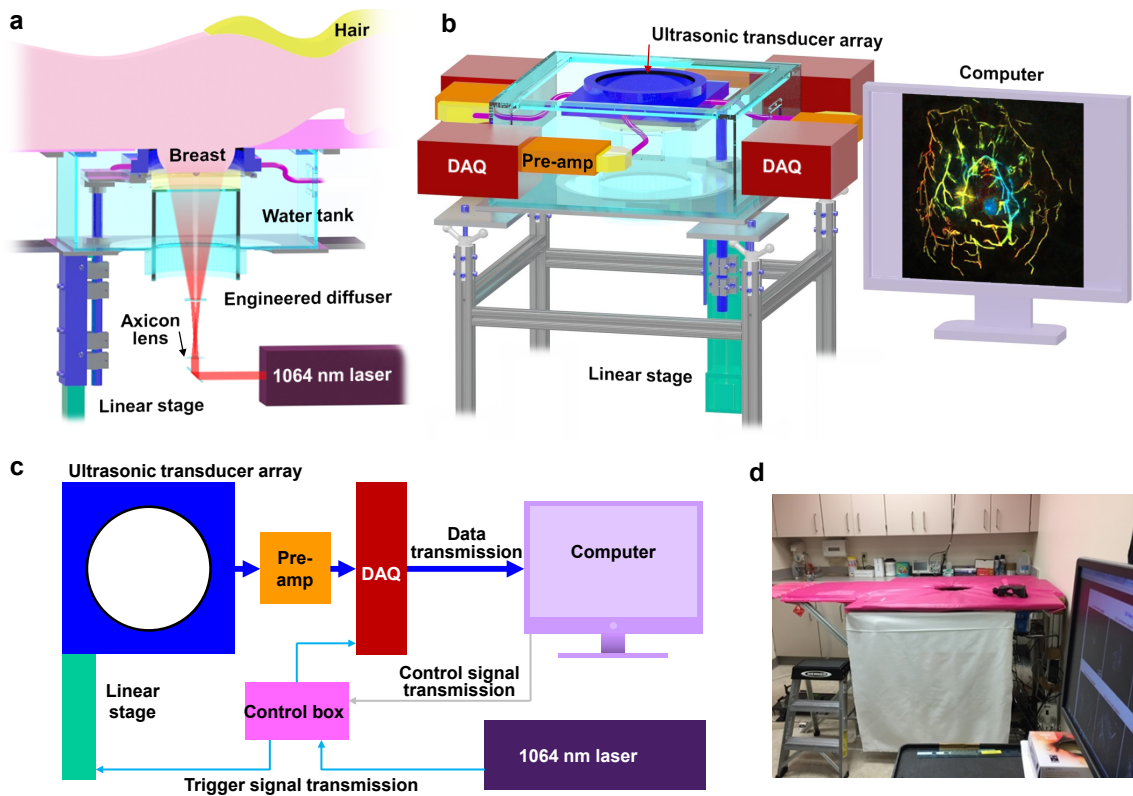


Figure 5. Representations of the SBH-PACT system. (a) Perspective cut-away view of the system with data acquisition components removed. (b) Perspective view of the system with patient bed and optical components removed. (c) Signal flow diagram for the system. (d) Photograph of the system. DAQ, data acquisition system; Pre-amp, pre-amplifier circuits.

The SBH-PACT system is placed underneath a patient bed with minimal separation from the top surface of the bed to the top scanning position of the ultrasonic transducer array (Fig. 5). With the patient lying prone on the bed, the breast to be imaged is slightly compressed against the chest wall by a soft agar pillow. Compared to craniocaudal or mediolateral breast compression, compression against the chest wall not only avoids pain, but also gives the least thickness breast tissue for light to penetrate from the nipple to the chest wall. The laser illuminates the breast from beneath the patient’s breast, and the ultrasonic transducer array detects photoacoustic waves circumferentially around the breast. The light beam is converted into a donut shape via an axicon lens followed by an engineered diffuser. Compared to a Gaussian beam, the donut beam provides more uniform illumination inside the breast (Fig. 6) and also deposits less energy on the nipple and areola, which have a higher concentration of pigment. We take advantage of the low optical attenuation of 1064 nm light to achieve sufficient optical penetration in breast tissue [57].

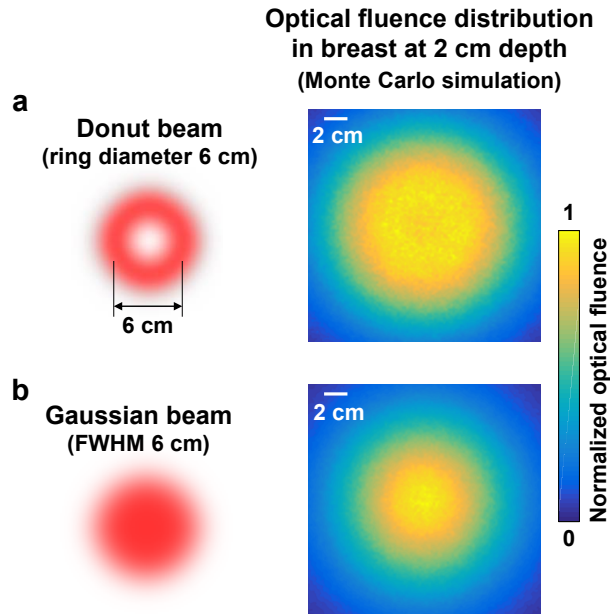


Figure 6. Simulation of the optical fluence in breast tissue at 2 cm depth, produced by different illumination schemes. (a) Distribution of the optical fluence in breast tissue when

the illumination beam is donut-shaped. After removing the engineered diffuser, the ring diameter is approximately 6 cm. (b) Distribution of the optical fluence in breast tissue at the same depth when the illumination beam is Gaussian-shaped. The FWHM of the beam is approximately 6 cm. To mimic a breast compressed against the chest wall, we built a cylindrical breast model with a height of 4 cm and a diameter of 15 cm. In this numerical model, the absorption coefficient (0.05 cm^{-1}) and the reduced scattering coefficient (7 cm^{-1}) inside the breast were selected for a 1064 nm wavelength [58].

To provide 2D panoramic in-plane acoustic detection, we employ a full-ring ultrasonic transducer array with 512 elements. Four sets of 128-channel data acquisition systems provide simultaneous one-to-one mapped associations with the 512-element transducer array. Therefore, we acquire photoacoustic signals from a cross section within $100 \mu\text{s}$ without multiplexing after each laser pulse excitation. The ultrasonic transducer elements have a central frequency of 2.25 MHz and a one-way bandwidth of more than 95% (Fig. 7a, b), providing an experimentally quantified in-plane resolution of $255 \mu\text{m}$ (Fig. 7c, d). The height of each transducer element yields a moderate divergence angle in the elevational direction ($\sim 9.0^\circ$ FWHM), yielding a flared diffraction pattern (Fig. 8a). This pattern enables both 2D imaging of a breast cross section per laser pulse and 3D imaging of the whole breast by scanning elevationally. Our 3D back-projection algorithm can reconstruct a volumetric image with an elevational resolution of 5.6 mm, which is ~ 3 times finer than that given by the 2D reconstruction algorithm (Fig. 8b, c).

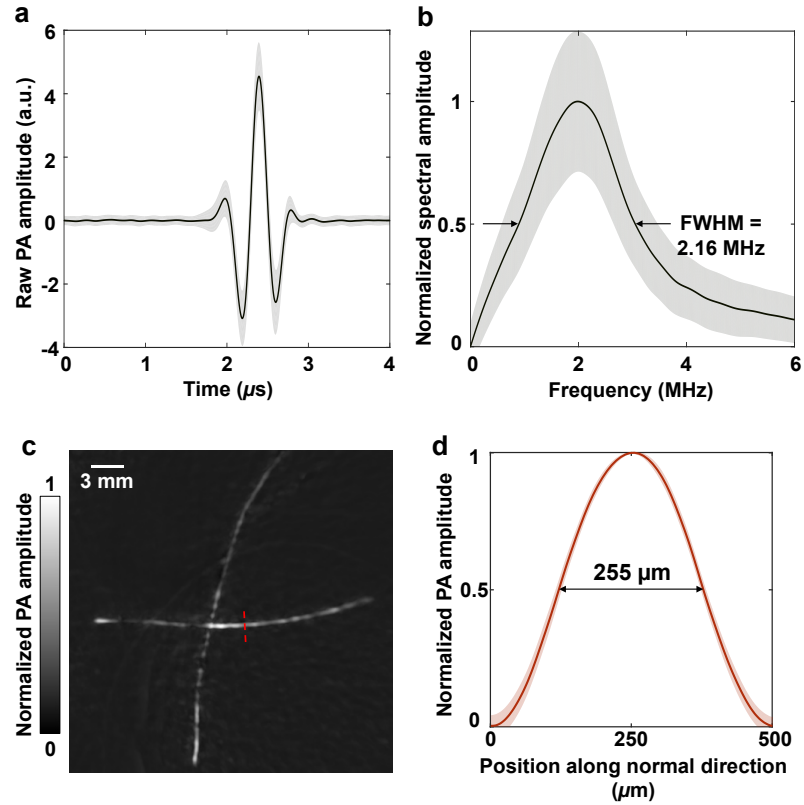


Figure 7. (a) The raw radio frequency signal from each ultrasonic transducer element corresponding to a point PA source at the center of the full-ring array. The black solid line represents the mean value of all transducer elements' responses, and the gray region represents the standard deviation (STD) across the elements. (b) Fourier transform amplitude of each RF signal in (a), showing that the bandwidth of the transducer array is about 2.16 MHz. The point source was created by fixing a carbon particle (20–50 μm) in an agar phantom. The particle was small enough to be regarded as a spatial point source for the SBH-PACT system. (c) A maximum amplitude projection (MAP) image of two crossed tungsten wires, each with a nominal diameter of 13 μm . (d) The PA amplitude distribution along the red dashed line in (c). The in-plane resolution, defined as the FWHM of the amplitude distribution, is 255 μm .

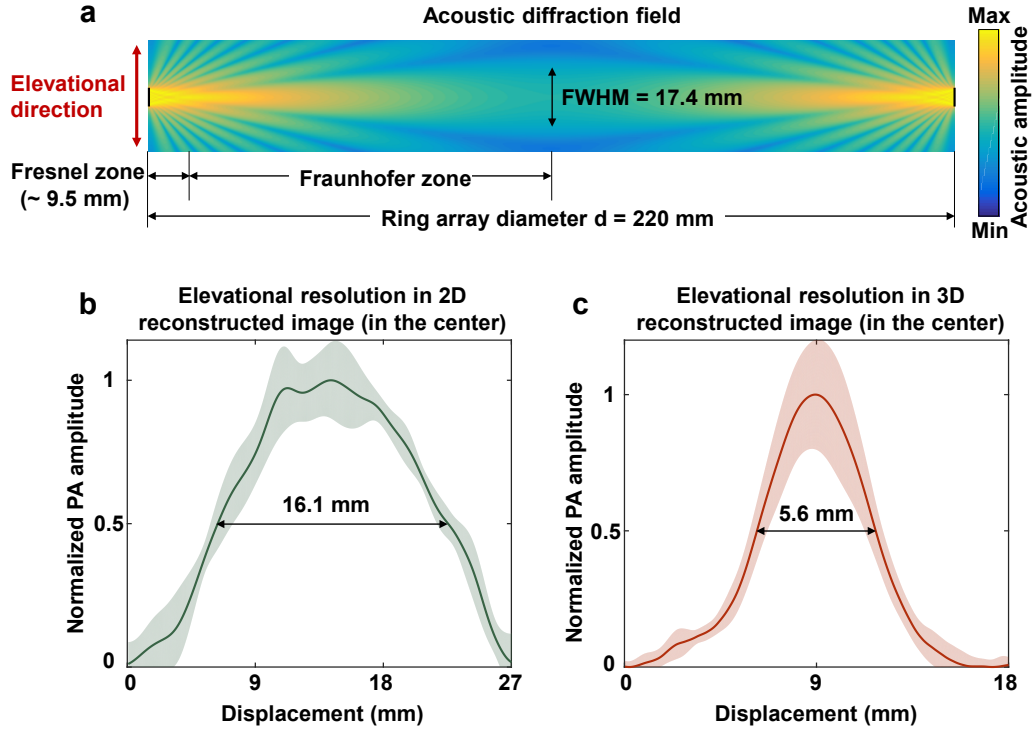


Figure 8. Quantification of elevational resolution. (a) Simulated acoustic diffraction field in the elevational direction. (b) Line profile in the elevational direction of a carbon particle (20–50 μm , placed at the ring center) reconstructed by 2D back-projection. (c) Line profile in the elevational direction of the same carbon particle reconstructed by 3D back-projection.

SBH-PACT of Healthy Breast Anatomy and Dynamics

Before imaging breast cancer patients, the performance of SBH-PACT was assessed by imaging a 27-year-old healthy female volunteer. By scanning the transducer array elevationally through her right breast, within one breath hold (~ 15 s), we revealed the angiographic anatomy from the nipple to the chest wall (Fig. 9a). The color-encoded depth-resolved image clearly revealed the detailed angiographic structures of the entire breast (Fig. 9b), visualizing the vasculature down to an apparent vascular diameter of 258 μm (Fig. 9c). We further investigated the relationship between parent and daughter vessels at vascular bifurcations, which is expressed by the junction exponent (X_B) [59]. We selected

a vessel tree in the breast and marked five branch levels with distinct colors (Fig. 9d). At five vascular bifurcations (B1–B5), we calculated the junction exponents as well as the ratios between the cube of the diameter of the parent vessel and the sum of the cubes of the diameters of the daughter vessels (Fig. 9d).

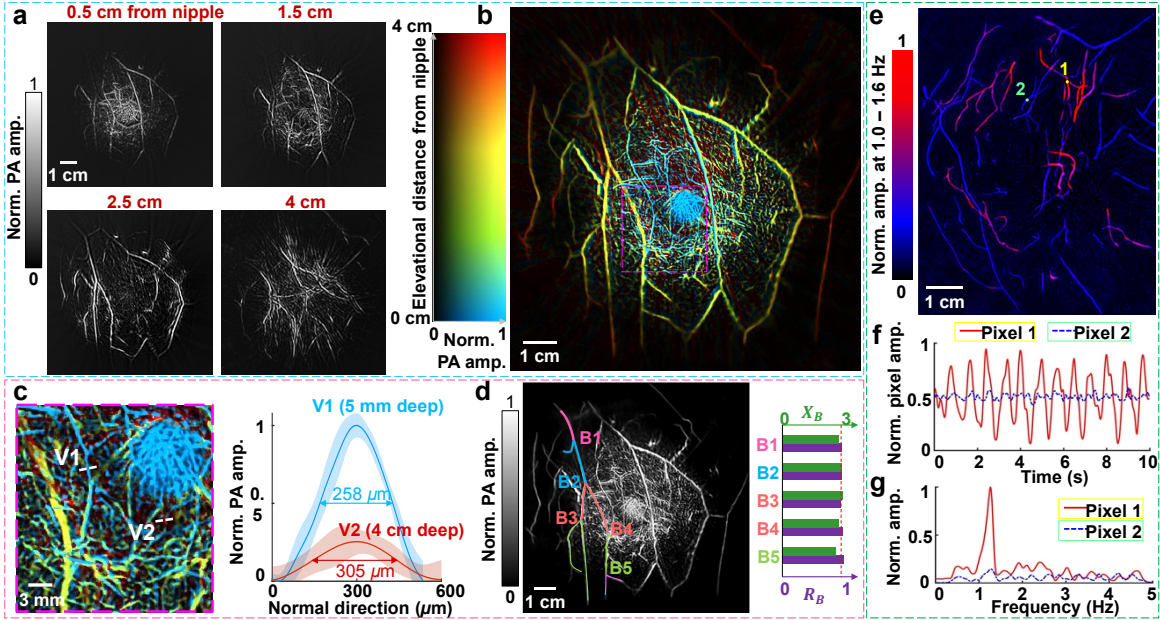


Figure 9. SBH-PACT of healthy breasts. (a) Vasculature in the right breast of a 27-year-old healthy female volunteer. Images at four depths are shown in increasing depth order from the nipple to the chest wall. (b) The same breast image with color-encoded depths. (c) A close-up view of the region outlined by the magenta dashed box in (b), with selected thin vessels and their line spread plots. (d) A selected vessel tree with five vessel bifurcations, labeled from B1 to B5. At each bifurcation, the diameter relationships between the parent vessel (D_{parent}) and daughter vessels ($D_{daughter}$) are presented on the right. X_B is the junction exponent, and R_B is defined as $R_B = D_{parent}^3 / (D_{daughter_a}^3 + D_{daughter_b}^3)$. (e) Heartbeat-encoded arterial network mapping of a breast cross-sectional image (red = artery, blue = vein). (f) Amplitude fluctuation in the time domain of the two pixels highlighted by yellow and green dots in e. The pixel value in the artery shows changes associated with arterial pulse propagation. (g) Fourier domain of the pixel value

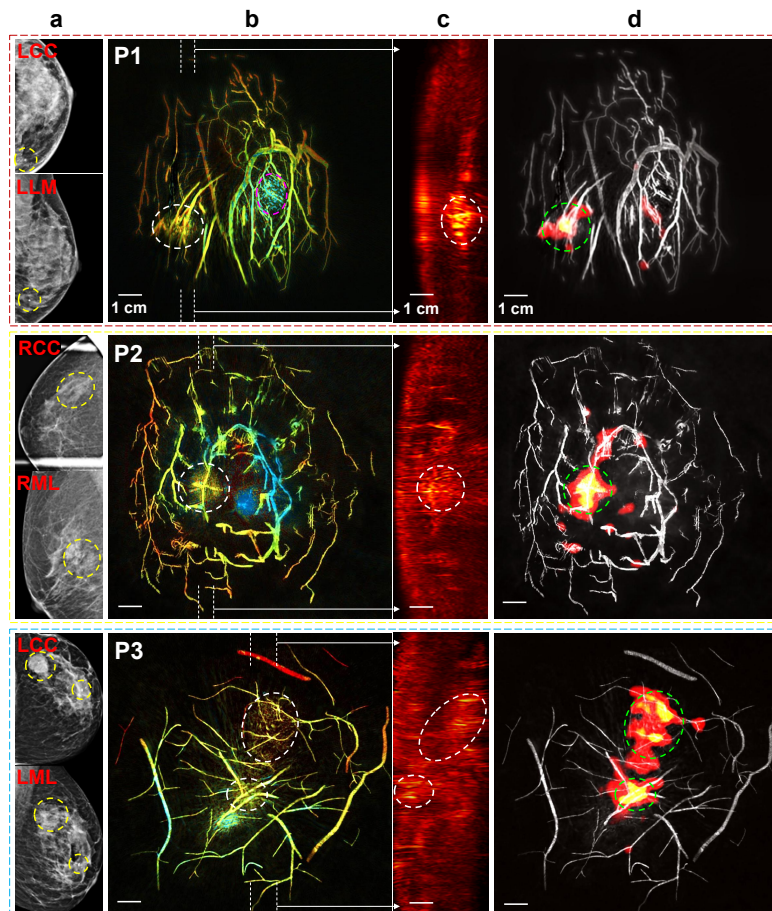
fluctuations in f . The oscillation of the arterial pixel value shows the heartbeat frequency at ~ 1.2 Hz.

During a breath hold within 10 s, we imaged a cross section of the contralateral healthy breast in one of the breast cancer patients. Working in 2D mode at 10 Hz frame rate, SBH-PACT continuously monitored arterial pulsatile deformation inside the breast by fixing the transducer array at a specific elevational position [60]. PA signals were analyzed pixel-wise in the frequency domain to identify arteries and veins according to the heartbeat frequency (Fig. 9e). For illustration, we selected a pixel from one artery and one vein (highlighted by round dots 1 and 2 respectively in Fig. 9e) and plotted their pixel value fluctuation (Fig. 9f). The periodic oscillation of the pixel values in the artery indicates that the changes were the result of pulse waves propagating through the arterial network. The oscillation frequency further reveals the subject's heart rate of ~ 1.2 Hz (Fig. 9g). Considering that arterial blood has a relatively narrow range of oxygen saturation (sO_2) [61], average PA signals from arteries can potentially be used to calibrate the local optical fluence ($mJ\ cm^{-2}$) deep in the breast, and thus enable accurate quantification of functional parameters (e.g., blood sO_2) with an additional laser wavelength (e.g., 750 nm) [62, 63].

SBH-PACT of Breast Cancer Anatomy, Segmentation, and Elastography

The main purpose to build SBH-PACT was to detect breast tumors with fine details, making this imaging modality potentially useful for multiple applications in breast clinical care. We imaged seven breast cancer patients (Fig. 10), with breast sizes ranging from B cup to DD cup (over 99% of the U.S. population has breast sizes of DD cup or smaller [64]) and skin pigmentations ranging from light to dark. Angiogenesis, which plays a central role in breast cancer development, invasion, and metastasis, is the essential

hallmark by which SBH-PACT differentiates lesions from normal breast tissue [40-42]. Well correlated with the tumor locations shown in mammograms and reported by ultrasound-guided biopsy (Fig. 10a), SBH-PACT showed eight of the nine tumors by observing higher blood vessel densities associated with tumors in the depth-encoded images (Fig. 10b). We further selected tumor-containing slices perpendicular to the chest wall (marked by white dashed lines in Fig. 10b). In these sagittal (side-view) images, the same tumors, where higher PA amplitude is shown, can be seen at corresponding locations (Fig. 10c). In the X-ray mammograms of Patient 1 (P1) and Patient 6 (P6), the lesions in the dense breasts are barely distinguishable. In comparison, SBH-PACT clearly revealed the tumors not readily seen in mammograms, notwithstanding the high radiographical density of the breast.



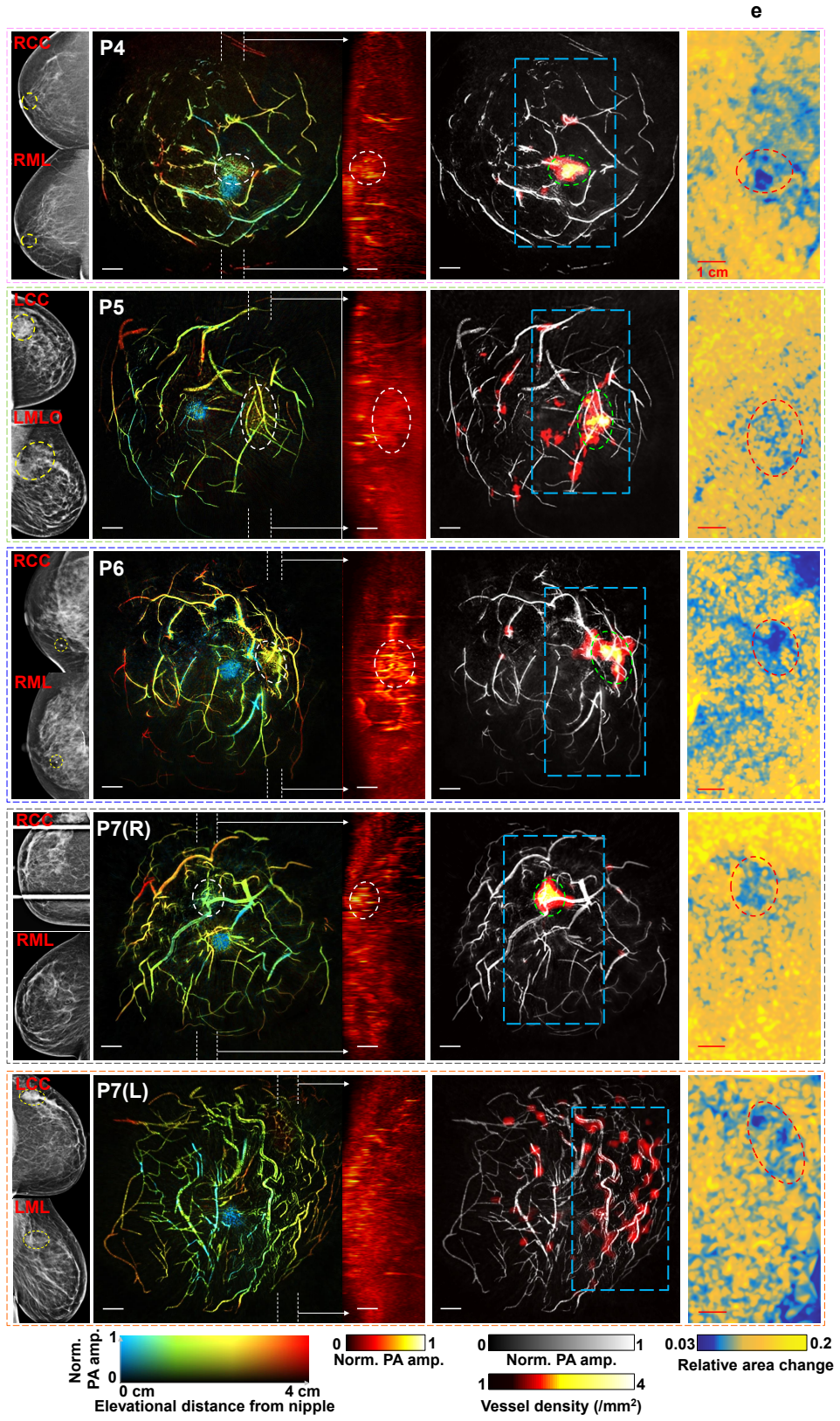


Figure 10. SBH-PACT of cancerous breasts. (a) X-ray mammograms of the affected breasts of seven breast cancer patients. LCC left cranial-caudal, LLM left lateral-medio, LML left mediolateral, LMLO left mediolateral-oblique, RCC right cranial-caudal, RML right medio-lateral. (b) Depth-encoded angiograms of the eight affected breasts acquired by SBH-PACT. Breast tumors are identified by white circles. For illustration, we marked the nipple of the first patient (P1) with a magenta circle. P1—48-year-old female patient with an invasive lobular carcinoma (grade 1/3); P2—70-year-old female patient with a ductal carcinoma in situ (microinvasion grade 3/3); P3—35-year-old female patient with two invasive ductal carcinomas (grade 3/3); P4—71-year-old female patient with an invasive ductal carcinoma (grade 3/3); P5—49-year-old woman with a stromal fibrosis or fibroadenoma; P6—69-year-old female patient with an invasive ductal carcinoma (grade 2/3); P7—44-year-old female patient with a fibroadenoma in the right breast and an invasive ductal carcinoma (grade 2/3) in the left breast. (c) MAP images of thick slices in sagittal planes marked by white dashed lines in (b). (d) Automatic tumor detection on vessel density maps. Tumors are identified by green circles. Background images in gray scale are the MAP of vessels deeper than the nipple. (e) Maps of the relative area change during breathing in the regions outlined by blue dashed boxes in the angiographic images in d. The same tumors are identified by red circles. The elastographic study began with Patient 4, and it revealed all imaged tumors, including the undetected one in (d) (P7(L)).

To assist in translation of the technology to a clinical setting, we developed a tumor segmentation algorithm to distinguish tumors automatically. Presumably due to angiogenesis, tumors appear as regions of denser blood vessels in SBH-PACT images. To segment tumors automatically, we extracted the vessel skeleton and produced a vessel density map of the breast (local vessel number / local area). The regions with the highest vessel density highlight the breast tumors (Fig. 10d).

In addition to direct observation of blood vessel density, SBH-PACT detected the difference in compliance between tumors and surrounding normal breast tissue, providing

an alternate concurrent contrast to detect breast cancer. Before performing elastography on breast cancer patients, we demonstrated this method on breast-mimicking phantoms (Fig. 11). Working in 2D imaging mode, SBH-PACT quantified the relative area changes in a breast cross section when minor deformations were caused by breathing. Because breast tumors are generally less compliant than normal breast tissue [65], the regions with lower relative area changes indicated the breast tumor (Fig. 10e). Unlike ultrasonic elastography, SBH-PACT elastography utilized the contrast of hemoglobin and formed area-quantificational grids between vessels. From only angiographic anatomy detailed by SBH-PACT, the only tumor we missed was located in a marginal region of a D cup breast (P7(L)), where light illumination was insufficient. However, with the addition of SBH-PACT elastography, the missed tumor was identified. Taking advantage of the short time requirement for elastographic measurement (~ 10 s), SBH-PACT can observe both blood vessel density and tissue compliance simultaneously within ~ 30 s. Taken together, these two measurements can improve the sensitivity of breast cancer detection.

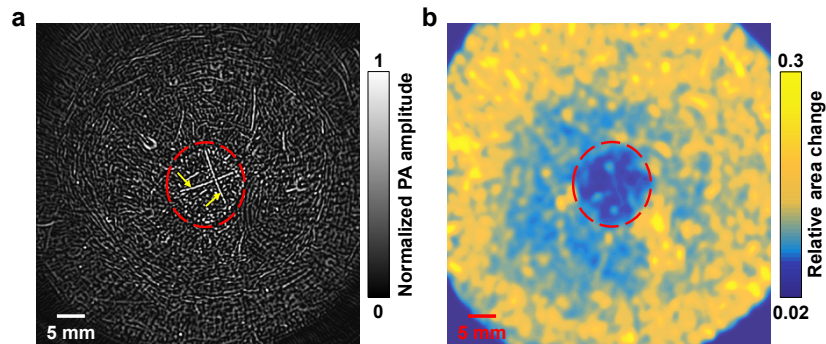


Figure 11. SBH-PACT elastography of a breast mimicking phantom. (a) Cross-sectional image of the phantom acquired by SBH-PACT. Hundreds of chopped human hairs were uniformly distributed in the phantom to mimic small blood vessels. To mark the location for comparison, two crossed tungsten wires (indicated by yellow arrows) were placed inside the ball (enclosed by the red dashed circle), which had a higher agar concentration

to mimic a breast tumor. (b) SBH-PACT elastographic image of the same cross section. Identified by the red dashed circle, the location of the agar ball is revealed correctly.

In this pilot study, SBH-PACT identified eight of the nine biopsy-verified tumors by assessing blood vessel density. Moreover, the initially undetected tumor was subsequently revealed by elastographic SBH-PACT. Pathology reports showed two benign tumors (Patient 5, stromal fibrosis or fibroadenoma; Patient 7, right, fibroadenoma), one ductal carcinoma in situ with a 3/3 nuclear grade (Patient 2), and six invasive carcinomas (all other cases).

Angiogenesis serves as a basis for tumor identification. Considering the diversity among the subjects, we defined high blood vessel densities as values greater than the whole-breast average plus (a) 1.5, (b) 2.0, or (c) 2.5 times the STD, respectively. We calculated and compared the ratios of average vessel density between the high-density region and the normal-density region in each affected and contralateral breast. Receiver operating characteristic (ROC) curves (Fig. 12a) were plotted by varying the threshold of the ratios from 1 to 6. Based on the data from the finite set of subjects, option (b) yielded the largest area (0.90) under the ROC curve. A threshold within (2.26, 2.58) produced a sensitivity (true positive rate) of 88% and a specificity (true negative rate) of 80%. We further performed training and testing studies by obtaining a threshold based on randomly picked six breasts (training set) and then applying the threshold to the remaining seven breasts (testing set). We repeated this procedure ten times and calculated the average sensitivity (87.0%) and specificity (85.9%).

We then demarcated tumors in each breast and computed the average vessel densities inside and outside the tumors (Methods). The average vessel density ratios between the tumors and the surrounding normal breast tissues were 3.4 ± 0.99 (Fig. 12b). In addition, the mean of the average vessel density ratios of the six malignant tumors was 1.4 times higher than that of the two benign ones.

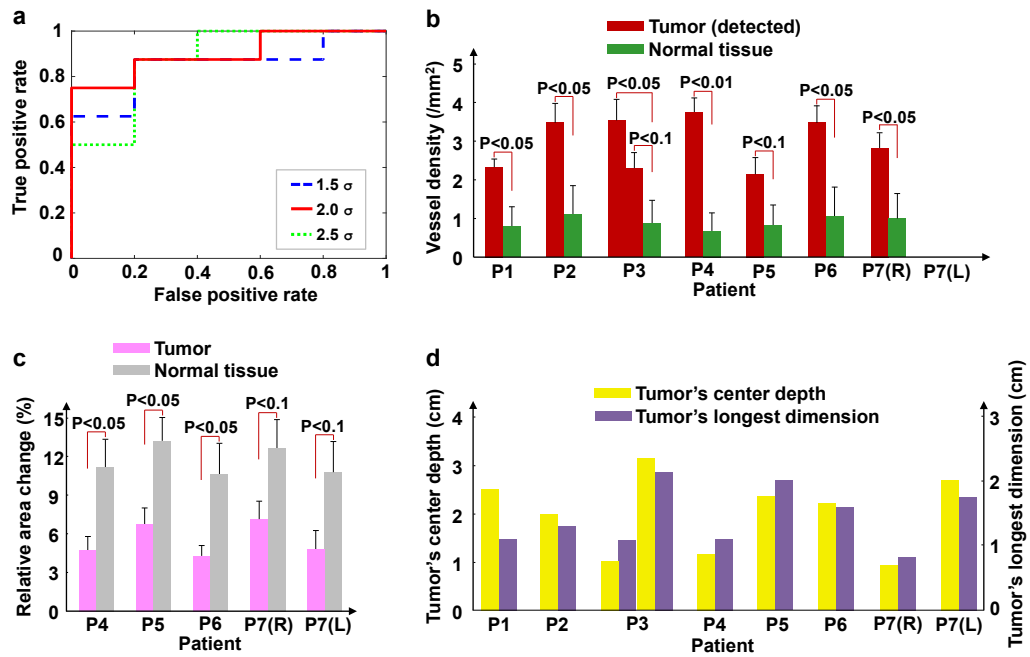


Figure 12. Statistics. (a) The ROC curves of breast tumor detection based on blood vessel density. σ , STD. (b) The average vessel density in each tumor and surrounding normal breast tissue. (c) The relative area change in each tumor and surrounding normal breast tissue caused by breathing. The elastographic study was started with Patient 4. (d) The longest dimension and center depth of each tumor.

Since the elastography study began with Patient 4, SBH-PACT elastography identified all five tumors in the subsequent four patients (Fig. 12c). The average breath-induced area change in tumors was around 2 times lower than that in normal breast tissue. As the patient recruitment protocol excluded patients with a mass smaller than 1 cm in diameter in this pilot study, the longest dimension of the smallest tumor we detected was approximately

0.8 cm (Fig. 12d). This tumor was located in the right breast of Patient 7, who was recruited due to a larger tumor in her left breast. However, with 255 μm spatial resolution and refined noise-equivalent sensitivity, SBH-PACT has the potential to detect smaller breast cancers once angiogenesis sufficiently progressed. Patient 3 had DD cup breasts, and her breast was compressed against the chest wall to roughly a cylinder. The tumor in her breast had a depth of ~ 3.2 cm (elevational distance from the nipple), which was the deepest among the recruited patients (Fig. 12d).

Assessing Breast Cancer Response to Neoadjuvant Chemotherapy

After demonstrating breast cancer detection using SBH-PACT, we further extended our study to understand breast cancer response to neoadjuvant chemotherapy (NAC). NAC has contributed to improving the outcomes of breast cancer patients by increasing the likelihood of breast conservation and by providing important prognostic information based on response to treatment. Exceptional responders to NAC may have complete eradication of breast cancer, known as a pathologic complete response (pCR), resulting in markedly better cancer outcomes. Overall, 20% to 30% of patients who receive NAC fit this profile and these patients may not benefit from definitive surgery after NAC. However, non-operative management of breast cancer treated with NAC is predicated on the ability to identify pCR. Unfortunately, the limited accuracy of the current breast imaging and noninvasive methods of identifying pCR demands pathologic confirmation. As such, post-NAC surgery remains standard of care. The primary objective of this study is to determine correlation of PACT measurements with clinical response in breast cancer to NAC and to determine if PACT can determine or predict pCR in patients treated with NAC.

In this ongoing study, we have imaged 3 patients, each of whom have taken PACT measurements prior to commencing NAC and after 2 cycles (~ 1 month) of NAC. Figure 13 shows PACT images of one patient. She responded to NAC well after 1-month treatment and the tumor reduced in size. The same assessment has been made by standard clinical examinations. The vessel density maps in Fig. 13b automatically detect the changes in tumor sizes by quantifying blood vessel densities. In addition to quantifying the vessel density, we further assessed the irregularity (entropy) of the blood vessels and enhanced the irregular ones (Fig. 13c) to make the tumors more easily identified.

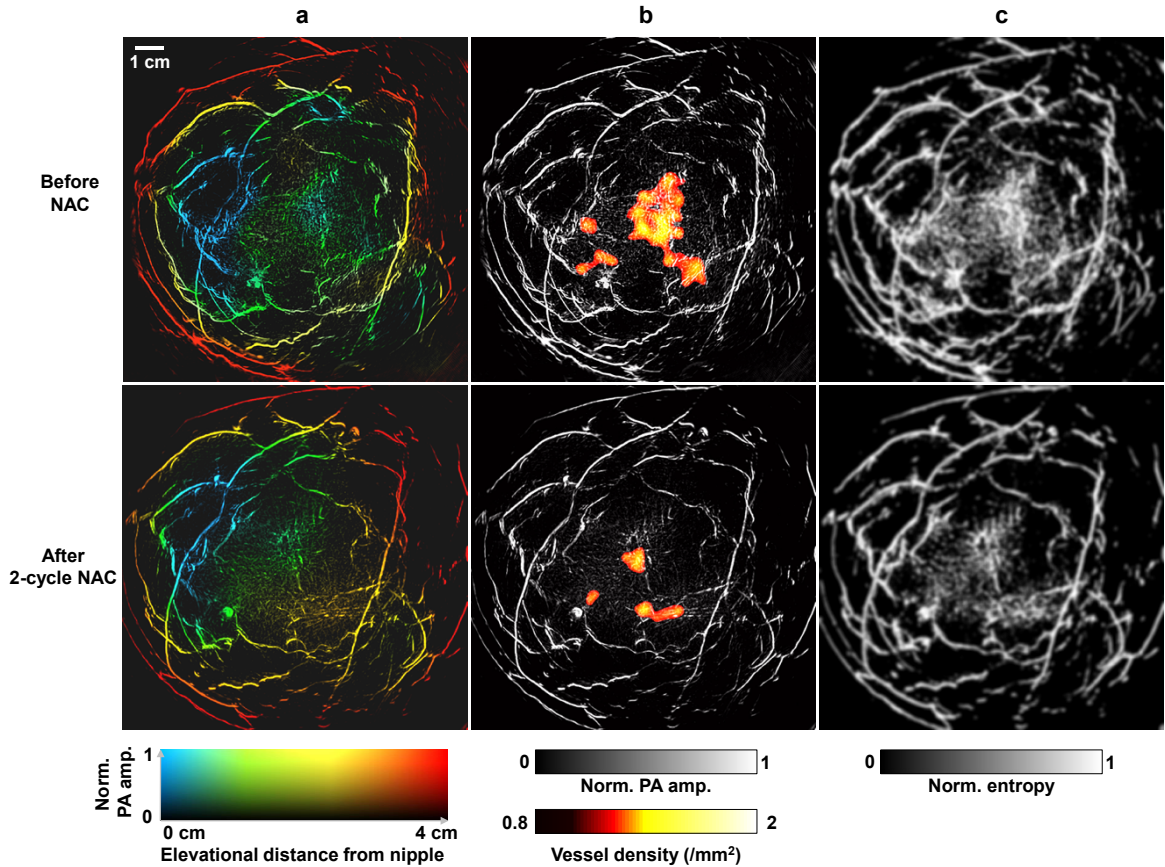


Figure 13. SBH-PACT of a patient before and after the 2-cycle NAC treatments.

We will recruit 80 breast cancer patients for this study. The goals of phase I (n = 10) are to fine-tune the imaging system and to develop detailed imaging protocols. All subtypes of

breast cancer patients who are treated with NAC are eligible. At the training stage (phase II, $n = 30$), the utility of each measurement in predicting pCR will first be determined. Then a multivariate logistic regression model will be constructed, in order to identify the regression coefficients of PACT's measurements and the threshold to dichotomize outcomes (pCR vs non-pCR). In phase III ($n = 40$), we will test our model built in the training phase and categorize the treated cancer as either pCR or non-pCR prior to surgery. The predicted results based on the PACT variables will then be compared with the reported final pathologic assessment of treatment response in the surgical specimen to determine the sensitivity, specificity, positive predictive value and negative predictive value as well as the area under the ROC curve.

Data Processing and Analysis

Half-time PA reconstruction in 2D and 3D modes

We used the half-time universal UBP algorithm [21] to reconstruct all images in this work. In 2D imaging mode, the time-domain PA signals generated by each laser pulse were back-projected to a 2D imaging plane. Determined by the acoustic divergence angle ($\sim 9.0^\circ$) at FWHM in the elevational direction (Fig. 8a), the elevational resolution at the center was ~ 16.1 mm.

Alternatively, when working in 3D mode, the ultrasonic transducer array scanned the entire breast from the chest wall to the nipple. The time-domain PA signals acquired at all elevational scanning steps were then back-projected simultaneously into the 3D space. To accommodate the acoustic divergence angle in the elevational direction, 3D-UBP added a weight to the back-projected PA signals at different elevational divergence angles (Fig. 8a). To accurately reconstruct objects in the Fraunhofer zone, we back-projected PA signals

from virtual transducers located at the transition points between the Fresnel and Fraunhofer zones [66]. Sharing the same in-plane resolution as the 2D mode, 3D-UBP provided an improved elevational resolution of 5.6 mm.

The full-ring transducer array with 512 elements could spatially well sample objects — according to the spatial Nyquist criterion — within a FOV of ~ 39 mm in diameter [22]. To eliminate aliasing caused by under-sampling in regions outside of this FOV, we low-pass filtered PA signals with cut-off frequencies determined by the distance to the center of the ring array.

Each volumetric image was first reconstructed with a voxel size of 1 mm in the elevational direction and 0.1×0.1 mm² on the horizontal plane. In each horizontal slice, we applied Hessian-based Frangi vesselness filtration [22] to enhance the contrast of blood vessels with diameters ranging from 3 to 12 pixels. In each filtered slice, adaptive thresholding was used to segment blood vessels [67], followed by morphology filtration for single-pixel elimination. In the elevational direction of each filtered volumetric image, we selected voxels with the largest PA amplitudes and then projected their depths to form a 2D image. We applied median filtration with a window size of 3×3 pixels to the depth image. Another median filtration with a window size of 6×6 pixels was further applied inside the segmented vessels to the segmented vessels' depths. Different RGB (red, green, blue) color values were assigned to discrete depths (vertical color bar in Fig. 9b). Finally, the 2D depth-resolved color-encoded image was multiplied by the MAP image pixel by pixel to represent the maximum amplitudes (horizontal color bar in Fig. 9b). To further reduce noise and improve image quality, we also tuned the above parameters in 2D slices at different depths.

Vascular diameter measurement

Vascular diameters were accurately measured by identifying vessel boundaries through a correlation-based template matching method [67]. The templates were generated through simulation (Fig. 14). The impulse responses of all ultrasonic transducers were used to simulate the images of vessels with different sizes (0.5–2.0 mm) and orientations. The diameters of vessels chosen from the SBH-PACT breast images were quantified by matching the reconstructed vessel images with the generated templates.

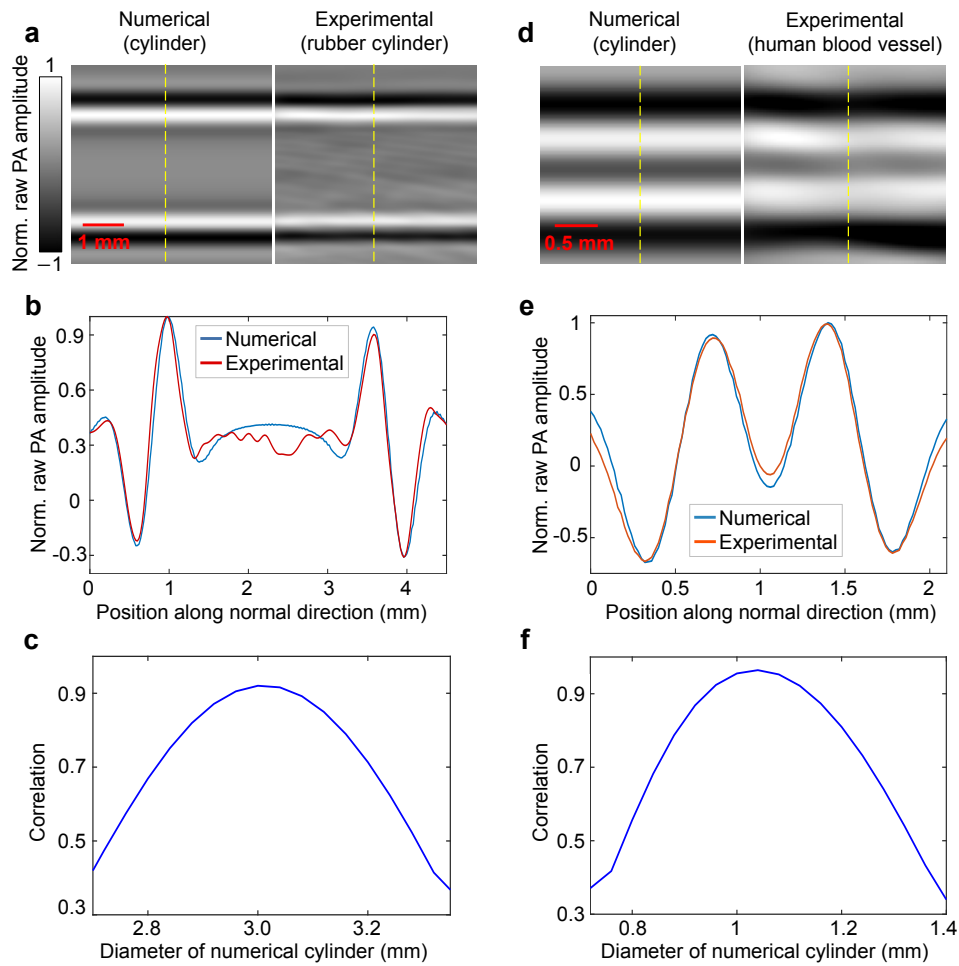


Figure 14. Vascular diameter quantification. (a) (left) Numerically simulated image of a cylinder with a diameter of 3 mm. (right) Experimental image of a rubber cylinder with a pre-known diameter of 3 mm. (b) Photoacoustic amplitude distributions along the normal

directions (yellow dashed lines) of the numerical cylinder and the rubber cylinder. (c) Correlation coefficients between numerical cylinders with different diameters and the rubber cylinder. (d) (left) Numerically simulated image of a cylinder with a diameter of 1.04 mm. (right) *In vivo* image of a section of a human blood vessel. (e) Photoacoustic amplitude distributions along the normal directions (yellow dashed lines) of the numerical cylinder and the blood vessel. (f), Correlation coefficients between numerical cylinders with different diameters and the blood vessel.

Arterial vessel mapping

Working in 2D imaging mode, SBH-PACT was able to monitor blood flow-mediated arterial fluctuation (Fig. 9e–g). After removing displacement through rigid transformation, we analyzed the pixel value fluctuation during a patient’s breath hold (~10 s). We found that arteries fluctuated much more than veins at the frequency of the heartbeat. The fluctuation of the pixel values in the artery indicated the changes associated with arterial pulse propagation (Fig. 9f).

To separate fluctuations caused only by heart beats, frames with strong motion caused by body movement were first removed. The entire imaging field was then divided into 16 slightly overlapping subdomains. In each subdomain, we chose the first frame as the reference frame; other frames were registered to it through rigid transformation, optimizing the frame–frame correlation. In each subdomain, a Gaussian filter with a radius of 0.2 mm was applied to all registered frames to reduce high spatial-frequency noise. We then applied Fourier transformation to each pixel’s value through all the frames. The fluctuations in pixel values induced by arterial pulse propagation were quantified within the frequency range (1.0–1.6 Hz) of heartbeat cycles [68].

Tumor segmentation

SBH-PACT showed breast masses by revealing a greater density of blood vessels, presumably due to angiogenesis, in tumor regions. To segment tumors automatically, we extracted the vessel skeleton and produced a vessel density (number of vessels / area) map of the breast. The regions with the highest vessel density highlighted the breast mass of interest (Fig. 10d).

The dense vessels in the nipple would affect the automatic tumor segmentation. Therefore, the shallowest slices containing the nipple were first removed. The remaining slices were used to generate the MAP image. A vessel mask was generated from the MAP by Hessian filtering and threshold-based segmentation. Based on the mask, vessel centerlines were extracted by removing boundary pixels. The vessel centerlines were broken into independent vessels at junction points. To reduce noise further, we removed independent vessels with lengths less than 3 pixels (255 μm spatial resolution divided by 100 μm pixel size is approximately 3). A 2 mm \times 2 mm window was then used to scan the entire image. At each scanning location, the number of vessels (independent segments) inside the window was counted and assigned to the center pixel in the window. The vessel density was quantified as the number of vessels divided by the window area. To compute the average vessel density of the whole breast, we included pixels inside a 10 cm-diameter circle around the image center.

To demarcate breast tumors from MAP images, we first identified suspicious regions where blood vessel densities were higher than a threshold, which was set to each whole-breast's average plus 2.0 times the STD. Among the eight affected breasts, the smallest suspicious region had a diameter of 1 mm. We then counted the numbers of pixels in each contiguous

region and rejected the regions with pixel counts fewer than 1855 (18.55 mm^2) to eliminate false positive cases. The remaining contiguous regions were labeled as tumors and the smallest one had a longest dimension of 8 mm (Fig. 12d). In comparison, contrast-enhanced MRI on a 1.5 Tesla scanner can detect breast tumors as small as 4 mm, which is similar to the smallest size of tumors detectable by X-ray mammography [69, 70].

Elastographic study

SBH-PACT's high imaging speed enabled differentiation in compliance between tumors and surrounding normal breast tissues, providing another contrast for detecting breast cancer. We first performed SBH-PACT elastographic measurements on a breast phantom. The phantom comprised a ball with 7% agar (mimicking breast tumor) embedded in a base of 2% agar (mimicking normal breast tissue) [71]. Chopped human hair was uniformly distributed in the phantom to mimic small blood vessels. Working in 2D imaging mode, SBH-PACT quantified the relative area changes in a cross section when minor deformations were induced by periodic compressions ($\sim 0.25 \text{ Hz}$) on top of the phantom. Due to the low elevational sectioning power of 2D imaging, objects in 2D frames were mainly influenced by coronal dilation instead of elevational displacement. Accordingly, SBH-PACT elastography clearly revealed the agar ball with correct size and location (Fig. 11). No obvious differences were observed in the concentration of the hair fiber between the balls and the phantom base.

To assess deformations over time, the first frame was taken as a reference. Other frames were registered to the first frame through a non-rigid demon algorithm [72] in Matlab. For each pixel of registered frames, the STD of the value variations was calculated. Pixels with relatively small STDs were stably registered and used for deformation quantification. The

entire image was then segmented into $2\text{ mm} \times 2\text{ mm}$ squares. One stably registered pixel was chosen from each square, and triangular grids were further generated from these registered pixels. The triangular grids were mapped back to the original unregistered frames, and their areas were calculated. For each grid, Fourier transformation was applied to quantify the area variation at the frequency of periodic compression, and amplitudes were assigned to the pixels inside this triangle to generate the deformation map. To further reduce noise, 100 deformation maps were generated with randomly registered pixels in the squares. The final image is the average of the 100 deformation maps.

To conduct SHB-PACT elastography of the breast, patients were asked to breathe normally. The chest wall pushed the breast against the agar pillow, elevationally generating a deformation of the breast in the coronal plane. We used the same method to quantify the change of area between blood vessels in the breast. Tumors, being stiffer, could be identified in areas with less deformation than normal breast tissue.

Chapter IV

3D PACT OF HUMAN BRAIN

SBH-PACT provides high in-plane resolution (255 μm) but suffers from poor elevational resolution (5.6 mm), thus has difficulty in accurately quantifying volumetric parameters. Therefore, we developed an improved PACT system that can provide isotropic resolution in 3D space while maintaining the deep penetration and high speed of SBH-PACT. We have validated the new system by imaging a healthy human breast and brain with high spatiotemporal resolution. The system will be utilized to image a few hemicraniectomy patients and then be moved to the Children's Hospital of Los Angeles for neonatal brain imaging.

Introduction and Motivation

The BRAIN Initiative calls for novel approaches for entirely new or next-generation noninvasive large-scale, high-resolution recording of the human brain. These new approaches are expected to be ideally noninvasive and translatable to humans. Although fMRI offers sub-millimeter spatial resolution, it is generally considered a low sensitivity technique. The functional signal in Blood-oxygen-level dependent (BOLD) fMRI shows a nonlinear relationship to the Hb concentration and suffers from substantial tissue background. Optical-only imaging, e.g., diffuse optical tomography (a.k.a. functional NIR spectroscopy), suffers from low spatial resolution due to light diffusion [2]. Similarly, ultrasound-only imaging—is difficult to use in humans because the ultrasonic waves are attenuated and distorted twice by the skull on both transmission and reception.

To address these issues, we developed a massively parallel high-speed high-resolution full-view 3D PACT system (3D-PACT), akin to fMRI, for fast/ultrafast anatomical and functional brain imaging. PACT offers comparable spatial resolution but can potentially be made faster than fMRI. It is directly sensitive to both oxy-hemoglobin (HbO₂) and deoxy-hemoglobin (Hb), which can be detected with a low tissue background. Moreover, the PACT signal possesses linear relationships with HbO₂ and Hb concentrations. Other potential benefits of PACT over fMRI include open imaging platforms, minimal site requirements, and less system maintenance.

System Construction and Characteristics

The 3D-PACT consists of four main modules: a laser module to excite PA waves from the brain cortex, an ultrasonic detection module to record the PA waves, a signal amplification and data acquisition module, and a mechanical scanning module to provide azimuthal sampling (Fig. 15). The system has 4 arc ultrasonic transducer arrays (1024 parallel channels) with per-element ultra-low-noise amplification and DAQ for high-speed, 3D, and spectroscopic PACT of human brains *in vivo*. It provided dense ultrasonic sampling on a hemispherical detection surface in just 10 seconds to fulfill the spatial Nyquist sampling criterion (i.e., spacing < wavelength/2). The 3D-PACT is orders of magnitude faster and more sensitive than our preliminary transcranial PACT systems, advancing PACT to the presently achievable limit.

Two types of laser, Nd:YAG and Ruby, have been utilized to generate dual-wavelength contrasts at HbO₂-dominant 1064 nm and Hb-dominant 694 nm, allowing measurement of HbO₂ [73] in addition to Hb (measurable by BOLD fMRI) as both are indicators of neural metabolism [74]. The laser beams are coupled and delivered through an engineered diffuser

installed in the light aperture to irradiate the FOV on the head. This design ensures that the laser beam is unaffected by the rotation of the array, which is important to avoid PA signal fluctuations due to laser illumination so that small functional neural signals can be teased out. The optical fluence on the skin surface satisfied the ANSI safety standards [20].

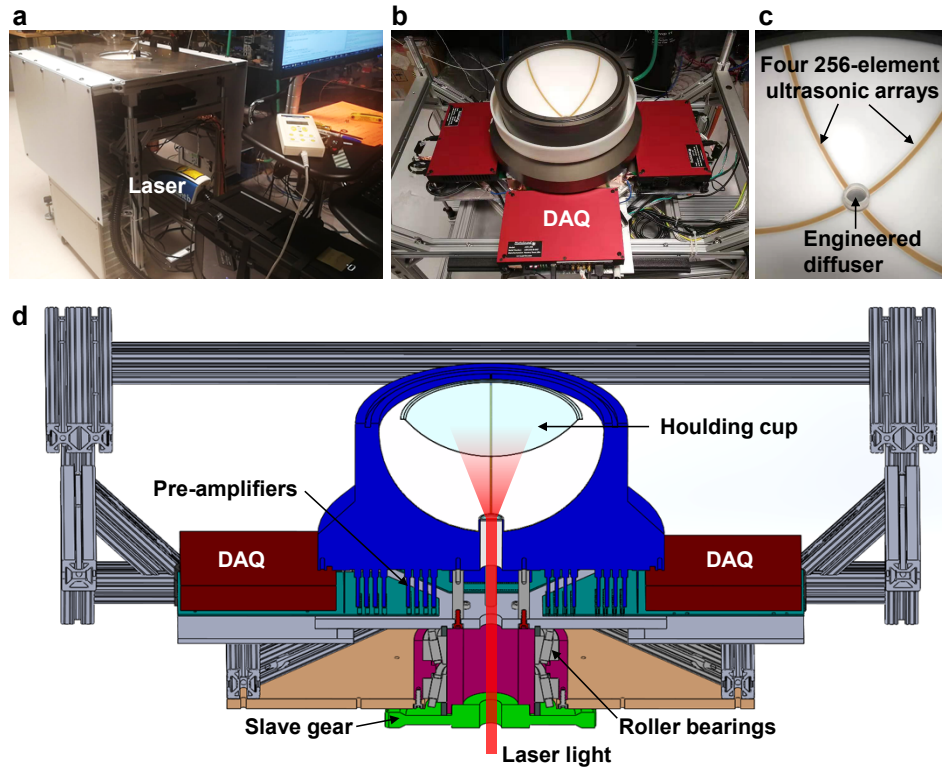


Figure 15. 3D-PACT system. (a) Photograph of the 3D-PACT system. The whole system is mounted on wheels. (b) Photograph of the system with the bed top and side panels removed. (c) Closeup view of the ultrasonic transducer arrays. (d) Cut-away view of the system schematic.

Four ultrasonic transducer arrays are integrated on the inner surface of a 26-cm-diameter hemispherical bowl that is coated with white plastic to reflect (recycle) the back-scattered light. 1024 ultrasonic transducer elements are evenly distributed on 4 quarter rings. Each element of the designed transducer has an active area of $0.6 \times 0.7 \text{ mm}^2$ with a 0.73-mm pitch. The central frequency is 2.25 MHz with a one-way -6-dB fractional bandwidth of

~80%. To separate the human subject with the imaging system, we mounted a disposable holding cup that is made by transparent membrane to cover the imaging aperture. The space between the holding cup and the ultrasonic detection module is filled with deuterium oxide (D₂O) for acoustical coupling because D₂O absorbs NIR light much less than water.

Customized pre-amplifiers (32 × 32 channels, 51-dB gain) are connected to the transducer array directly, amplifying the signal before cable noise spoils the SNR. Four 256-channel DAQ boards (PhotoSound, Inc., 40-MHz sampling rate, programmable amplification up to 51 dB, 12-bit dynamic range) receives all data in parallel. The digitized RF data are directly transferred to a workstation through USB 3.0. A mechanical scanning system rotates the transducer array to sample the object azimuthally over the hemisphere. With this design, a spatial resolution of ~0.28 mm has been achieved.

Geometric Correction in 3D-PACT

Due to manufacturing errors, the geometric position of each ultrasonic transducer element needed to be calibrated. We imaged a point source placed at multiple positions within the FOV and iteratively optimized the geometric location of each transducer element. To make a point source that emit strong PA waves, a point absorber (~100 μm) was glued to an optical fiber tip such that most of the light coupled into the fiber was absorbed. Because the arrays' housing was coaxially aligned and mounted, we assumed all the transducer elements share the same rotation axis.

The geometric relationship of the point source and each transducer element can be described by the following quadratic equations:

$$(x_m - x_n)^2 + (y_m - y_n)^2 + (z_m - z_n)^2 = (c \cdot t_{m,n})^2$$

$$m = 1, 2, \dots, M; n = 1, 2, \dots, N \quad (8)$$

Here, M and N are the number of point sources and elements, respectively; (x_m, y_m, z_m) denote the location of the m -th point source; (x_n, y_n, z_n) represent the location of the n -th transducer element; $t_{m,n}$ is the acoustic propagation time from the m -th point source to the n -th element; and c is the speed of sound in water.

We know $t_{m,n}$ precisely since the DAQs samples at 40 MHz. We have initial estimations of the unknown parameters c from the water temperature measurement, (x_m, y_m, z_m) from the reconstructed images, and (x_n, y_n, z_n) from the manufacture's specifications.

Since our initial estimations were assumed to be close, we applied Jacobi iteration to find the true values of (x_n, y_n, z_n) . In each iteration, we updated the following parameters:

(1) Speed of sound c

$$c = \frac{1}{N} \sum_{n=1}^N \sqrt{(x_m - x_n)^2 + (y_m - y_n)^2 + (z_m - z_n)^2} / t_{m,n} \quad (9)$$

(2) Point source location (x_m, y_m, z_m)

To solve (x_m, y_m, z_m) , we subtracted the following Eq. (10) from Eq. (8).

$$(x_m - x_{n-1})^2 + (y_m - y_{n-1})^2 + (z_m - z_{n-1})^2 = (c \cdot t_{m,n-1})^2 \quad (10)$$

Then, we had

$$2(x_n - x_{n-1})x_m + 2(y_n - y_{n-1})y_m + 2(z_n - z_{n-1})z_m = (c \cdot t_{m,n-1})^2 - (c \cdot t_{m,n})^2 + x_n^2 + y_n^2 + z_n^2 - x_{n-1}^2 - y_{n-1}^2 - z_{n-1}^2 \quad (11)$$

Since M is much less than N , we applied the least squares method to solve (x_m, y_m, z_m) .

(3) Element location (x_n, y_n, z_n)

Since the element size is much larger than the geometric error, we consider the radial error only. We define radial calibration factor α_n to confine the geometric error along the radial axis.

$$(x_m - \alpha_n x_n)^2 + (y_m - \alpha_n y_n)^2 + (z_m - \alpha_n z_n)^2 = c_m^2 (t_{m,n} - t_0)^2 \quad (12)$$

where α_n can be directly solved from the quadratic Eq. (12).

We repeatedly updated the above parameters 10 times, and their values converged to provide an optimal solution. Figure 16 shows the variation of the radial calibration factor α_n and Fig. 17 shows the images of a leaf skeleton reconstructed before and after geometric correction. The improvement in image quality is clear after correction. The images were acquired by scanning the array 90 degrees with 100 steps in 10 seconds. The laser has a repetition rate of 10 Hz, and each pulse has an energy of 750 mJ at 1064 nm.

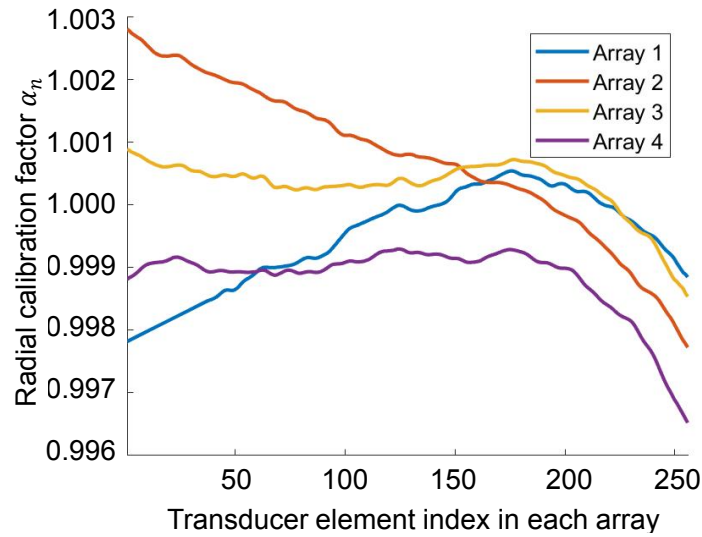


Figure 16. Radial calibration factor α_n of each ultrasonic transducer element.

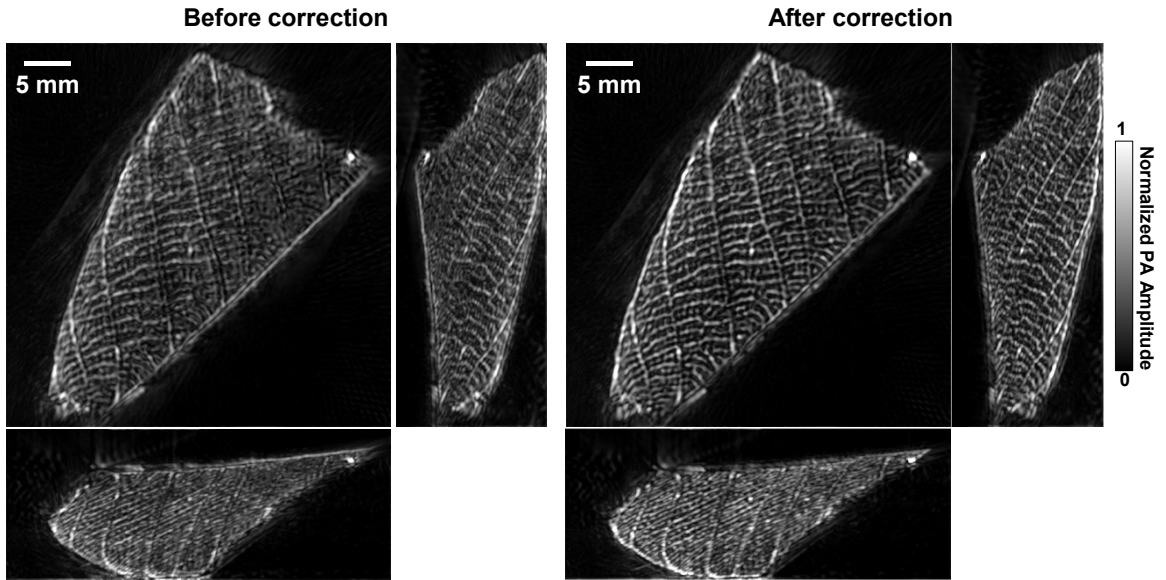


Figure 17. MAP images of a leaf skeleton reconstructed before and after geometric correction.

***In Vivo* 3D PACT**

After optimizing the system using phantoms, we first performed *in vivo* tests by imaging a healthy human breast. Fig. 18 shows three projections of the 3D breast. Since we designed the optical illumination for neonatal brain imaging, the light was expanded to a diameter of ~6 cm. However, such a beam could not cover the entire C-cup breast. Accordingly, the deep blood vessels near the peripheral regions were not revealed as clearly as those near the center. In the breast image, the system was validated to visualize the vasculature down to an apparent vascular diameter of 275 μm and to penetrate up to 3.5 cm. The nipple can be visualized at 4:30 o'clock 3 cm away from the image center. The breast images were acquired by scanning the array 90 degrees with 100 steps in 10 seconds. The laser has a repetition rate of 10 Hz and each pulse has an energy of 2.0 J at 1064 nm. Similarly to SBH-PACT, we asked the subject to take a single breath hold of 10 seconds to minimize motion artifacts.

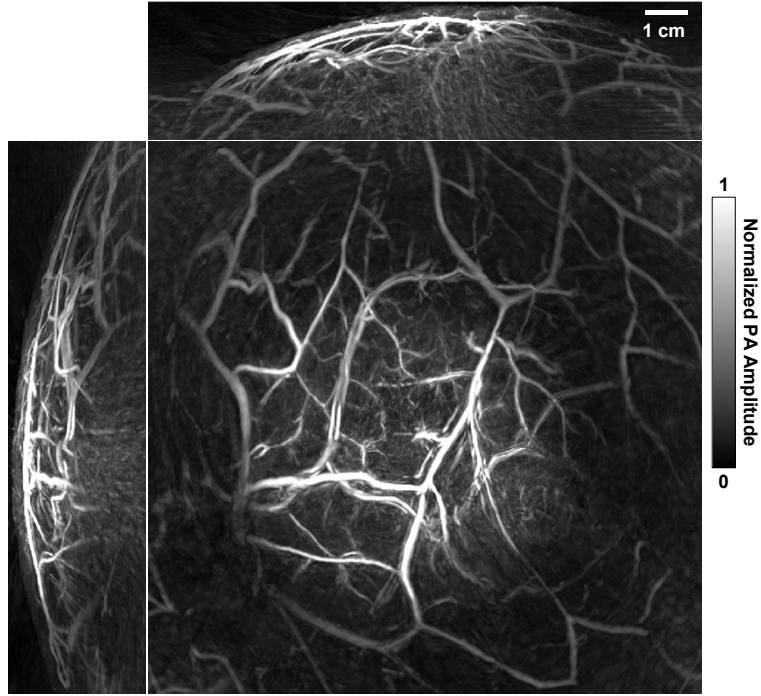


Figure 18. MAP images of a healthy human breast acquired by 3D-PACT within a single breath hold of 10 seconds.

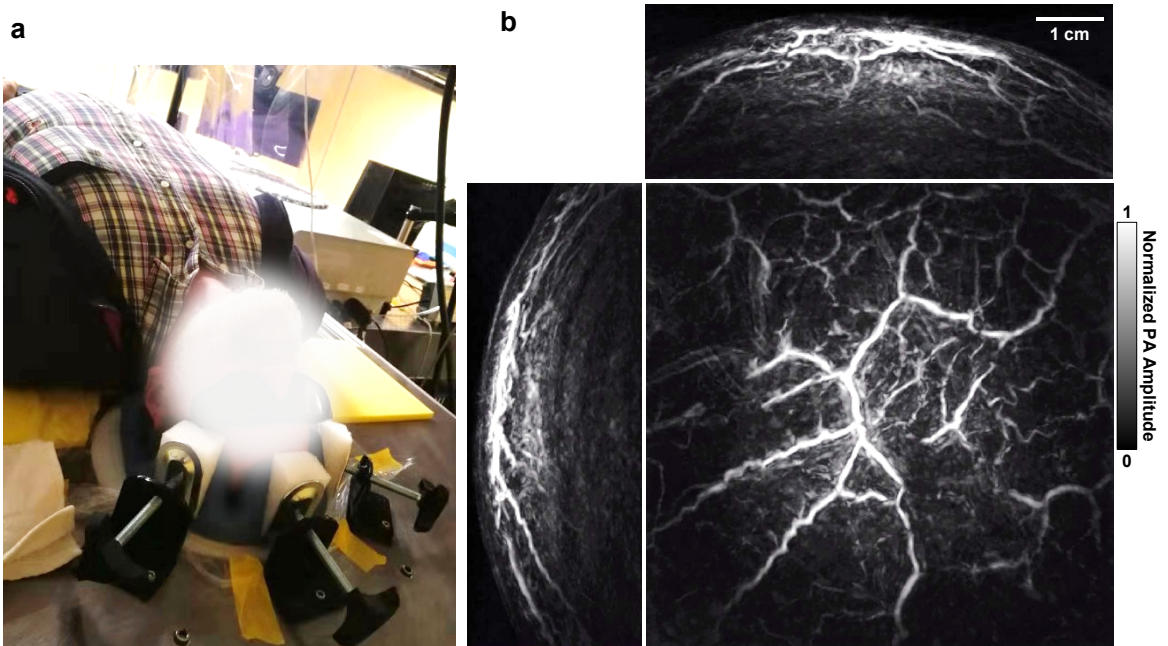


Figure 19. 3D-PACT of a healthy human head. (a) Photograph of a healthy subject being imaged. (b) MAP images of a healthy human head acquired by 3D-PACT within 10 seconds.

We further imaged a bald healthy subject using the 3D-PACT system. Figure 19a shows a photograph taken during the measurement and figure 19b shows the blood vessel network, primarily from the scalp. Since the system has a center frequency of 2.25 MHz, which is chosen primarily for neonatal brain and human breast imaging, it is challenging to detect the low-frequency PA signals through an adult human skull (see Fig. 25a).

Up to date, we have finished developing the system for neonatal brain imaging. We have validated the system on *in vivo* human breast and brain imaging. Since the neonatal skull has thinner thickness, softer hardness, and fontanel openings, we expect minor acoustic distortion and attenuation from the skull. We will further perform functional study by applying two wavelengths at HbO₂-dominant 1064 nm and Hb-dominant 694 nm.

Chapter V

MICROWAVE-BASED THERMOACOUSTIC TOMOGRAPHY

The high imaging speed and deep penetration is the key advantage of PACT. For light incident upon a homogeneous scattering half-space, expression for light fluence can be readily simplified as $F = F_0 \cdot e^{-(\mu_{eff} \cdot z)}$ that is well known as Beer's law. $\mu_{eff} = \sqrt{3\mu_a(\mu_a + \mu'_s)}$ is the effective absorption coefficient with absorption coefficient μ_a and reduced scattering coefficient μ'_s . Using NIR light, PACT can image blood vessels as deep as 4 cm in the human breast [75]. Nevertheless, deeper penetration is necessary for many clinical applications, including human brain or trunk imaging.

By simply replacing the laser with a pulsed microwave source and applying proper shielding of the transducers and electronics, microwave-induced TAT images can be generated using the same reconstruction algorithm. Different from visible light absorption in which heat is generated by non-radiative relaxation of excited electrons, microwaves generate heat through the electrical conductivity of tissues. Molecular relaxation and ionic conduction dominate this response at microwave frequencies, which generally relate to water and salt content. Therefore, the difference in dielectric properties of biological tissues can be revealed by TAT.

Introduction

Figure 20 shows the penetration depth of microwaves with respect to frequency in various biological tissues. The penetration depth is the inverse of the absorption coefficient. The

wide range of dielectric properties, related to physiological and pathological status, can lead to a high imaging contrast.

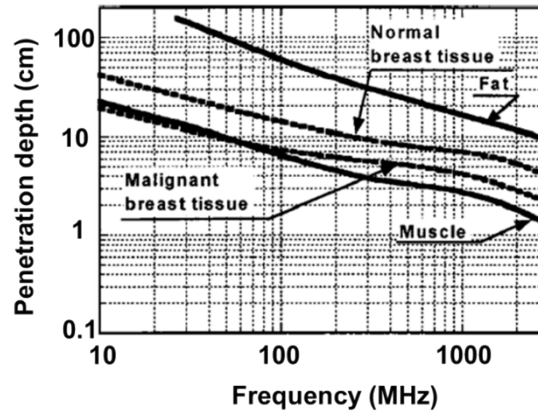


Figure 20. Penetration depths of various biological tissues versus the microwave frequency.

Several TAT systems have been developed [76-78] and have advanced TAT toward clinical application, while ongoing limitations remain to be addressed. Most TAT studies are limited to phantom imaging without validating the soft tissue contrast *in vivo*. And they did not analyze the specific absorption rate (SAR) to show the conformance to the safety standard for electromagnetic exposure. Our study demonstrates both soft tissue contrast *in vivo* and human-skull transcranial TAT, with an SAR lower than the safety limit.

Experimental Setup

To study the TAT contrast of soft tissue *in vivo*, we first imaged a live rat. A schematic of the experimental setup is shown in Fig. 21a. The rat was half-immersed in mineral oil. The microwave source had a peak power of 60 kW at 3 GHz and emitted 1.2- μ s microwave pulses at a 10-Hz repetition rate. We used a custom-made horn antenna to illuminate the rat. It was found that a uniform distribution of the electric field could be acquired within a plane 4.5 cm above the horn antenna (Fig. 21b). An ultrasonic transducer (2.25-MHz

central frequency, 0.5-inch diameter, cylindrical focus) was mounted on a rotary scanner. The thermoacoustic signals were first amplified by a two-stage low-noise amplifier and then transmitted to a DAQ card set to a sampling frequency of 20 MHz. To eliminate microwave interference, we shielded the ultrasonic transducer surface with a metal mesh (Fig. 21c). The dimension of the mesh holes was smaller than the microwave wavelength but larger than the ultrasonic wavelength.

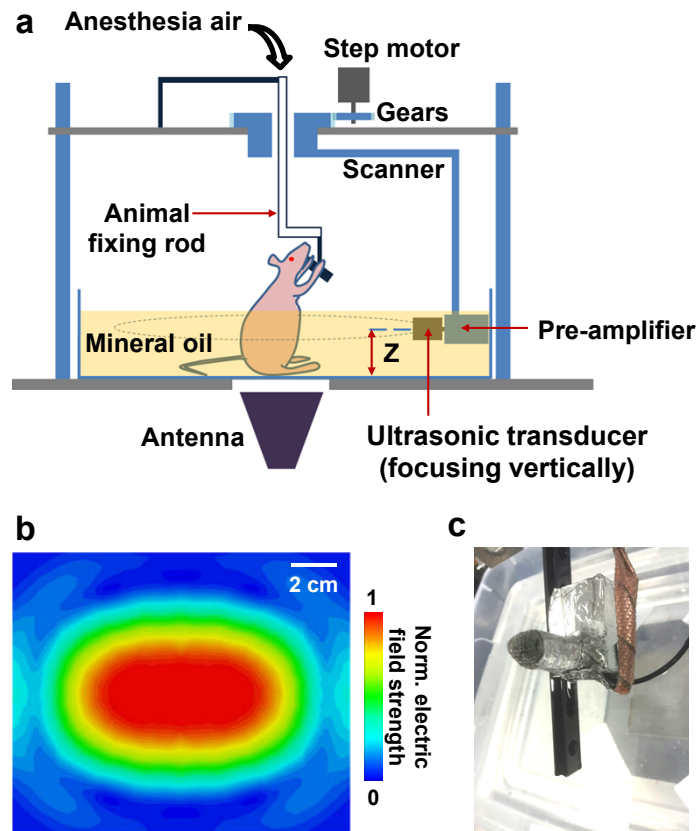


Figure 21. (a) Schematic of the experimental TAT system. (b) Simulated electric field distribution in a plane 4.5 cm above the antenna. (c) Photograph of the ultrasonic transducer shielded with metal mesh.

To image cross sections of the rat, we scanned the transducer circularly around the rat's trunk with 720 steps (0.5° step angle) and averaged signals 20 times at each scanning step. A half-time reconstruction algorithm was applied to mitigate image artifacts due to

heterogeneous acoustic properties [79]. We then sacrificed the rat and photographed its abdominal cross section after imaging. All experimental animal procedures followed the laboratory animal protocol approved by the Animal Studies Committee of Washington University in St. Louis.

After showing the TAT contrast of the soft tissue *in vivo*, we further demonstrated the penetration of the microwave and ultrasound through an adult human skull, which was donated by an 83-year-old Caucasian male. The thickness of the skull was inhomogeneous, ranging from 7 mm (temporal area) to 11 mm (frontal area). An agar cylinder was placed inside the skull. The microwave illuminates the skull from the bottom and the tank is housed with microwave absorbing foams. We also covered the skull opening with an agar pad to isolate the reflected microwave.

Because of the near-field illumination of microwave, an analysis of the SAR inside a head model is necessary to confirm the conformance to the safety standard for electromagnetic exposure. SAR measures the rate at which energy is absorbed by biological tissues when exposed to RF electromagnetic fields. SAR is calculated as $SAR = \sigma E^2 / 2\rho$, where σ is the electric conductivity (S/m), ρ is the mass density (kg/m^3), and E is the electric field (V/m). We developed a model of the human head illuminated by the antenna. The SAR distribution has a peak amplitude of 4×10^{-2} W/kg, which is far below the safety limit of the average SAR (2 W/kg) per IEEE EM safety standard [80].

Results

Different from the PAT, microwave leads to a lot of interference on the transducer surface. After shielding the transducer surface with metal mesh, the artifacts induced by microwave

interference are significantly reduced (Fig. 22). Figure 23 shows two phantom images and their photographs, validating the TAT system and the reconstruction algorithm. Both phantoms were around 2 cm thick, which was shorter than the microwave wavelength and can eliminate standing waves formed in phantoms.

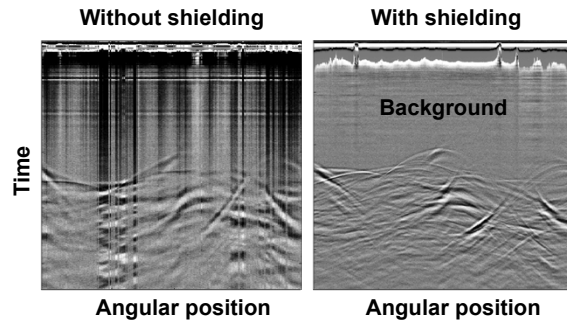


Figure 22. Diagrams of TAT signals acquired before and after shielding.

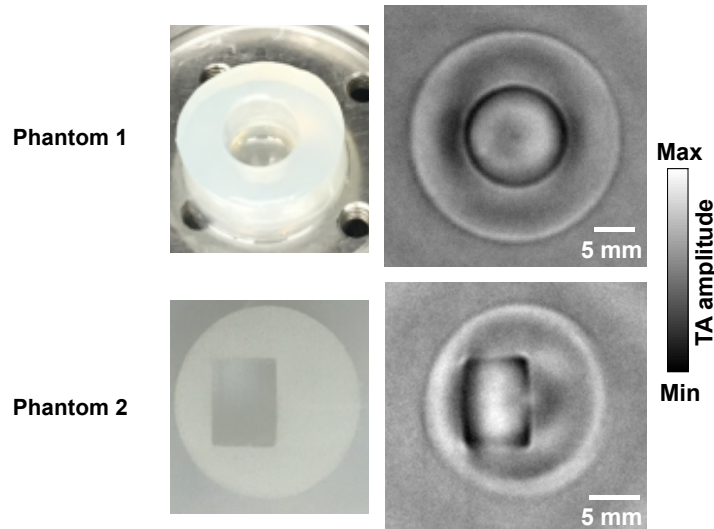


Figure 23. Two phantom photographs and their cross-sectional images acquired by TAT.

The cross-sectional TAT image of the rat's trunk agrees well with the corresponding photograph (Fig. 24a). The major vessels, spinal cord, and intestines are clearly revealed by TAT. Images of other cross sections ($Z = 4, 5.5,$ and 7 cm) are shown in Fig. 24b, where

Z is the distance above the bottom of the tank. Because of the deep penetration, we imaged up to 7 cm in rat's body, where shows the rat's ribs.

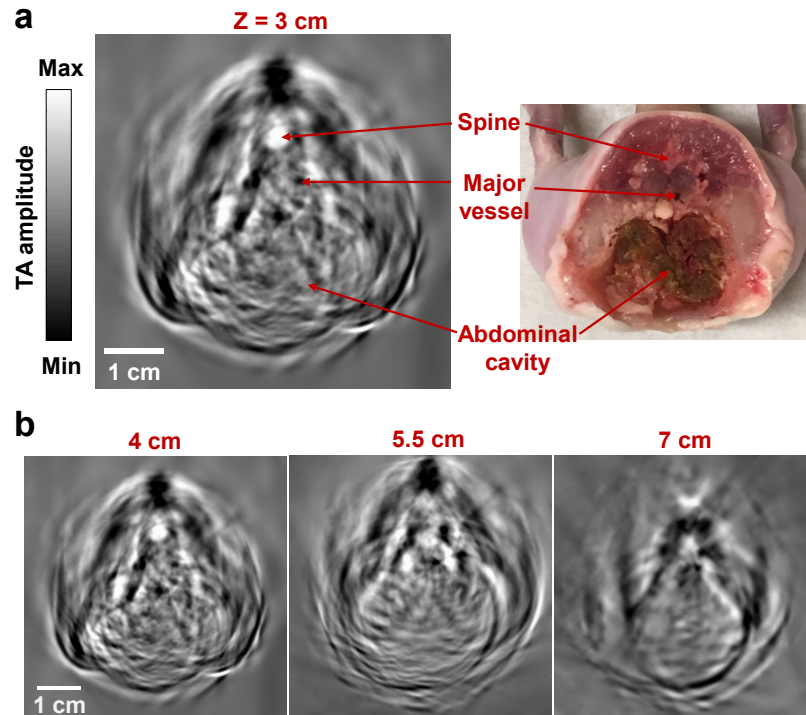


Figure 24. Cross-sectional images of the rat's trunk. (a) TAT image and the corresponding photograph. (b) TAT images of the rat's trunk at different cross sections.

The transcranial acoustic signals we received had a center frequency of 0.8 MHz (Fig. 25a). An ultrasonic transducer (1-MHz center frequency, 1-inch diameter) was used to detect the transcranial signals. We scanned the transducer circularly around the skull with 600 steps and averaged the signals 250 times at each scanning step. The TAT image clearly revealed the agar cylinder enclosed by the skull (Fig. 25b). To facilitate electromagnetic shielding, we used single-element transducer, preamplifier, and DAQ. Combining the microwave source with a transducer array will dramatically increase the imaging speed but requires careful shielding to protect the electronics from microwaves.

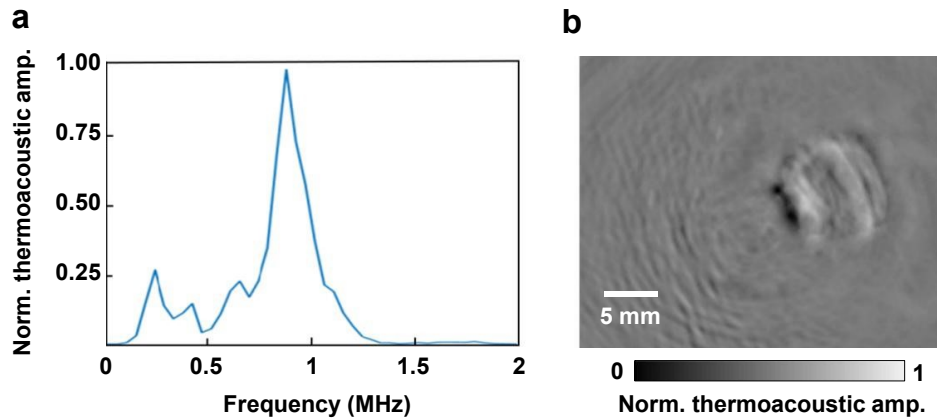


Figure 25. Transcranial TAT. (a) Normalized spectrum of the transcranial thermoacoustic signal. (b) Transcranial TAT image of the agar.

Summary and Outlook

Microwave-induced TAT reveals the difference in dielectric properties of biological tissues, providing a rich contrast showing tissue heterogeneity. Such a contrast would be a useful complement to the angiographic information provided by PAT for *in vivo* imaging. In addition to the imaging contrast, another key advantage of TAT is the deep penetration, which may not be feasible using NIR light. The transcranial image we acquired also demonstrates the potential of TAT for human brain imaging. By using a lower frequency microwave source, there is a potential for whole-body human imaging.

Due to the long microwave wavelength, objects are usually placed in the near field of the antenna. Therefore, the positions and orientations of the antennas need to be configured to distribute the microwave energy homogeneously in the tissue. Several techniques have been developed for this purpose. For instance, researchers used a power divider to equally distribute the microwave energy from a source into multiple antennas located around the object, allowing for uniform energy distribution.

Chapter VI

MULTI-CONTRAST PACT—MYOGLOBIN

TAT generates an imaging contrast of dielectric properties. To investigate more endogenous functional PACT contrasts, we demonstrated myoglobin oxygenation imaging. By applying microwave and NIR illumination, there is potential to acquire images with simultaneous dielectric property, hemoglobin, and myoglobin distributions, as well as their oxygenations.

Introduction and Motivation

Myoglobin is a primary oxygen-carrying protein expressed in skeletal muscle fibers and cardiac myocytes [81]. It functions as an oxygen-storage unit, facilitating the diffusion of oxygen from the cell membrane to mitochondria. Quantification of oxygen saturation of myoglobin (sO_2 -Mb) is of great interest in preclinical and clinical applications. For instance, an increased capability of myoglobin to buffer oxygen in skeletal muscle is closely related to chronic heart failure [82]. Myoglobin may also be used as a cardiac biomarker in blood stream, to help diagnose a heart attack [83].

Myoglobin has been demonstrated, along with hemoglobin, as a main muscle chromophore in the visible and near-infrared spectral regions [84]. Both myoglobin and hemoglobin have oxygen-bound and -unbound states that are spectrally distinct. Currently, optical spectroscopy [85], DOT [86], fMRI [87] are mainly used to quantify sO_2 -Mb *in vivo*; however, all three techniques have limitations. Optical spectroscopy and DOT have low spatial resolution, and fMRI is sensitive only to deoxygenated myoglobin [88].

In muscle tissue, the major absorbers in the visible and NIR spectral regions are oxygenated myoglobin (MbO_2), deoxygenated myoglobin (Mb), HbO_2 , and Hb . Figure 26a shows the optical absorption spectra of the major chromophores found in muscle. Their distinct spectra give us an opportunity to differentiate each chromophore. The optical absorption coefficient μ_a at wavelength λ can be expressed as

$$\mu_a(\lambda, s) = \ln(10) C_T(s) \left\{ f_{\text{MbO}_2}(s) \cdot \varepsilon_{\text{MbO}_2}(\lambda) + f_{\text{Mb}}(s) \cdot \varepsilon_{\text{Mb}}(\lambda) \right. \\ \left. + f_{\text{HbO}_2}(s) \cdot \varepsilon_{\text{HbO}_2}(\lambda) + f_{\text{Hb}}(s) \cdot \varepsilon_{\text{Hb}}(\lambda) \right\};$$

$$f_{\text{Hb}} = 1 - f_{\text{MbO}_2} - f_{\text{Mb}} - f_{\text{HbO}_2}, \quad (13)$$

where s denotes the oxygenation state; C_T is the total concentration of myoglobin and hemoglobin; f_{MbO_2} , f_{Mb} , f_{HbO_2} , and f_{Hb} are the respective concentration fractions of MbO_2 , Mb , HbO_2 , and Hb relative to the total concentration C_T . $\varepsilon_{\text{MbO}_2}$, ε_{Mb} , $\varepsilon_{\text{HbO}_2}$, and ε_{Hb} are the respective molar extinction coefficients of the four chromophores. Between two different oxygenation states ($s = a$ and b), the ratio of the measured PA signal amplitudes (P) can be written as follows [62]:

$$\frac{P(\lambda, a)}{P(\lambda, b)} = \frac{F(\lambda, a)}{F(\lambda, b)} \cdot \frac{C_T(a)}{C_T(b)} \cdot \frac{\mu_a(\lambda, a)}{\mu_a(\lambda, b)}, \quad (14)$$

Γ and η_{th} do not appear in the ratio because they do not change between different $s\text{O}_2$ states. For red and near-infrared light, the change in optical attenuation in the skin due to variations in $s\text{O}_2$ (e.g., from 90% to 30%) is less than 3% [89], mainly because of the high optical scattering and low volume fraction of blood in the skin. Therefore, we can neglect the change in local optical fluence due to variations in $s\text{O}_2$, i.e., $F(\lambda, a) = F(\lambda, b)$. In addition, if we assume that the total concentration C_T does not change, i.e., $C_T(\lambda, a) = C_T$

(λ, b) , the first two terms on the right hand side of Eq. (14) can be removed. To solve the remaining six unknowns r_{MbO_2} , r_{MbR} , r_{HbO_2} in the a and b states, we need to measure the PA signals at a minimum of six wavelengths.

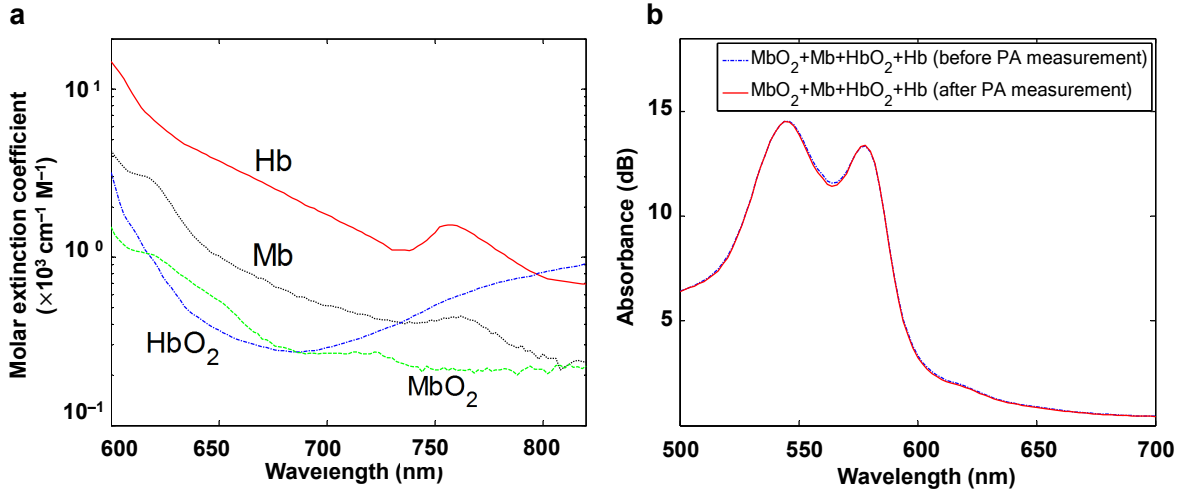


Figure 26. Optical absorption properties of myoglobin. (a) Absorption spectra of major chromophores found in muscle, measured at wavelengths from 600 nm to 820 nm. (b) Absorption spectra of a mixture of MbO₂ (60.7%), Mb (24.8%), HbO₂ (6.9%), and Hb (7.6%), measured using a spectrophotometer before and after the photoacoustic experiment.

Results

The source and the method adopted to prepare the solutions of pure MbO₂, Mb, HbO₂, and Hb were the same as reported in previous papers [84, 85]. A standard spectrophotometer measured the absorbance, which was the product of the molar extinction coefficient, molar concentration, and the pathlength of the cuvette. From the known molar extinction coefficients at various wavelengths and the pathlength of the cuvette, we derived the molar concentrations. To the mixture of MbO₂ and HbO₂, we added a moderate amount of sodium dithionite to partially deoxidize the sample, giving the spectrum shown in Fig. 26b (dashed line). From the spectrum, we calculated the concentration fractions of the four

chromophores as a reference. After PA measurement, we repeated the spectral measurement (solid line in Fig. 26b). We covered the cuvettes and the phantom with a piece of transparent film to avoid exposing the mixtures to the air during the two spectrophotometer measurements (~5 minutes).

We first performed a phantom study to validate our method. We made an agar cylinder with four square vertical tunnels (Fig. 27a). Each tunnel was 5 mm long, 5 mm wide, and 70 mm high, with a 3 mm spacing between tunnels. Initially, 0.11 mL 20% intralipid (deoxygenated) was injected in each tunnel. The reduced scattering coefficient of the intralipid solution was around 100 cm^{-1} at 700 nm [90]. Three mixtures of MbO₂, Mb, HbO₂, and Hb with the same total concentration and different concentration fractions were then added into the first three tunnels, and the fourth tunnel was filled with pure water. The absorption coefficients of the first three samples at 700 nm were respectively 0.23 cm^{-1} , 0.15 cm^{-1} , and 0.36 cm^{-1} . The samples in all tunnels had the same reduced scattering coefficient of 10 cm^{-1} at 700 nm.

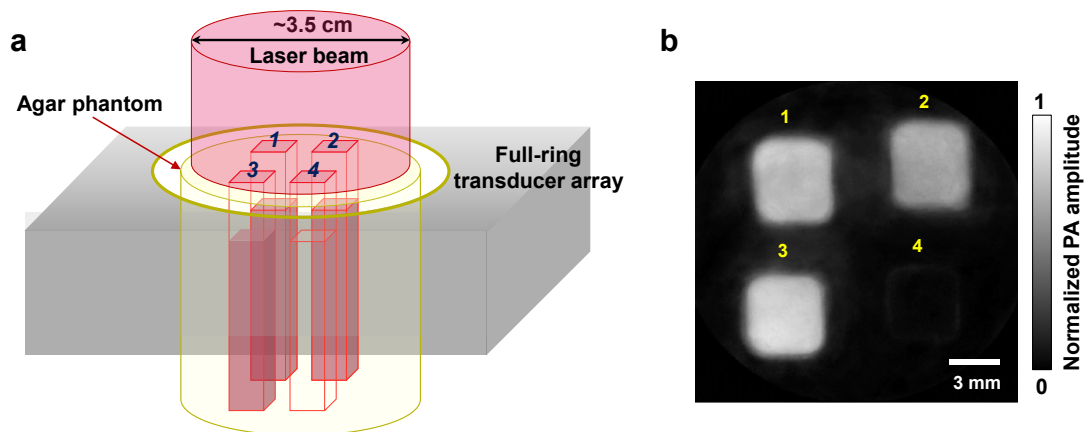


Figure 27. Experimental setup and a representative PA image of the phantom. (a) Schematic of the phantom setup. (b) Photoacoustic image of the phantom acquired at 600 nm.

We used a full-ring PACT system [18] to validate our model. The agar phantom was $\sim 5/6$ immersed in water and fixed at the center of the transducer array. The imaging plane was set at 2 mm below the sample's liquid surface. At the imaging plane, a 0.1 mm radial resolution and <0.25 mm tangential resolution were achieved. For multiwavelength imaging, we combined an optical parametric oscillator (OPO) laser and a Ti-Sapphire laser, each pumped by an Nd:YAG laser with a 10 Hz pulse repetition rate. After passing through a ground glass, the light beam was expanded and delivered onto the top of the phantom. The laser fluence at the phantom surface was around 2.6 mJ/cm^2 . We imaged the phantom at 600 nm, 620 nm, 640 nm, 734 nm, 757 nm, and 800 nm, with 60 times averaging at each wavelength. Figure 27b shows a representative image of the phantom acquired at 600 nm.

From the images acquired at each wavelength, we first averaged the PA signals within each tunnel, and then subtracted the water absorption (PA signal amplitude in tunnel #4) from the first three tunnels before substituting the data into Eq. (14). The spectral unmixing results are summarized in Table 1. In the table, the true concentration fractions were calculated by using the molar extinction coefficient of each chromophore and the spectrophotometer measurements of the mixture, e.g., Fig. 26b. The measured concentration fractions were in good agreement with the true values, with an average error of 10%. The accuracy is still sufficient to measure the $s\text{O}_2$ change *in vivo* from hyperoxia induced with 100% O_2 inhalation to hypoxia induced with 10% O_2 inhalation [62].

In the phantom experiment, the first three samples with different oxygenation levels served as the different oxygenation states required for the ratiometric $s\text{O}_2$ calculation by using equations (13) and (14). The estimated effective attenuation coefficients of the three samples were respectively 2.65 cm^{-1} , 2.14 cm^{-1} , and 3.34 cm^{-1} at 700 nm. Therefore, the

optical fluence at the imaging plane was different for each sample. The ratio between the light fluence in tunnel #1 and tunnel #2 was 0.91, and the ratio between the light fluence in tunnel #1 and tunnel #3 was 1.15. Because Eq. (14) assumes the optical fluence remains constant between different oxygenation states, the actual difference in optical fluence between different samples (i.e., different oxygenation states) was the major source for the sO_2 measurement errors.

Table 1. Summary of the phantom experiment results.

Concentration fraction	Tunnel #1		Tunnel #2		Tunnel #3		Tunnel #4 (water)
	True fraction	Measured fraction (\pm standard error)	True fraction	Measured fraction (\pm standard error)	True fraction	Measured fraction (\pm standard error)	
f_{MbO_2}	60.7%	59.5% ($\pm 2.4\%$)	78.5%	71.4% ($\pm 2.3\%$)	0	2.6% ($\pm 1.4\%$)	—
f_{Mb}	24.8%	22.1% ($\pm 1.7\%$)	0	2.3% ($\pm 1.3\%$)	85.5%	77.6% ($\pm 1.9\%$)	—
f_{HbO_2}	6.9%	8.3% ($\pm 2.0\%$)	21.5%	24.6% ($\pm 2.4\%$)	0	3.3% ($\pm 1.2\%$)	—
f_{Hb}	7.6%	10.1% ($\pm 1.5\%$)	0	1.7% ($\pm 0.9\%$)	14.5%	16.5% ($\pm 2.1\%$)	—

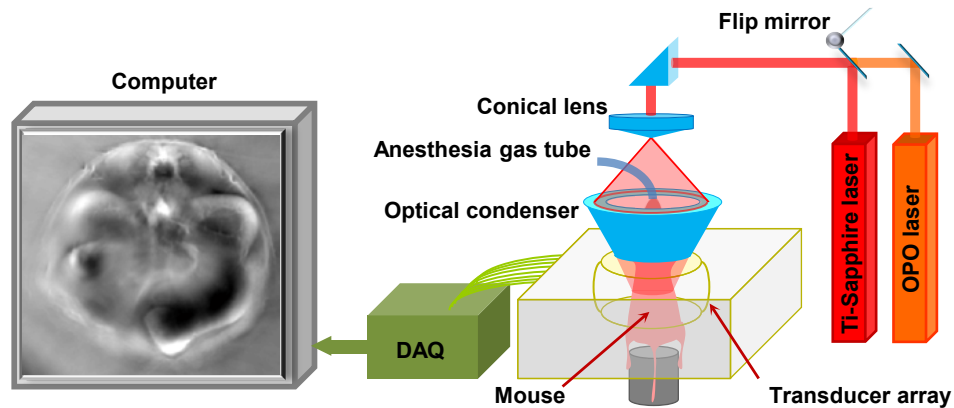


Figure 28. Schematic of the experimental setup for *in vivo* sO_2 measurement in backbone muscle.

To further test the method, we noninvasively imaged a systemic sO_2 change in the backbone muscle of a mouse *in vivo*. Figure 28 shows a schematic of the experimental setup. The sO_2 level in the backbone muscle was adjusted by challenging the animal with different oxygen concentrations in the inhalation gas. At first, the anesthesia gas was a mixture of pure oxygen and isoflurane, keeping the mouse in hyperoxia. We used 780 nm light with full-ring illumination to obtain a cross-sectional image of the mouse at the kidney level, shown in Fig. 28. We then adjusted the light to the mouse back to form a half-ring illumination to image the backbone muscle at six wavelengths. The laser fluence on the mouse's dorsal surface was around 25 mJ/cm².

We switched the six wavelengths one by one to image the mouse backbone region during hyperoxia. Then, we decreased the inhaled O_2 to 10% and increased N_2 to 90%, waited three minutes so the mouse was in hypoxia, and repeated imaging with six wavelengths. Finally, we increased the inhaled O_2 back to 100% and repeated the measurements, in order to compare the sO_2 -Mb values in two hyperoxic states. At each wavelength, we averaged 60 times.

To calculate the hemoprotein sO_2 , we first smoothed the PA images with a 5×5 median filter. We then substituted the measurements into Eq. (14) and calculated the pixelwise concentration fraction of MbO_2 , Mb, HbO_2 , and Hb. Figure 29a shows the distribution of myoglobin in hyperoxia (state *a*), and figure 29b shows the distribution of hemoglobin in the same state. These two images clearly differentiate the regions of the spinal cord, backbone muscle, and kidney, which conform to the background structural image (shown in Fig. 28). The relative changes in myoglobin and hemoglobin sO_2 from hyperoxia (state *a*) to hypoxia (state *b*) are shown in Fig. 29c and d, respectively. In Fig. 29c, the sO_2 -Mb

decreased primarily in the backbone muscle region when we reduced the inhaled O₂ concentrations. In Fig. 29d, we observe the hemoglobin sO₂ systemically decreases, in both the backbone muscle and other internal organs. Moreover, with the same hypoxic challenge, the hemoglobin sO₂ decreased faster than the myoglobin sO₂, probably due to the fact that myoglobin has higher oxygen affinity than hemoglobin.

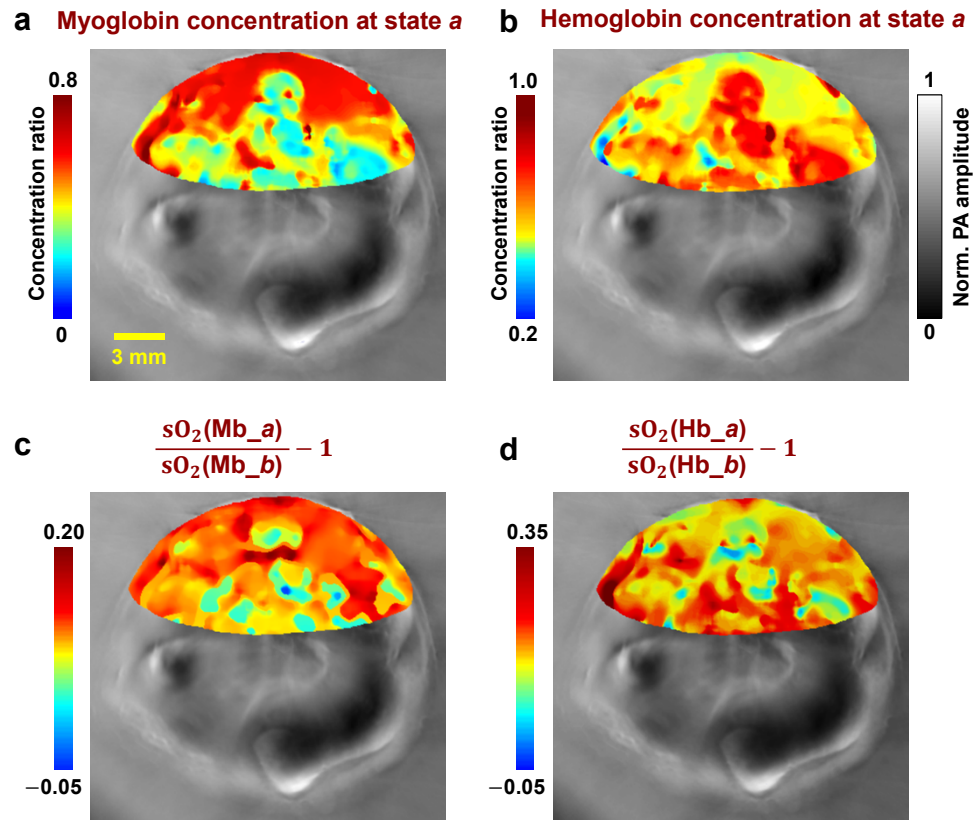


Figure 29. *In vivo* experimental results. (a-b) Concentration fraction of myoglobin (a) and hemoglobin (b) in hyperoxia (state *a*) (shown in color) overlaid on the structural image (shown in gray). (c-d) The relative change in myoglobin sO₂ (c) and hemoglobin sO₂ (d) from hyperoxia (state *a*) to hypoxia (state *b*) (shown in color) overlaid on the structural image (shown in gray). BM, backbone muscle; KN, kidney; SC, spinal cord.

Discussion

An accurate sO₂ measurement requires knowledge of the local optical fluence, which can be estimated through invasive measurements [91] or sophisticated modeling of light

transportation [22]. To address this issue, we used a ratiometric method based on the dynamics in sO_2 , where knowledge of optical fluence was not required. We neglected the change in optical attenuation in tissue due to variations in sO_2 , mainly because of the high scattering and low volume fraction of blood in the skin.

Since six wavelengths were used, the current *in vivo* measurements are not fast enough to monitor the dynamics of sO_2 -Mb changes. The imaging speed can potentially be improved by using faster wavelength switching. Direct validation of the *in vivo* sO_2 -Mb measurement in deep tissue is challenging. Invasive partial pressure of oxygen (pO_2) oximetry or fluorescence lifetime-based pO_2 measurement [92] might be a surrogate validation. Non-invasive *in vivo* measurements of sO_2 -Mb might be useful in medical and surgical procedures [93]. By taking advantage of the high spatial resolution of PACT, applications such as cardiac surgery and sports medicine might particularly benefit.

Chapter VII

HIGH-SPEED OR-PAM OF CORTICAL HEMODYNAMICS

Efforts to advance PACT mainly focused on increasing the imaging depth, inducing rich contrasts, and improving the reliability such that it can be used for clinical applications. In addition to PACT, another implementation of PAI—OR-PAM—has been translated from the bench to the bedside. As in PACT, we started with small animal imaging by using an existing benchtop system to gain initial insight. A high-speed OR-PAM system was applied to image the mouse cortical microhemodynamics. Afterward, the system was minimized to a handheld probe suitable for human skin imaging.

Introduction and Motivation

The hemodynamics of the mouse brain have been studied in detail by biomedical imaging modalities such as small-animal fMRI, wide-field optical microscopy, and two-photon microscopy. However, small-animal fMRI is primarily sensitive to deoxy-hemoglobin and is insufficient to resolve brain activities at length scales finer than 50 μm [94], wide-field optical microscopy lacks depth resolution [95], and two-photon microscopy relies on exogenously delivered fluorophores as the contrast agents [96]. Optical coherence tomography-based angiography exploits the optical contrast in dynamic backscattered light [97] and is complementary to PAI, which shows the optical absorption contrast. By acoustically detecting optical absorption in tissues, PAI is capable of anatomical, functional, molecular, and metabolic imaging of small animals, with highly scalable spatial resolution and penetration depth [7]. In particular, the rich spectroscopic and functional imaging

capabilities of PAI suggest it could be a powerful tool for brain disease diagnosis and neuroimaging studies [14, 39].

As a major implementation of PAI, OR-PAM provides capillary-level spatial resolution by tightly focusing the laser beam at depths within the optical diffusion limit [7]. In this chapter, we present a high-speed OR-PAM with micrometer-level resolution and a millisecond-level cross-sectional imaging speed over a millimeter-level field of view. Using this high-speed OR-PAM, we quantified the blood flow redistribution in response to spontaneous microhemorrhage, as well as to laser induced occlusions of single microvessels. We also imaged cerebral autoregulation (CA) on single microvessels in an intact mouse brain.

Methods

High-speed OR-PAM

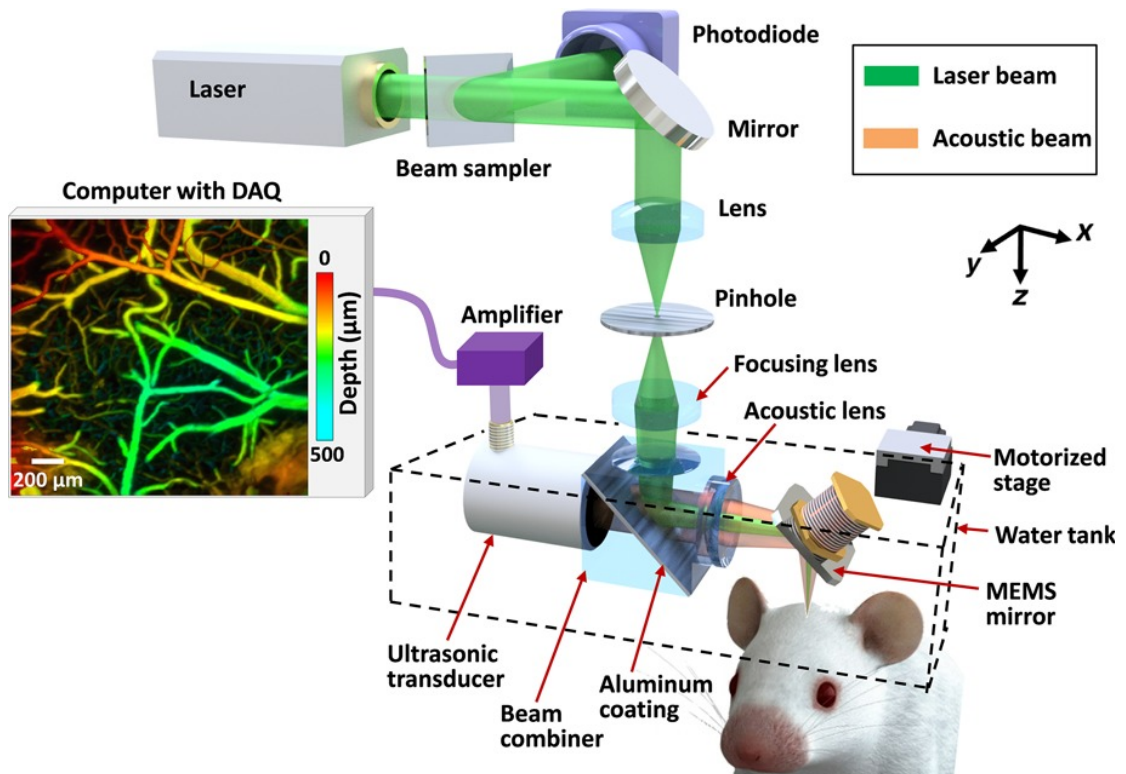


Figure 30. Schematic of the high-speed OR-PAM.

Compared with conventional OR-PAM [98], the distinguishing feature of high-speed OR-PAM is the confocal steering of the excitation laser beam and the detection acoustic axis by a lab-made water-immersible microelectromechanical system (MEMS) scanning mirror (Fig. 30). The confocal steering ensures uniform detection sensitivity over a large FOV. The excitation laser beam (3 ns at 532 nm), generated by an Nd:YVO₄ laser, is spatially filtered by a 50 μm diameter pinhole, then reflected to the MEMS mirror by an optical-acoustic beam combiner. The beam combiner provides optical-acoustic coaxial alignment by reflecting light but transmitting sound. The photoacoustic waves from the focus are selected by an acoustic lens and detected by an ultrasonic transducer (central frequency of 50 MHz; -6 dB bandwidth of 100%). The fast angular scanning of the MEMS mirror along the x -axis enables a cross-sectional (B-scan) imaging rate of 400 Hz over a 3 mm range. Volumetric imaging is achieved by a slow linear step motor that scans the object along the y -axis. The lateral resolution is ~ 3 μm at the optical focus. The axial resolution is estimated to be ~ 15 μm based on the transducer bandwidth and the speed of sound in tissue. The high laser repetition rate of 100 kHz enables dense sampling for capillary-resolution imaging over a large FOV. The optical fluence at the tissue surface is around 18 mJ/cm^2 , just below the ANSI limit [20].

Animal preparation

To observe a spontaneous microhemorrhage, two-year-old female ND4 Swiss Webster mice (Harlan Laboratory, Inc.; 22 to 28 g) were used for blood flow redistribution measurement. The laboratory animal protocols for this work were approved by the Animal Studies Committee of Washington University in St. Louis. During experiments, the

animals' temperatures were kept at 37 °C by a heating pad. We used an intraperitoneal dose of 100 mg/kg α -chloral hydrate for anesthesia. Each experiment typically took less than three hours. Therefore, no additional injection of the anesthetic mixture was needed.

The scalp was surgically removed before imaging, but the skull was left intact. The skull surface was cleaned with phosphate buffered saline solution. A membrane (clear plastic wrap) at the bottom of a water tank was positioned in gentle contact with the skull surface, where ultrasound gel was applied in advance to couple the acoustic signals. The head of the mouse was fixed in a stereotaxic frame. A motor stage translated the animal and the water tank along the y-axis at a speed of 2–4 mm/s (Fig. 30).

For CA imaging, with no need for aged animals, we used three female ND4 Swiss Webster mice (Harlan Laboratory, Inc.; 16–22 g, 4 weeks old). After mounting the animal in the imaging system, phenylephrine, a clinically used vasoconstrictor, was intravenously infused into the tail vein at a dose of 1 mg/kg. Other preparation procedures were the same as for the blood flow redistribution measurement.

Manipulating blood flow with photothrombosis of single vessels

Optical access to the vasculature offers the opportunity for laser-induced occlusion of single vessels as a model to study the effects of small-scale stroke in mice. In addition to imaging spontaneous microhemorrhage in aged mice brains, we studied blood flow redistribution due to a laser-induced vessel occlusion. We intentionally damaged the vessel wall by focusing a continuous wave (CW) laser beam at 650 nm (50 mW) into the lumen of a vessel, and a blood clot formed closely downstream from the irradiation site. The CW laser beam and the PA imaging beam were aligned so that the two beams were focused in

the same focal plane. The CW beam was roughly centered in the area that was raster-scanned by the imaging beam. The energy of the CW beam was varied, and the time of irradiation was controlled based on the clot formation assessed from the OR-PAM images.

High-speed OR-PAM of blood flow redistribution in mini-stroke models

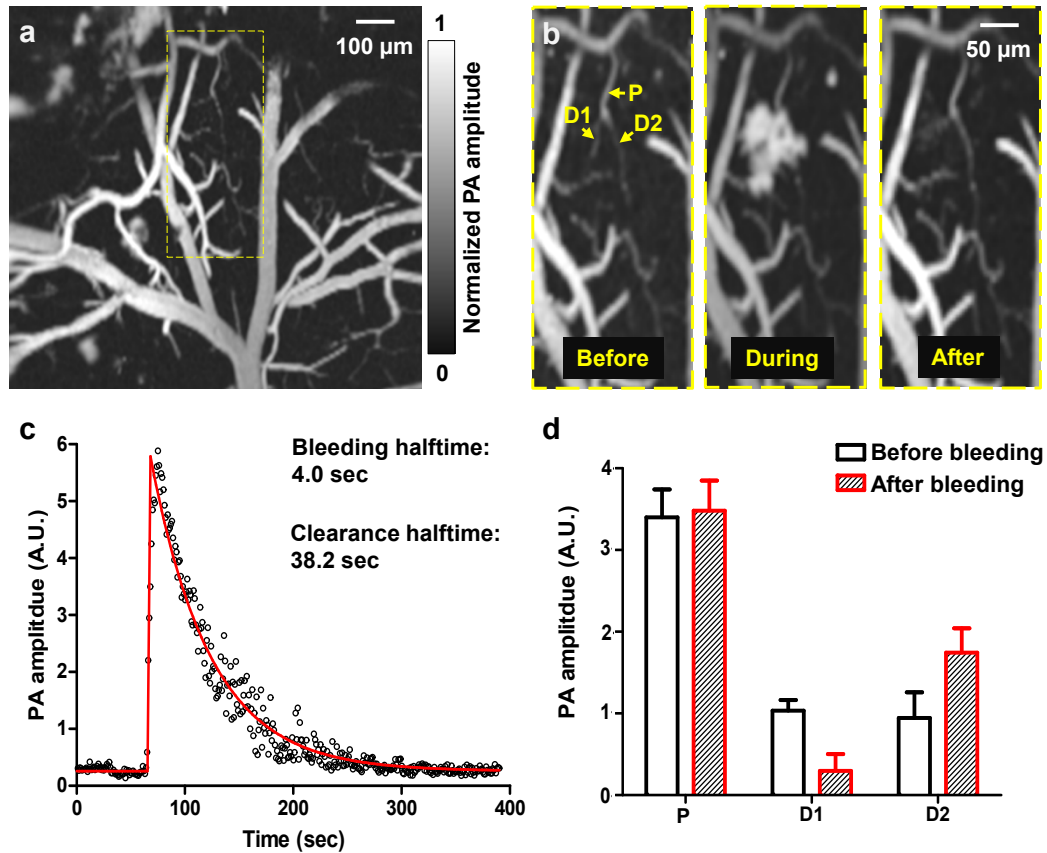


Figure 31. High-speed OR-PAM of ischemic mini-stroke dynamics in a mouse brain. (a) OR-PAM image of a 1 mm by 1 mm cortical area, where spontaneous bleeding was observed in the boxed region. (b) Zoomed-in images of the bleeding region, showing a capillary bifurcation composed of a parent vessel (P) and two daughter vessels (D1 and D2). Spontaneous bleeding was observed at daughter vessel D1. (c) The time course of the bleeding dynamics, which shows that the bleeding half-time was 4.0 seconds and the extravascular blood was cleared with a half-time of 38.2 seconds. On the fitted curve, the half-time is the time duration from the baseline to half of the peak or from the peak to half of the peak. (d) The PA signals from the parent vessels and daughter vessels show the blood

volume redistribution after the bleeding, with the loss of the blood volume in the bleeding daughter vessel D1 compensated by the blood volume increase in the intact daughter vessel D2.

A spontaneous microhemorrhage was observed by high-speed OR-PAM at a cortical bifurcation in a two-year-old mouse (Fig. 31a). The dynamic imaging showed that the hemorrhage stopped within 8 seconds and the extravasated red blood cells were cleared within 80 seconds (Fig. 31b, c). After the hemorrhage, the blood flow in the hemorrhaged daughter vessel was completely stopped. By contrast, the blood flow speed in the intact daughter vessel was increased by $\sim 100\%$, due to the conservation of volumetric blood flow. Since the vessel diameter did not change, the pressure gradient in the intact daughter vessel must have increased accordingly. In addition, the signal amplitude in the intact daughter vessel significantly increased, which reflected an elevated red blood cell (RBC) density (Fig. 31d). The escalated blood flow speed and RBC density increased the risk of further hemorrhages in the remaining vessels [99].

In addition to imaging a spontaneous microhemorrhage, we created an occlusion on the parent vessel of a bifurcation by focusing a high-power CW laser beam of 650 nm in wavelength. The formation of the occlusion was monitored by fast full-frame imaging (Fig. 32a). Before and after the occlusion, RBC flow speeds were measured at each vessel branch by the line scanning method (Fig. 32b). The dynamic imaging revealed a dramatic blood flow decrease in the parent vessel after occlusion (Fig. 32c). Meanwhile, the blood flow in one of the daughter vessels, marked D1 in Fig. 32b, was quickly reversed after occlusion (Fig. 32d), and a new blood flow pathway was immediately formed between the two daughter vessels, which reflected the plasticity of the cortical vascular network. By

governing the blood flow redistribution after vessel occlusion, such plasticity may have therapeutic implications for large and small-scale strokes [100].

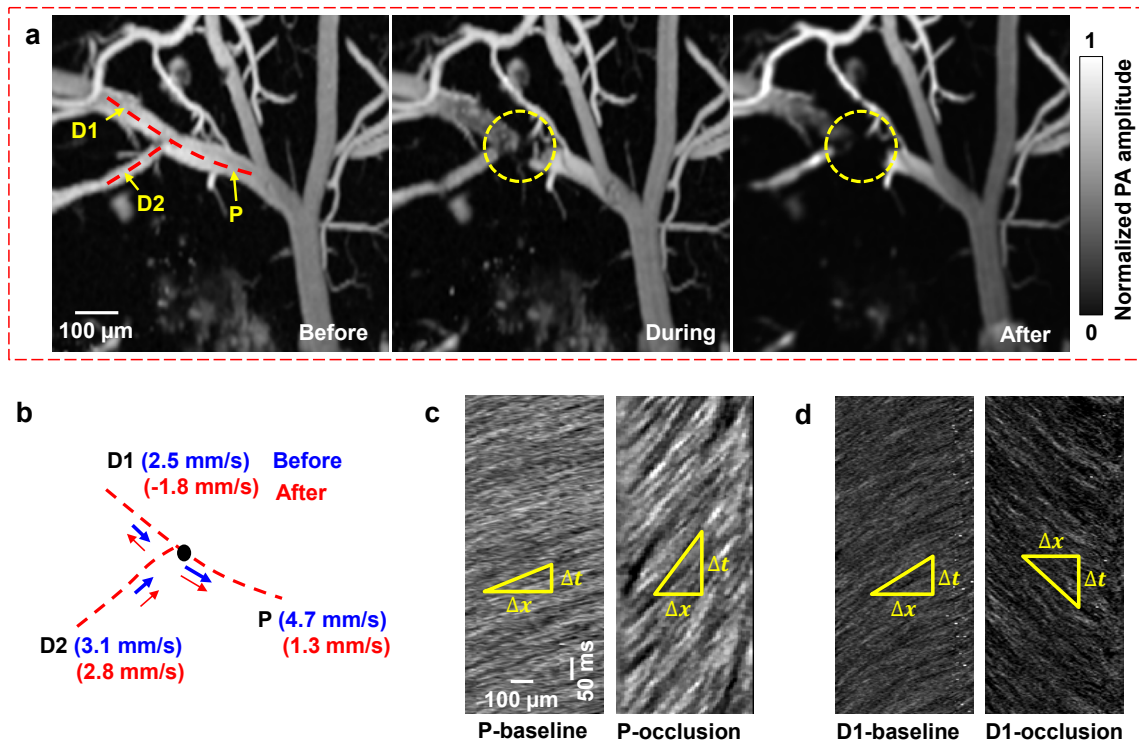


Figure 32. Blood flow dynamics in response to vessel occlusion. A CW laser at 650 nm was focused at the lumen of a vessel to induce photothrombosis. (a) The occlusion region is marked by the dashed circle. Snapshots are shown before, during, and after the occlusion. (b) Line scanning at the bifurcation, consisting of a parent vessel (P) and two daughter vessels (D1 and D2), shows a reduced flow speed in the parent vessel and the reverse flow in the daughter vessel (D1). (c-d) Line scanning images of the parent vessel (c) and one daughter vessel (d) before and after the occlusion, which show the blood flow slowing down in the parent vessel and reversing in the daughter vessel.

Interestingly, in both of the mini-stroke models, strong signals were observed from amoeboid structures scattered over the damaged region. These structures appeared ~30 seconds after the hemorrhage and ~80 seconds after vessel occlusion (Fig. 33). Microglia are resident macrophages in the brain. They are rapidly activated, undergoing

morphological changes to amoeboid morphology in response to brain injuries such as ischemic stroke [99, 101]. Multiple substances might contribute to the absorption contrast: In response to brain injuries, microglia quickly display several activation markers, including CD68 and major histocompatibility complex class II [101, 102]. Besides, microglia/macrophages are the makers of Peridinin-chlorophyll protein complex, which has ~60% of peak absorbance at 532 nm [103]. Therefore, given the diameters of these structures (~10 μm) and their highly confined locations, we speculate that the amoeboid structures at the mini-stroke/occlusion regions were microglia/macrophages activated by a rapid inflammatory response.

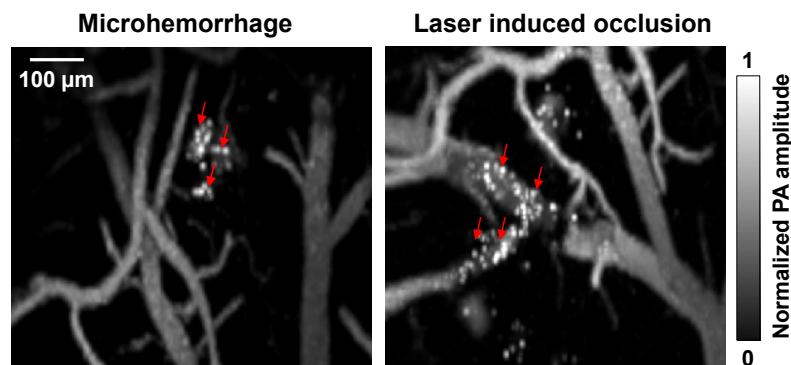


Figure 33. Amoeboid structures (indicated by arrows) were observed in the damaged regions after hemorrhage and vessel occlusion.

High-speed OR-PAM of cerebral autoregulation

The intravenous tail vein infusion of phenylephrine, a clinically used vasoconstrictor, induced a systemic decrease in vessel diameters. High-speed OR-PAM of the mouse brain showed that, despite the administration of phenylephrine, the majority of the cerebral blood vessels remained of constant diameter, indicating an intact CA system (Fig. 34a, b, and h). The blood brain barrier (BBB) effectively blocked phenylephrine from diffusing out of the vessels [104]. Interestingly, blood perfusion to a subpopulation of vessels was completely

stopped (Fig. 34b, 33c and 33h), which indicates that selectively turning off a subpopulation of vessels may be part of the CA mechanism for blood redistribution. Quantitatively, the volumetric changes of different vessel types were quantified after vessel segmentation (Fig. 34d). While the trunk vessels with diameters larger than 50 μm showed no significant change in volume, the smaller vessels had a slight volumetric decrease of $\sim 10\%$ (Fig. 34e).

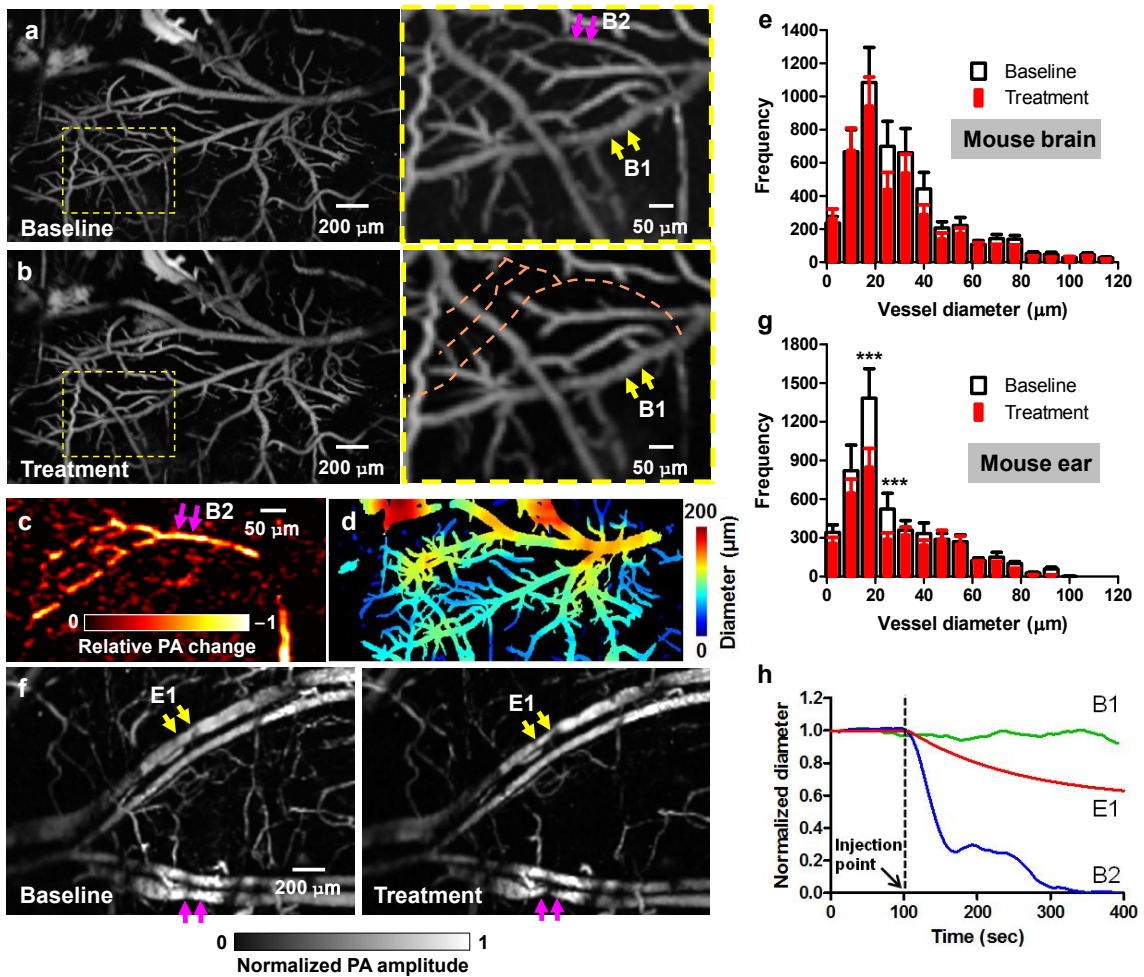


Figure 34. High-speed OR-PAM of mouse brain autoregulation in response to phenylephrine. (a-b) PA images of a 2 mm by 3 mm cortical area before (a) and after (b) the intravenous tail vein injection of phenylephrine, a vasoconstriction agent. While the brain autoregulation maintained the diameters of the majority of vessels, blood perfusion to a sub-population of vessels was completely stopped. (c) The relative PA signal change

between the close-ups in (a) and (b), showing the vessels with stopped blood perfusion. (d) Automatic vessel segmentation was used to quantify the vessel diameters. (e) The statistical results show no significant difference in the vessel diameters in the mouse brain before and after the injection of phenylephrine. (f) A comparative study performed in the mouse ear shows clear vasoconstriction (marked by arrows) after the injection. (g) The statistical results also confirmed the decrease in vessel diameters in the mouse ear after the injection. Statistics: paired Student's t-test. *** $p < 0.001$, $n = 3$. (h) Averaged diameter changes of representative vessel segments in the mouse brain and ear in response to phenylephrine. B1 and B2 are brain vessel segments marked in the close-up in (a), and E1 is an ear vessel segment marked in (f). While the diameter of E1 steadily decreased after the injection, the diameter of B1 remained constant and the blood perfusion in B2 stopped.

Phenylephrine does not penetrate the BBB, but it does increase systemic blood pressure, and thereby increases blood flow velocity to the brain [104]. The brain vasculature reacts by constricting so that cerebral blood flow is kept constant (this activity is not dependent on phenylephrine but is a normal reactive change). Therefore, we think the turnoff of cerebral vessels was a reactive vasoconstriction caused by an increase in systemic blood pressure.

As a comparison, we also imaged the vasoactive effect of phenylephrine on the blood vessels in the mouse ear, where the vascular autoregulation system is much less developed (Fig. 34f). After phenylephrine administration, we observed a clear systemic vasoconstriction in the mouse ear. While the trunk vessels showed an average decrease in volume of ~30%, the small vessels had a volumetric decrease of ~60% (Fig. 34g and h), which in turn confirmed the counter-vasoactive effect of CA in the brain.

Discussion

The pathways of cortical microhemodynamics are closely coupled in neuronal activity [105]. The vasculature network nourishing the mammalian cortex is highly interconnected with extensive redundant connections. Cortical microhemorrhage and occlusion in aged brains, so-called mini-strokes, do not produce acute clinical stroke symptoms, but they are nevertheless closely linked to cognitive decline and dementia. Blood flow redistribution after microhemorrhage and occlusion is a crucial mechanism that mitigates the adverse effects of vessel obstruction, which otherwise can induce severe brain damage via ischemia. Imaging the hemodynamic response to mini-strokes can provide information leading to a deeper understanding of stroke mechanisms. CA plays another important role in maintaining adequate and stable blood flow in the brain. Impaired cerebral autoregulation is clinically used as a diagnostic indication of brain cancers and many neurological disorders [106].

Using endogenous contrast, OR-PAM has high spatial-temporal resolution, enabling imaging the microvasculature of the mouse brain through the intact skull, and observing the hemodynamic responses evoked by various stimulations. Although other biomedical imaging modalities have demonstrated similarly high imaging speeds, they usually have either limited spatial resolution or a small FOV. With a high volumetric scanning speed over a large FOV, high-speed OR-PAM could also quantitatively assess the energy metabolic information of cortical regions [107]. With its highly scalable spatial resolution and imaging speed, OR-PAM is a promising tool for neurophysiological studies.

Chapter VIII

HANDHELD OR-PAM

The high-speed imaging capability in benchtop OR-PAM was realized by the use of a 1D-MEMS scanning mirror. The millisecond-level cross-sectional imaging speed over a millimeter-level FOV makes handheld implementation possible. However, the size of the benchtop OR-PAM needs to be reduced for handheld use. In this chapter, we minimized the benchtop OR-PAM using a 2D-MEMS scanning mirror to reduce the space occupied by mechanical scanners, and we demonstrated handheld skin imaging.

Motivation

The American Cancer Society recommends regular examinations of skin lesions as the best way to find skin cancers early [108]. Therefore, a noninvasive device that can easily scan the body would facilitate such routine examinations. For use in medical offices and clinics, handheld microscopes have been developed based on various optical imaging modalities [109-112]. Compact confocal microscopy achieves fast imaging speed with high spatial resolution, but its shallow imaging depth (200 to 300 μm) limits its wide application [109, 110]. Optical coherence tomography-based probes exploit the optical contrast in backscattered light [111, 112] and are complementary to PAI, which shows the optical absorption contrast.

In this chapter, we present a handheld probe, based on OR-PAM, that uses a newly developed two-axis water-immersible MEMS scanning mirror [64]. In the OR-PAM probe, the optical and acoustic beams are confocally configured to maximize the SNR [98, 113]. The two beams are fast scanned by the MEMS mirror, yielding a 3D imaging rate of

2 Hz over a $2.5 \times 2.0 \times 0.5 \text{ mm}^3$ volume. This probe was tested *in vivo* on both the mouse ear and human skin.

System Construction and Characteristics

Figure 35a shows a schematic of the optical and acoustic elements in the OR-PAM handheld probe. A laser beam is directed into the probe through a single-mode fiber (P1-460B-FC-2, Thorlabs), which guides the light to a lens tube in the handheld probe. Two optical lenses (AC127-025-A, Thorlabs; and PAC025, Newport) in the lens tube focus the light to an optical–acoustic beam combiner immersed in water [114]. Similar to the benchtop OR-PAM in Chapter VII, the focused laser beam is reflected by the MEMS mirror plate onto the surface of the object to be imaged. Volumetric imaging is provided by fast rotational scanning along the x-axis and slow rotational scanning along the y-axis, as well as by the time-resolved detection of the ultrasound signal. The imaging probe is filled with water for ultrasound coupling.

Figure 35b shows a 3D rendering of the OR-PAM handheld probe. The probe has dimensions of $80 \text{ mm} \times 115 \text{ mm} \times 150 \text{ mm}$ along the x, y, and z axes. The lens tube is mounted on a five-axis lens positioner (LP-05A, Newport), which is used for fine tuning the laser beam. The MEMS scanning mirror is fixed on a compact linear stage (DS25-XY, Newport) for precise position adjustment. The front, bottom, and cover panels are made of transparent acrylic to help to localize the targeted area. The imaging window on the bottom panel has a diameter of 6 mm and is sealed with a transparent film. The PA signal from the ultrasound transducer is amplified by two integrated amplifiers (ZX60-43-S+ and ZFL-500LN+, Minicircuits) that provide a total amplification of 41 dB. The probe is grounded through a cable attached to the backboard.

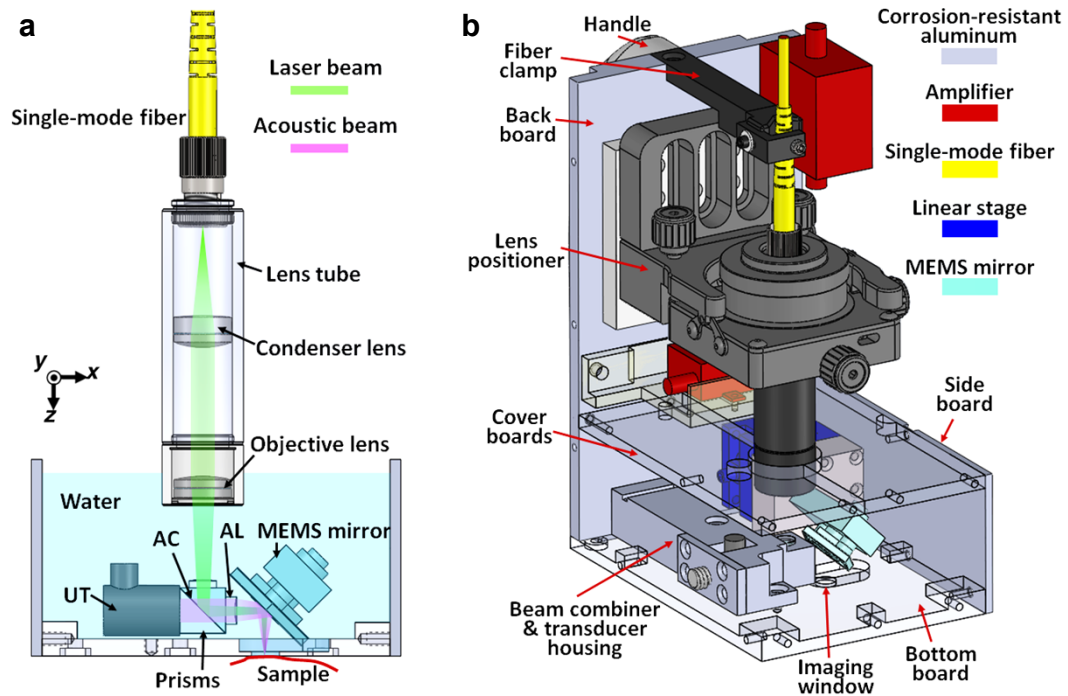


Figure 35. Schematic of the OR-PAM handheld probe. (a) 2-D sketch of the optical and acoustic beams in the probe. UT, ultrasound transducer; AC, aluminum coating; AL, acoustic lens. (b) 3-D rendering of the OR-PAM handheld probe. The front and the left side panels are removed for better visualization.

The handheld probe is connected to the laser, MEMS driver, DAQ devices, and computer. The light is provided by a fiber laser (VPFL-G-10, VGEN) that generates 5-ns pulses at 532 nm, with a pulse repetition rate of 88 kHz. The MEMS mirror is driven by a sinusoidal current from a homemade MEMS driver. The amplified PA signal from the probe is recorded by the DAQ device with a sampling rate of 250 MHz. A low-pass filter (BLP-70+, Minicircuits) is connected between the amplifier and the analog-to-digital converter to eliminate high-frequency noises. Both the mirror scanning and the DAQ are synchronized with the laser pulse.

To characterize the lateral resolution of the handheld OR-PAM system, the edge of a sharp blade was imaged in water, with a step size of 1 μm and a scanning range of 250 μm along

the x-axis. After conversion from polar coordinates to Cartesian coordinates, the MAP of the B-scan along the acoustic axis was calculated and is plotted as a function of the displacement of the optical and acoustic foci from the edge (Fig. 36). Assuming a Gaussian line spread function, fitting of the measured data to an error function indicates a lateral resolution of $5.0\ \mu\text{m}$ (FWHM), which agrees well with the theoretical diffraction-limited focused laser spot size ($4.9\ \mu\text{m}$). The lateral resolution in tissue decreases with imaging depth due to optical scattering. The axial resolution of the system is determined by the bandwidth of the ultrasound transducer and was estimated to be $26\ \mu\text{m}$. The penetration depth of the handheld probe was quantified by a hair embedded in an optical scattering medium consisting of 2% Intralipid solution (reduced scattering coefficient $\mu'_s = 15\ \text{cm}^{-1}$ at 532 nm) and 3% agar gel, which mimics the reduced scattering coefficient of the human skin [115]. The x-z projected MAP image is shown in Fig. 36b. The PA signal from the hair $0.54\ \text{mm}$ beneath the surface (indicated by the dashed line) was still detectable when 100-nJ pulse energy was used.

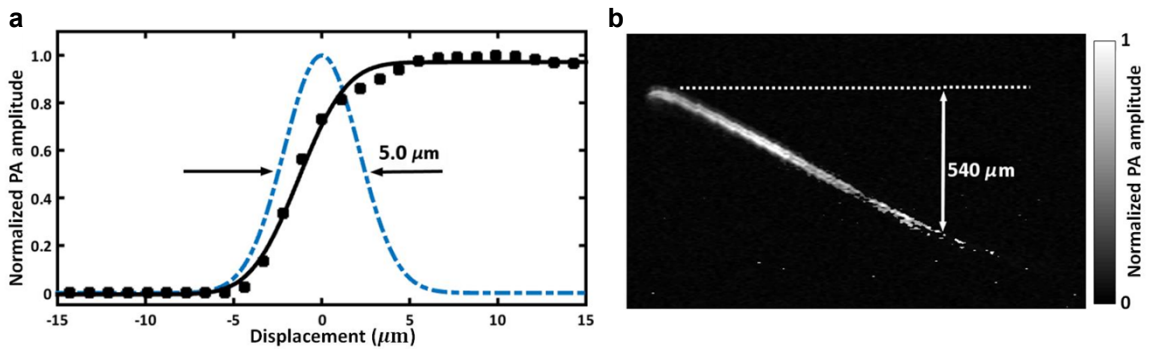


Figure 36. Characteristics of the handheld OR-PAM probe. (a) Lateral resolution measurement by imaging a sharp edge. Solid squares: the PA amplitude when the laser beam was scanned across the edge. Solid curve: the fit of the measured data to an error function. Dashed line: the extracted Gaussian-shaped line spread function. (b) Penetration depth measured by a hair embedded in an optical scattering medium mimicking skin tissue.

The acoustic attenuation has been compensated for by multiplying the PA signal by a depth-dependent exponential correction factor. The gray bar shows the normalized PA signal amplitude.

Results

To demonstrate the fast imaging capability of the handheld OR-PAM system, the vessels in a mouse ear were continuously scanned after a tail vein injection of 0.6 mL of 0.9% saline. The postinjection changes in the PA signal from the vessels were monitored with a temporal resolution of 2 Hz. Representative images taken at different times after the injection (Fig. 37a) show a decrease in the PA signal followed by a slower recovery process. To quantitatively characterize the changes in the signal from the vessels, we calculated the average of the pixel amplitude over the region indicated by the dashed box. The background signal was calculated by averaging over a region of the same size but without vessels inside. The net signal from the blood vessels is shown as a function of time in Fig. 37b. The initial drop in the signal was probably due to a quick wave of injected saline before it was homogeneously mixed with blood, while the slow increase later was due to the diluting effect of blood [116].

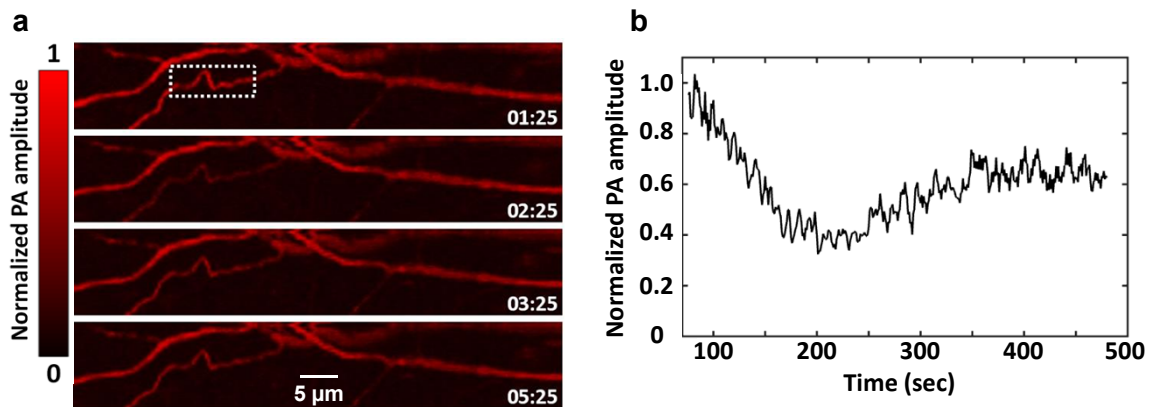


Figure 37. Hemoglobin concentration monitoring in the vessels in a mouse ear after tail vein injection of 0.9% saline. (a) Representative images recorded at different time points

after the injection of 0.6 mL saline. The stamps on the images indicate the time (min:s) after the injection. (b) The signal from the blood vessels within the dashed box in (a) as a function of time. The injection procedure lasted 75 s.

To demonstrate the flexibility of the handheld probe in clinical applications, we tested the system by imaging the human skin. All the human experiments followed a protocol approved by the Institutional Review Board administered by the Human Research Protection Office at Washington University in St. Louis. We first imaged the blood vessels under a cuticle. To obtain higher SNR, the region of interest was scanned repeatedly at a volumetric imaging rate of 2 Hz, and images were averaged over 20 C-scans. It should be noted that the small shift of the same imaging region during the DAQ was corrected by image translation transform, with the shifts calculated from image correlation. In Fig. 38(a), the vessels under the cuticle can be seen clearly, with an SNR of 26 dB.

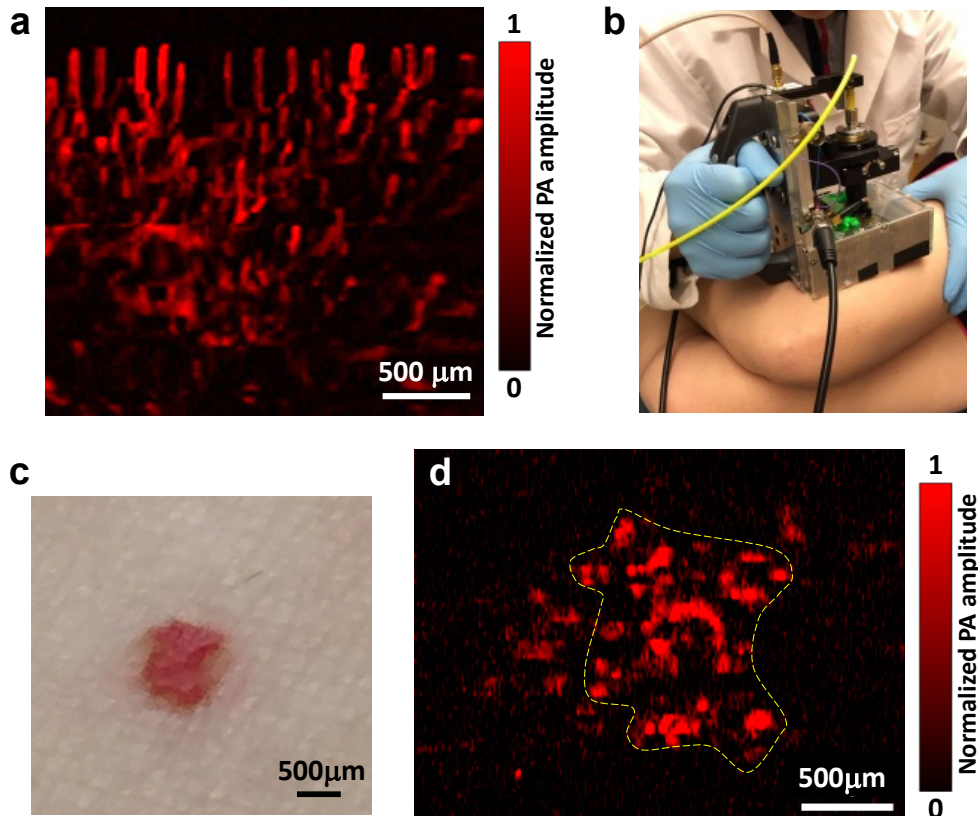


Figure 38. OR-PAM of the human skin by the handheld probe. (a) OR-PAM image of capillaries in a cuticle. (b) Photograph of the OR-PAM handheld probe imaging a red mole on a volunteer's leg. (c) Photograph of the mole. (d) OR-PAM image of the mole. The color bar shows the normalized PA signal amplitude.

The key advantage of a handheld system is its capability of imaging an area that is usually not accessible by a benchtop device. To demonstrate this advantage, a red mole on a healthy volunteer's leg was imaged by the handheld OR-PAM probe, as shown in Fig. 38b–d. The scan fully covered the mole, and a single C-scan PAM image was able to resolve the features, with an SNR of 20 dB. The optical fluence at the skin surface was around 18 mJ/cm², just below the ANSI limit [20].

Summary

In summary, we have developed a handheld OR-PAM probe equipped with a water-immersible 2D MEMS mirror for fast skin imaging. Potential applications of the probe have been demonstrated on a mouse ear and human skin. The scanning range of the probe is 2.5 mm × 2.0 mm, and the volumetric imaging rate is 2 Hz, which is mainly limited by the resonant frequency of the fast axis of the MEMS. The penetration depth of the present optical-resolution probe is 540 μm, which is chiefly limited by the optical scattering in the tissue and can be improved by using near-infrared light that usually undergoes less scattering in biological tissue [117]. Compared with the linear array-based photoacoustic computed tomography, the handheld OR-PAM provides finer spatial resolutions in the superficial region. Moreover, with multiwavelength measurements, OR-PAM has a better accuracy in quantifying the oxygen saturation of hemoglobin [118].

Chapter IX

CONCLUSIONS AND OUTLOOK

To date, PAI is the only high-resolution optical imaging modality that breaks the optical diffusion limit. With its multiscale and multi-contrast imaging capability, PAI has irreplaceable advantages over other imaging modalities in biological research and has attracted growing interest for clinical applications. Evolving from benchtop modalities designed for small animal imaging, translational PAI has been developed with improved imaging depth, reliability, and portability.

Overall, the essential improvements in PACT for bedside imaging have been made to provide greater depth and multiple contrasts. Starting from imaging the rat brain (Chapter II), PACT was translated to human breast imaging, detecting breast cancer and assessing its response during NAC (Chapter III). A 3D PACT system was developed subsequently with isotropic 3D resolution, and has been applied to human breast and brain imaging (Chapter IV). To further extend the imaging depth and provide more imaging contrast, microwave-based TAT was demonstrated *in vivo* (Chapter V). We also demonstrated multispectral PACT to provide additional contrast based on myoglobin (Chapter VI). In addition to translating PACT to the bedside, we minimized a benchtop high-speed OR-PAM system (Chapter VII) to a handheld probe for human skin imaging (Chapter VIII).

What makes an imaging modality truly impactful in clinics are its high reliability and the capability to provide clinically useful information which is unavailable or impractical with other technologies. PAI certainly owns irreplaceable advantages over other imaging modalities. It is the only technology that can provide both optical contrast and high depth-

to-resolution ratio. We have advanced PAI from the bench to bedside, but there remain challenges to be solved. For instance, one aspect of PAI that needs improvement relates to quantitative imaging, which is important for functional and molecular imaging. The quantification accuracy of absolute absorption coefficient is limited by the unpredictability of the wavelength-dependent optical fluence in tissues. While PAI faces a few challenges, exciting PAI results have already been reported. With its unique combination of optical absorption contrast, ultrasonic imaging depth, and scalable resolution, PAI is expected to find more high-impact applications in both biomedical research and clinical practice.

BIBLIOGRAPHY

1. Wang, L.V.W., Hsin-I, Biomedical optics: principles and imaging. *John Wiley & Sons*, 2012.
2. Culver, J.P., V. Ntziachristos, M.J. Holboke, and A.G. Yodh, Optimization of optode arrangements for diffuse optical tomography: A singular-value analysis. *Opt Lett*, **26**(10): p. 701-3, 2001.
3. Wang, L.V. and S. Hu, Photoacoustic tomography: in vivo imaging from organelles to organs. *Science*, **335**(6075): p. 1458-62, 2012.
4. Guo, Z., L. Li, and L.V. Wang, On the speckle-free nature of photoacoustic tomography. *Medical physics*, **36**(9Part1): p. 4084-4088, 2009.
5. Shah, J., S. Park, S.R. Aglyamov, T. Larson, L. Ma, K.V. Sokolov, K.P. Johnston, T.E. Milner, and S.Y. Emelianov, Photoacoustic imaging and temperature measurement for photothermal cancer therapy. *Journal of biomedical optics*, **13**(3): p. 034024, 2008.
6. Xu, M. and L.V. Wang, Universal back-projection algorithm for photoacoustic computed tomography. *Physical Review E*, **71**(1): p. 016706, 2005.
7. Wang, L.V., Multiscale photoacoustic microscopy and computed tomography. *Nature photonics*, **3**(9): p. 503, 2009.
8. Hristova, Y., P. Kuchment, and L. Nguyen, Reconstruction and time reversal in thermoacoustic tomography in acoustically homogeneous and inhomogeneous media. *Inverse Problems*, **24**(5): p. 055006, 2008.
9. Hu, S. and L.V. Wang, Optical-resolution photoacoustic microscopy: auscultation of biological systems at the cellular level. *Biophysical journal*, **105**(4): p. 841-847, 2013.
10. Lutzweiler, C. and D. Razansky, Photoacoustic imaging and tomography: reconstruction approaches and outstanding challenges in image performance and quantification. *Sensors*, **13**(6): p. 7345-7384, 2013.
11. Shu, W., M. Ai, T. Salcudean, R. Rohling, P. Abolmaesumi, and S. Tang, Broadening the detection view of 2D photoacoustic tomography using two linear array transducers. *Optics express*, **24**(12): p. 12755-12768, 2016.
12. Hoover, E.E. and J.A. Squier, Advances in multiphoton microscopy technology. *Nature photonics*, **7**(2): p. 93, 2013.
13. Turnbull, D.H. and S. Mori, MRI in mouse developmental biology. *NMR in Biomedicine: An International Journal Devoted to the Development and Application of Magnetic Resonance In vivo*, **20**(3): p. 265-274, 2007.
14. Wang, X., Y. Pang, G. Ku, X. Xie, G. Stoica, and L.V. Wang, Noninvasive laser-induced photoacoustic tomography for structural and functional in vivo imaging of the brain. *Nature biotechnology*, **21**(7): p. 803, 2003.
15. Wang, X., Y. Pang, G. Ku, G. Stoica, and L.V. Wang, Three-dimensional laser-induced photoacoustic tomography of mouse brain with the skin and skull intact. *Optics letters*, **28**(19): p. 1739-1741, 2003.
16. Ku, G., X. Wang, X. Xie, G. Stoica, and L.V. Wang, Imaging of tumor angiogenesis in rat brains in vivo by photoacoustic tomography. *Applied optics*, **44**(5): p. 770-775, 2005.

17. Razansky, D., A. Buehler, and V. Ntziachristos, Volumetric real-time multispectral optoacoustic tomography of biomarkers. *Nature protocols*, **6**(8): p. 1121, 2011.
18. Xia, J., M.R. Chatni, K.I. Maslov, Z. Guo, K. Wang, M.A. Anastasio, and L.V. Wang, Whole-body ring-shaped confocal photoacoustic computed tomography of small animals in vivo. *Journal of biomedical optics*, **17**(5): p. 050506, 2012.
19. Yao, J., J. Xia, K.I. Maslov, M. Nasiriavanaki, V. Tsytarev, A.V. Demchenko, and L.V. Wang, Noninvasive photoacoustic computed tomography of mouse brain metabolism in vivo. *Neuroimage*, **64**: p. 257-266, 2013.
20. American National Standards Institute, American National Standard for the Safe Use of Lasers. *ANSI Standard Z136.1*, 2000.
21. Anastasio, M.A., J. Zhang, X. Pan, Y. Zou, G. Ku, and L.V. Wang, Half-time image reconstruction in thermoacoustic tomography. *IEEE transactions on medical imaging*, **24**(2): p. 199-210, 2005.
22. Li, L., L. Zhu, C. Ma, L. Lin, J. Yao, L. Wang, K. Maslov, R. Zhang, W. Chen, and J. Shi, Single-impulse panoramic photoacoustic computed tomography of small-animal whole-body dynamics at high spatiotemporal resolution. *Nature biomedical engineering*, **1**(5): p. 0071, 2017.
23. Siegel, R.L., K.D. Miller, and A. Jemal, Cancer statistics, 2017. *Ca Cancer J Clin*: p. 7-30, 2017.
24. Heymach, J., L. Krilov, A. Alberg, N. Baxter, S.M. Chang, R.B. Corcoran, W. Dale, A. DeMichele, C.S. Magid Diefenbach, and R. Dreicer, Clinical cancer advances 2018: annual report on progress against cancer from the American Society of Clinical Oncology. *Journal of Clinical Oncology*, **36**(10): p. 1020-1044, 2018.
25. Miller, A.B., C. Wall, C.J. Baines, P. Sun, T. To, and S.A. Narod, Twenty five year follow-up for breast cancer incidence and mortality of the Canadian National Breast Screening Study: randomised screening trial. *Bmj*, **348**: p. g366, 2014.
26. Burton, R. and R. Bell, The global challenge of reducing breast cancer mortality. *The oncologist*, **18**(Special Collection): p. 3-5, 2013.
27. Pinsky, R.W. and M.A. Helvie, Mammographic breast density: effect on imaging and breast cancer risk. *Journal of the National Comprehensive Cancer Network*, **8**(10): p. 1157-1165, 2010.
28. Freer, P.E., Mammographic breast density: impact on breast cancer risk and implications for screening. *Radiographics*, **35**(2): p. 302-315, 2015.
29. Devolli-Disha, E., S. Manxhuka-Kërliu, H. Ymeri, and A. Kutlllovci, Comparative accuracy of mammography and ultrasound in women with breast symptoms according to age and breast density. *Bosnian journal of basic medical sciences*, **9**(2): p. 131, 2009.
30. Hooley, R.J., L.M. Scoutt, and L.E. Philpotts, Breast ultrasonography: state of the art. *Radiology*, **268**(3): p. 642-659, 2013.
31. Murphy, K.J., J.A. Brunberg, and R.H. Cohan, Adverse reactions to gadolinium contrast media: a review of 36 cases. *AJR. American journal of roentgenology*, **167**(4): p. 847-849, 1996.
32. Perazella, M.A., Gadolinium-contrast toxicity in patients with kidney disease: nephrotoxicity and nephrogenic systemic fibrosis. *Current drug safety*, **3**(1): p. 67-75, 2008.

33. Ibrahim, D., B. Froberg, A. Wolf, and D.E. Rusyniak, Heavy metal poisoning: clinical presentations and pathophysiology. *Clinics in laboratory medicine*, **26**(1): p. 67-97, 2006.
34. Choe, R., A. Corlu, K. Lee, T. Durduran, S.D. Konecky, M. Grosicka-Koptyra, S.R. Arridge, B.J. Czerniecki, D.L. Fraker, and A. DeMichele, Diffuse optical tomography of breast cancer during neoadjuvant chemotherapy: a case study with comparison to MRI. *Medical physics*, **32**(4): p. 1128-1139, 2005.
35. Culver, J., R. Choe, M. Holboke, L. Zubkov, T. Durduran, A. Slep, V. Ntziachristos, B. Chance, and A. Yodh, Three-dimensional diffuse optical tomography in the parallel plane transmission geometry: Evaluation of a hybrid frequency domain/continuous wave clinical system for breast imaging. *Medical physics*, **30**(2): p. 235-247, 2003.
36. Durduran, T., R. Choe, J. Culver, L. Zubkov, M. Holboke, J. Giammarco, B. Chance, and A. Yodh, Bulk optical properties of healthy female breast tissue. *Physics in Medicine & Biology*, **47**(16): p. 2847, 2002.
37. Heine, J.J. and J.A. Thomas, Effective x-ray attenuation coefficient measurements from two full field digital mammography systems for data calibration applications. *Biomedical engineering online*, **7**(1): p. 13, 2008.
38. Fang, Q., S.A. Carp, J. Selb, G. Boverman, Q. Zhang, D.B. Kopans, R.H. Moore, E.L. Miller, D.H. Brooks, and D.A. Boas, Combined optical imaging and mammography of the healthy breast: optical contrast derived from breast structure and compression. *IEEE transactions on medical imaging*, **28**(1): p. 30-42, 2008.
39. Mallidi, S., G.P. Luke, and S. Emelianov, Photoacoustic imaging in cancer detection, diagnosis, and treatment guidance. *Trends in biotechnology*, **29**(5): p. 213-221, 2011.
40. Weidner, N., J.P. Semple, W.R. Welch, and J. Folkman, Tumor angiogenesis and metastasis—correlation in invasive breast carcinoma. *New England Journal of Medicine*, **324**(1): p. 1-8, 1991.
41. Schneider, B.P. and K.D. Miller, Angiogenesis of breast cancer. *Journal of Clinical Oncology*, **23**(8): p. 1782-1790, 2005.
42. Reynolds, A.R., I.R. Hart, A.R. Watson, J.C. Welti, R.G. Silva, S.D. Robinson, G. Da Violante, M. Gourlaouen, M. Salih, and M.C. Jones, Stimulation of tumor growth and angiogenesis by low concentrations of RGD-mimetic integrin inhibitors. *Nature medicine*, **15**(4): p. 392, 2009.
43. Folkman, J. *Role of angiogenesis in tumor growth and metastasis*. in *Seminars in oncology*. 2002. Elsevier.
44. Toi, M., Y. Asao, Y. Matsumoto, H. Sekiguchi, A. Yoshikawa, M. Takada, M. Kataoka, T. Endo, N. Kawaguchi-Sakita, and M. Kawashima, Visualization of tumor-related blood vessels in human breast by photoacoustic imaging system with a hemispherical detector array. *Scientific reports*, **7**: p. 41970, 2017.
45. Kruger, R.A., C.M. Kuzmiak, R.B. Lam, D.R. Reinecke, S.P. Del Rio, and D. Steed, Dedicated 3D photoacoustic breast imaging. *Medical physics*, **40**(11): p. 113301, 2013.
46. Wang, D., Y. Wang, W. Wang, D. Luo, U. Chitgupi, J. Geng, Y. Zhou, L. Wang, J.F. Lovell, and J. Xia, Deep tissue photoacoustic computed tomography with a fast and compact laser system. *Biomedical optics express*, **8**(1): p. 112-123, 2017.
47. Heijblom, M., W. Steenbergen, and S. Manohar, Clinical photoacoustic breast imaging: the twente experience. *IEEE pulse*, **6**(3): p. 42-46, 2015.

48. Heijblom, M., D. Piras, M. Brinkhuis, J.C. van Hespén, F. Van den Engh, M. Van der Schaaf, J. Klaase, T. Van Leeuwen, W. Steenbergen, and S. Manohar, Photoacoustic image patterns of breast carcinoma and comparisons with Magnetic Resonance Imaging and vascular stained histopathology. *Scientific reports*, **5**: p. 11778, 2015.
49. Fakhrejehani, E., M. Torii, T. Kitai, S. Kanao, Y. Asao, Y. Hashizume, Y. Mikami, I. Yamaga, M. Kataoka, and T. Sugie, Clinical report on the first prototype of a photoacoustic tomography system with dual illumination for breast cancer imaging. *PLoS One*, **10**(10): p. e0139113, 2015.
50. Kitai, T., M. Torii, T. Sugie, S. Kanao, Y. Mikami, T. Shiina, and M. Toi, Photoacoustic mammography: initial clinical results. *Breast Cancer*, **21**(2): p. 146-153, 2014.
51. Ermilov, S.A., T. Khamapirad, A. Conjusteau, M.H. Leonard, R. Lacewell, K. Mehta, T. Miller, and A.A. Oraevsky, Laser optoacoustic imaging system for detection of breast cancer. *J Biomed Opt*, **14**(2): p. 024007, 2009.
52. Ke, H., T.N. Erpelding, L. Jankovic, C. Liu, and L.V. Wang, Performance characterization of an integrated ultrasound, photoacoustic, and thermoacoustic imaging system. *J Biomed Opt*, **17**(5): p. 056010, 2012.
53. Li, X., C.D. Heldermon, L. Yao, L. Xi, and H. Jiang, High resolution functional photoacoustic tomography of breast cancer. *Med Phys*, **42**(9): p. 5321-8, 2015.
54. Cox, B.T., S.R. Arridge, and P.C. Beard, Photoacoustic tomography with a limited-aperture planar sensor and a reverberant cavity. *Inverse Problems*, **23**(6): p. S95-S112, 2007.
55. Huang, B., J. Xia, K. Maslov, and L.H.V. Wang, Improving limited-view photoacoustic tomography with an acoustic reflector. *Journal of Biomedical Optics*, **18**(11), 2013.
56. Lehman, C.D. and M.D. Schnall, Imaging in breast cancer: magnetic resonance imaging. *Breast Cancer Res*, **7**(5): p. 215-9, 2005.
57. Smith, A.M., M.C. Mancini, and S.M. Nie, BIOIMAGING Second window for in vivo imaging. *Nature Nanotechnology*, **4**(11): p. 710-711, 2009.
58. Jacques, S.L., Optical properties of biological tissues: a review. *Physics in Medicine and Biology*, **58**(11): p. R37-R61, 2013.
59. Witt, N.W., N. Chapman, S.A. Thom, A.V. Stanton, K.H. Parker, and A.D. Hughes, A novel measure to characterise optimality of diameter relationships at retinal vascular bifurcations. *Artery Res*, **4**(3): p. 75-80, 2010.
60. Davies, P.F., Flow-Mediated Endothelial Mechanotransduction. *Physiological Reviews*, **75**(3): p. 519-560, 1995.
61. Yoshiya, I., Y. Shimada, and K. Tanaka, Spectrophotometric Monitoring of Arterial Oxygen-Saturation in the Fingertip. *Medical & Biological Engineering & Computing*, **18**(1): p. 27-32, 1980.
62. Xia, J., A. Danielli, Y. Liu, L. Wang, K. Maslov, and L.V. Wang, Calibration-free quantification of absolute oxygen saturation based on the dynamics of photoacoustic signals. *Opt Lett*, **38**(15): p. 2800-3, 2013.
63. Sivaramakrishnan, M., K. Maslov, H.F. Zhang, G. Stoica, and L.V. Wang, Limitations of quantitative photoacoustic measurements of blood oxygenation in small vessels. *Phys Med Biol*, **52**(5): p. 1349-61, 2007.

64. Xu, S., C.H. Huang, and J. Zou, Microfabricated water-immersible scanning mirror with a small form factor for handheld ultrasound and photoacoustic microscopy. *Journal of Micro-Nanolithography MemS and Moems*, **14**(3), 2015.
65. Fenner, J., A.C. Stacer, F. Winterroth, T.D. Johnson, K.E. Luker, and G.D. Luker, Macroscopic Stiffness of Breast Tumors Predicts Metastasis. *Scientific Reports*, **4**, 2014.
66. Yang, X.M., M.L. Li, and L.H.V. Wang, Ring-based ultrasonic virtual point detector with applications to photoacoustic tomography. *Applied Physics Letters*, **90**(25), 2007.
67. Tsai, P.S., J.P. Kaufhold, P. Blinder, B. Friedman, P.J. Drew, H.J. Karten, P.D. Lyden, and D. Kleinfeld, Correlations of Neuronal and Microvascular Densities in Murine Cortex Revealed by Direct Counting and Colocalization of Nuclei and Vessels. *Journal of Neuroscience*, **29**(46): p. 14553-14570, 2009.
68. Bender, L., Science Facts: Human Body. *Crescent Books, New York*, 1992.
69. Lobbes, M.B.I., U.C. Lalji, P.J. Nelemans, I. Houben, M.L. Smidt, E. Heuts, B. de Vries, J.E. Wildberger, and R.G. Beets-Tan, The Quality of Tumor Size Assessment by Contrast-Enhanced Spectral Mammography and the Benefit of Additional Breast MRI. *Journal of Cancer*, **6**(2): p. 144-150, 2015.
70. Gruber, I.V., M. Rueckert, K.O. Kagan, A. Staebler, K.C. Siegmann, A. Hartkopf, D. Wallwiener, and M. Hahn, Measurement of tumour size with mammography, sonography and magnetic resonance imaging as compared to histological tumour size in primary breast cancer. *Bmc Cancer*, **13**, 2013.
71. Manickam, K., M.R. Reddy, S. Seshadri, and B. Raghavan, Development of a training phantom for compression breast elastography-comparison of various elastography systems and numerical simulations. *Journal of Medical Imaging*, **2**(4), 2015.
72. Thirion, J.P., Image matching as a diffusion process: an analogy with Maxwell's demons. *Med. Image Anal.*, **2**: p. 243-260, 1998.
73. Beard, P.C., Photoacoustic imaging for characterising the structure and function of vascular networks. *The Journal of the Acoustical Society of America*, **123**(5), 2008.
74. Yao, J.J., L.D. Wang, J.M. Yang, K.I. Maslov, T.T.W. Wong, L. Li, C.H. Huang, J. Zou, and L.V. Wang, High-speed label-free functional photoacoustic microscopy of mouse brain in action. *Nature Methods*, **12**(5): p. 407+, 2015.
75. Lin, L., P. Hu, J. Shi, C.M. Appleton, K. Maslov, L. Li, R. Zhang, and L.V. Wang, Single-breath-hold photoacoustic computed tomography of the breast. *Nat Commun*, **9**(1): p. 2352, 2018.
76. Xu, M.H. and L.H.V. Wang, Time-domain reconstruction for thermoacoustic tomography in a spherical geometry. *Ieee Transactions on Medical Imaging*, **21**(7): p. 814-822, 2002.
77. Xu, Y. and L.H.V. Wang, Rhesus monkey brain imaging through intact skull with thermoacoustic tomography. *Ieee Transactions on Ultrasonics Ferroelectrics and Frequency Control*, **53**(3): p. 542-548, 2006.
78. Huang, L., T.T. Li, and H.B. Jiang, Technical Note: Thermoacoustic imaging of hemorrhagic stroke: A feasibility study with a human skull. *Medical Physics*, **44**(4): p. 1494-1499, 2017.

79. Jin, X., C.H. Li, and L.V. Wang, Effects of acoustic heterogeneities on transcranial brain imaging with microwave-induced thermoacoustic tomography. *Medical Physics*, **35**(7): p. 3205-3214, 2008.
80. IEEE Standard for Safety Levels with Respect to Human Exposure to Radio Frequency Electromagnetic Fields 3 kHz to 300 GHz. *IEEE Std C95.1-2005 (Revision of IEEE Std C95.1-1991)*, 2006.
81. Ordway, G.A. and D.J. Garry, Myoglobin: an essential hemoprotein in striated muscle. *Journal of Experimental Biology*, **207**(20): p. 3441-3446, 2004.
82. Bekedam, M.A., B.J. van Beek-Harmsen, W. van Mechelen, A. Boonstra, and W.J. van der Laarse, Myoglobin concentration in skeletal muscle fibers of chronic heart failure patients. *Journal of Applied Physiology*, **107**(4): p. 1138-1143, 2009.
83. Weber, M., M. Rau, K. Madlener, A. Elsaesser, D. Bankovic, V. Mitrovic, and C. Hamm, Diagnostic utility of new immunoassays for the cardiac markers cTnI, myoglobin and CK-MB mass. *Clinical Biochemistry*, **38**(11): p. 1027-1030, 2005.
84. Arakaki, L.S.L., W.A. Ciesielski, B.D. Thackray, E.O. Feigl, and K.A. Schenkman, Simultaneous Optical Spectroscopic Measurement of Hemoglobin and Myoglobin Saturations and Cytochrome aa3 Oxidation In Vivo. *Applied Spectroscopy*, **64**(9): p. 973-979, 2010.
85. Arakaki, L.S.L., D.H. Burns, and M.J. Kushmerick, Accurate myoglobin oxygen saturation by optical spectroscopy measured in blood-perfused rat muscle. *Applied Spectroscopy*, **61**(9): p. 978-985, 2007.
86. Hartwig, V., G. Giovannetti, C. Kusmic, C. Quartieri, N. Vanello, I. Puglia, L. Landini, and A. L'Abbate, First Prototype of a Near Infrared Tomograph for Mapping the Myocardial Oxygenation in Small Animal Isolated Hearts. *2008 Ieee International Workshop on Imaging Systems and Techniques*: p. 94+, 2008.
87. Lebon, V., P.G. Carlier, C. Brillault-Salvat, and A. Leroy-Willig, Simultaneous measurement of perfusion and oxygenation changes using a multiple gradient-echo sequence: Application to human muscle study. *Magnetic Resonance Imaging*, **16**(7): p. 721-729, 1998.
88. Befroy, D.E. and G.I. Shulman, Magnetic Resonance Spectroscopy Studies of Human Metabolism. *Diabetes*, **60**(5): p. 1361-1369, 2011.
89. Maslov, K., H.F. Zhang, and L.V. Wang, Effects of wavelength-dependent fluence attenuation on the noninvasive photoacoustic imaging of hemoglobin oxygen saturation in subcutaneous vasculature in vivo. *Inverse Problems*, **23**(6): p. S113-S122, 2007.
90. Flock, S.T., S.L. Jacques, B.C. Wilson, W.M. Star, and M.J.C. Vangemert, Optical-Properties of Intralipid - a Phantom Medium for Light-Propagation Studies. *Lasers in Surgery and Medicine*, **12**(5): p. 510-519, 1992.
91. Hussain, A., K. Daoudi, E. Hondebrink, and W. Steenbergen, Mapping optical fluence variations in highly scattering media by measuring ultrasonically modulated backscattered light (vol 19, 066002, 2014). *Journal of Biomedical Optics*, **19**(6), 2014.
92. Hartmann, P., W. Ziegler, and D.W. Lubbers, Fluorescence lifetime imaging of the skin PO₂ supply instrumentation and results. *Oxygen Transport to Tissue XIX*, **428**: p. 605-611, 1997.

93. Gussakovskiy, E., Y.M. Yang, J. Rendell, O. Jilkina, and V. Kupriyanov, NIR spectroscopic imaging to map hemoglobin plus myoglobin oxygenation, their concentration and optical pathlength across a beating pig heart during surgery. *Journal of Biophotonics*, **5**(2): p. 128-139, 2012.
94. Kim, D.S., T.Q. Duong, and S.G. Kim, High-resolution mapping of iso-orientation columns by fMRI. *Nature Neuroscience*, **3**(2): p. 164-169, 2000.
95. Hillman, E.M.C., A. Devor, M.B. Bouchard, A.K. Dunn, G.W. Krauss, J. Skoch, B.J. Bacskai, A.M. Dale, and D.A. Boas, Depth-resolved optical imaging and microscopy of vascular compartment dynamics during somatosensory stimulation. *Neuroimage*, **35**(1): p. 89-104, 2007.
96. Sakadzic, S., E. Roussakis, M.A. Yaseen, E.T. Mandeville, V.J. Srinivasan, K. Arai, S. Ruvinskaya, A. Devor, E.H. Lo, S.A. Vinogradov, and D.A. Boas, Two-photon high-resolution measurement of partial pressure of oxygen in cerebral vasculature and tissue. *Nature Methods*, **7**(9): p. 755-U125, 2010.
97. Baran, U. and R.K.K. Wang, Review of optical coherence tomography based angiography in neuroscience. *Neurophotonics*, **3**(1), 2016.
98. Maslov, K., H.F. Zhang, S. Hu, and L.V. Wang, Optical-resolution photoacoustic microscopy for in vivo imaging of single capillaries. *Optics Letters*, **33**(9): p. 929-931, 2008.
99. Rosidi, N.L., J. Zhou, S. Pattanaik, P. Wang, W.Y. Jin, M. Brophy, W.L. Olbricht, N. Nishimura, and C.B. Schaffer, Cortical Microhemorrhages Cause Local Inflammation but Do Not Trigger Widespread Dendrite Degeneration. *Plos One*, **6**(10), 2011.
100. Schaffer, C.B., B. Friedman, N. Nishimura, L.F. Schroeder, P.S. Tsai, F.F. Ebner, P.D. Lyden, and D. Kleinfeld, Two-photon imaging of cortical surface microvessels reveals a robust redistribution in blood flow after vascular occlusion. *Plos Biology*, **4**(2): p. 258-270, 2006.
101. Bok, S., T. Wang, C.J. Lee, S.U. Jeon, Y.E. Kim, J. Kim, B.J. Hong, C.J. Yoon, S. Kim, S.H. Lee, H.J. Kim, I.H. Kim, K.H. Kim, and G.O. Ahn, In vivo imaging of activated microglia in a mouse model of focal cerebral ischemia by two-photon microscopy. *Biomedical Optics Express*, **6**(9): p. 3303-3312, 2015.
102. Singer, B.H., M.W. Newstead, X.Y. Zeng, C.L. Cooke, R.C. Thompson, K. Singer, R. Ghantasala, J.M. Parent, G.G. Murphy, T.J. Iwashyna, and T.J. Standiford, Cecal Ligation and Puncture Results in Long-Term Central Nervous System Myeloid Inflammation. *Plos One*, **11**(2), 2016.
103. Song, P.S., P. Koka, B.B. Prezelin, and F.T. Haxo, Molecular topology of the photosynthetic light-harvesting pigment complex, peridinin-chlorophyll a-protein, from marine dinoflagellates. *Biochemistry*, **15**(20): p. 4422-7, 1976.
104. Meng, L., A.W. Gelb, B.S. Alexander, A.E. Cerussi, B.J. Tromberg, Z. Yu, and W.W. Mantulin, Impact of phenylephrine administration on cerebral tissue oxygen saturation and blood volume is modulated by carbon dioxide in anaesthetized patients(dagger). *British Journal of Anaesthesia*, **108**(5): p. 815-822, 2012.
105. O'Herron, P., P.Y. Chhatbar, M. Levy, Z.M. Shen, A.E. Schramm, Z.Y. Lu, and P. Kara, Neural correlates of single-vessel haemodynamic responses in vivo. *Nature*, **534**(7607): p. 378-+, 2016.
106. Paulson, O.B., S. Strandgaard, and L. Edvinsson, Cerebral Autoregulation. *Cerebrovascular and Brain Metabolism Reviews*, **2**(2): p. 161-192, 1990.

107. Yao, J.J., K.I. Maslov, and L.H.V. Wang, Noninvasive quantification of metabolic rate of oxygen (MRO₂) by photoacoustic microscopy. *Photons Plus Ultrasound: Imaging and Sensing 2011*, **7899**, 2011.
108. Friedman, L.C., J.A. Webb, S. Bruce, A.D. Weinberg, and H.P. Cooper, Skin-Cancer Prevention and Early Detection Intentions and Behavior. *American Journal of Preventive Medicine*, **11**(1): p. 59-65, 1995.
109. Calzavara-Pinton, P., C. Longo, M. Venturini, R. Sala, and G. Pellacani, Reflectance Confocal Microscopy for In Vivo Skin Imaging. *Photochemistry and Photobiology*, **84**(6): p. 1421-1430, 2008.
110. Arrasmith, C.L., D.L. Dickensheets, and A. Mahadevan-Jansen, MEMS-based handheld confocal microscope for in-vivo skin imaging. *Optics Express*, **18**(4): p. 3805-3819, 2010.
111. Zhang, E.Z., B. Povazay, J. Laufer, A. Alex, B. Hofer, B. Pedley, C. Glittenberg, B. Treeby, B. Cox, P. Beard, and W. Drexler, Multimodal photoacoustic and optical coherence tomography scanner using an all optical detection scheme for 3D morphological skin imaging. *Biomedical Optics Express*, **2**(8): p. 2202-2215, 2011.
112. Jung, W., J. Kim, M. Jeon, E.J. Chaney, C.N. Stewart, and S.A. Boppart, Handheld Optical Coherence Tomography Scanner for Primary Care Diagnostics. *Ieee Transactions on Biomedical Engineering*, **58**(3): p. 741-744, 2011.
113. Hu, S., K. Maslov, and L.V. Wang, Second-generation optical-resolution photoacoustic microscopy with improved sensitivity and speed. *Optics Letters*, **36**(7): p. 1134-1136, 2011.
114. Yao, J.J., C.H. Huang, L.D. Wang, J.M. Yang, L. Gao, K.I. Maslov, J. Zou, and L.H.V. Wang, Wide-field fast-scanning photoacoustic microscopy based on a water-immersible MEMS scanning mirror. *Journal of Biomedical Optics*, **17**(8), 2012.
115. Maslov, K., G. Stoica, and L.H.V. Wang, In vivo dark-field reflection-mode photoacoustic microscopy. *Optics Letters*, **30**(6): p. 625-627, 2005.
116. Tocantins, L.M., R.T. Carroll, and R.H. Holburn, The Clot Accelerating Effect of Dilution on Blood and Plasma - Relation to the Mechanism of Coagulation of Normal and Hemophilic Blood. *Blood*, **6**(8): p. 720-739, 1951.
117. Hai, P.F., J.J. Yao, K.I. Maslov, Y. Zhou, and L.H.V. Wang, Near-infrared optical-resolution photoacoustic microscopy. *Optics Letters*, **39**(17): p. 5192-5195, 2014.
118. Yao, J.J., K.I. Maslov, Y. Zhang, Y.N. Xia, and L.V. Wang, Label-free oxygen-metabolic photoacoustic microscopy in vivo. *Journal of Biomedical Optics*, **16**(7), 2011.